STRUCTURE-INDUCED OPTICAL ANISOTROPY

IN THIN FILMS

by

Flavio Horowitz

———————————

A Dissertation Submitted to the Faculty of the

COMMITTEE ON OPTICAL SCIENCES (GRADUATE)

In Partial Fulfillment of the Requirements

For the Degree of

DOCTOR OF PHILOSOPHY

In the Graduate College

THE UNIVERSITY OF ARIZONA

1 9 8 3

STATEMENT BY AUTHOR

This dissertation has been submitted in partial fulfillment of requirements for an advanced degree at The University of Arizona and is deposited in the University Library to be made available to borrowers under rules of the Library.

Brief quotations from this dissertation are allowable without special permission, provided that accurate acknowledgment of source is made. Requests for permission for extended quotation from or reproduction of this manuscript in whole or in part may be granted by the head of the major department or the Dean of the Graduate College when in his judgment the proposed use of the material is in the interests of scholarship. In all other instances, however, permission must be obtained from the author.

SIGNED: _____

PREFACE

Several decades after early techniques were established for the thermal evaporation of materials onto substrates (Faraday, 1857), limitations of the old paradigm that films are bulk material in two-dimensional form were gradually realized in different fronts. Worthy of mention are the electron diffraction studies by König and Helwig (1950), optical measurements by Bousquet (1956) and later observations involving water adsorption by Koch (1965).

Such limitations have surfaced more clearly in recent years as a result of greatly improved deposition parameter control, thickness monitoring, and characterization techniques (Movchan and Demchishin, 1969; Thornton, 1973). In particular, microfractography has enabled us to "see" in cross section, through the examination of direct shadowed replicas in the transmission electron microscope, the pronounced columnar structures to which thin films grow under nonequilibrium conditions (Nieuwenhuizen and Haanstra, 1966; Pearson, 1970; Guenter and Pulker, 1976). This materials aspect is considered to be the main problem in optical coatings today (Macleod, 1982).

How can bulk properties be restored to materials in thin film form? Answers to this question have been sought by many authors through the use of thermal treatments (Meaburn, 1966), ultraviolet radiation (Bradford et al., 1965), and electron or ion bombardment (Browning, 1983; Martin et al., 1983), in what currently constitutes a major effort in the field.

But here that was the road not taken. Instead, we have asked: Given the columnar structure of thin films, can it produce any peculiar optical behavior absent in the bulk from which they originated?

In pursuing this question we stepped into a number of riches and complexities far greater than initially realized. Still, we would like this work to be looked at as a search for simplicity.

ACKNOWLEDGMENTS

This work would not have been possible without the far-sighted intuition, constant encouragement, and vast scientific knowledge of my advisor, Prof. Angus Macleod. I am thankful for the opportunity to interact with Angus, which has been a very enjoyable learning experience for me.

I was also greatly honored by the presence of Professors James Burke, Roland Shack, and Francis Turner on the Examining Committee. Their comments and suggestions added to the quality of this dissertation.

Prof. Alan Portis from the University of California at Berkeley and my close, far-away friend, Prof. Jin-Fa Tang, director of the thin film optics lab at Zhejiang University, enriched me greatly with theoretical and experimental ideas. Dr. Ian Hodgkinson from the University of Otago, New Zealand, and Dr. Marten Sikkens from the University of Groningen, the Netherlands, provided direct contributions to this work during their brief but extremely productive stay in our group. I would like to extend my sincere thanks to Drs. Francois Flery and Emil Pelletier from l'École Nationale Supérieure de Physique, Marseille, for their scattering measurements on our samples and for supplying us with valuable literature from the deep-rooted French tradition in thin films.

I wish to express my appreciation to the professors at the Optical Sciences Center, in particular Peter Franken, Roy Frieden, Jack

TABLE OF CONTENTS

LIST OF ILLUSTRATIONS

LIST OF TABLES

ABSTRACT

We consider in this work the contribution of anisotropic microstructure to polarization effects in thin films. The microstructure is pictured by a simple model as composed of identical columns with elliptical cross section elongated in a direction perpendicular to that of the vapor incidence. The asymmetry in columnar structure that results from oblique deposition is identified as the common source for the significant dichroism and birefringence observed in metal and dielectric films, respectively. A four-dimensional theory for multilayer systems is presented that starts from first principles, unifies previous treatments for particular cases of film anisotropy, and properly handles the most general case of elliptically polarized mode propagation. In this framework and from a set of polarimetric measurements, a simple method is devised, with explicit consideration of the anisotropic microstructure, for the determination of the physical thickness and principal refractive indices of a single dielectric film. A sequence of transmittance measurements is performed with a zirconium oxide film deposited at 65° and, substrate role and instrumental errors considered, good agreement is obtained between theory and experiment. Spectrophotometer data for a narrowband filter with 21 layers deposited at 30° is shown to confirm theoretical predictions of peak positions with Angstrom resolution. A hypothetical metal film is discussed that reproduces the essential features observed in the optical behavior of an

aluminum film deposited at 85°. Potential applications and suggestions
for future work are included.

CHAPTER 1

INTRODUCTION

In contrast with the conventional assumption in current
multilayer design techniques, virtually all vacuum-deposited thin films
are anisotropic. (See Figure 1.1.)

Would such a porous, discontinuous material, with its evident
preferential orientations, produce under proper conditions a significant
amount of optical anisotropy? By optical anisotropy we mean a behavior
exhibited during the interaction with light that depends on the direction
of the incident electric field. Its relation to film microstructure is
the general theme of this dissertation.

We could well have entitled it "Form Birefringence in Thin
Films," as long as this is understood in a wide sense to include
dichroism, or direction-dependent absorption, especially for metal films.
According to Born and Wolf (1975, p. 705), form birefringence "...arise(s)
from a scale much larger than molecular, namely when there is an
ordered arrangement of similar particles of optically isotropic material
whose size is large compared with the dimensions of molecules, but small
compared to the wavelength of light."

Crystalline orientation and anisotropic stress have also been
known as sources of birefringence in dielectric coatings, although the
reported extent of their effect (Burgers and Dippel, 1934; Turner and

1
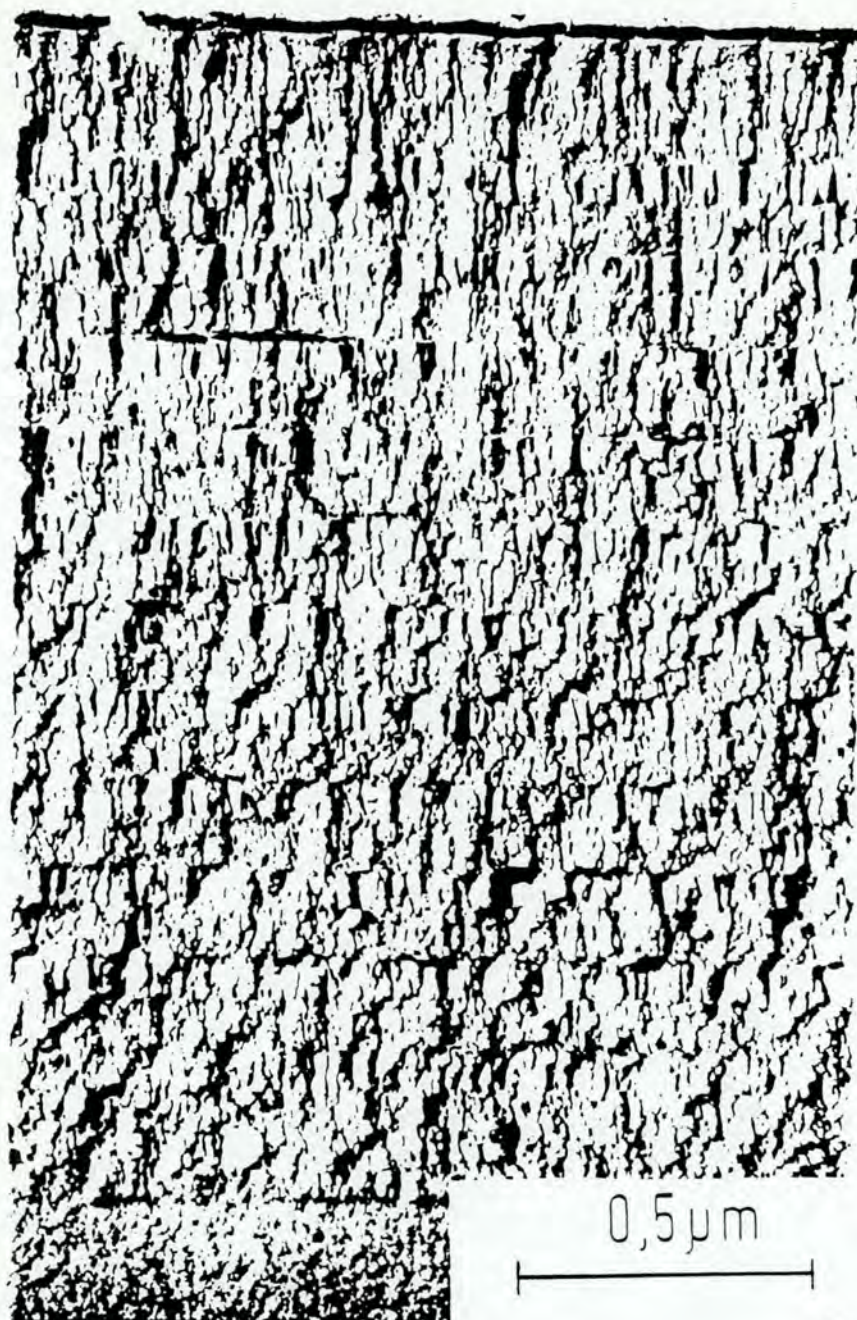
Figure 1.1.   Cross Section of a ZnS/ThF$_4$ Quarterwave Multilayer.

Substrate temperature was approximately 30°C. Trans-
mission micrograph of a preshadowed carbon replica.
Columnar crystals with large diameters are ZnS layers,
smaller columns indicate ThF$_4$ layers. (From Guenther
and Pulker, 1976)

Ulbrich, 1947; Bousquet and Delcourt, 1957; Lichtenstein, 1980) is at least one order of magnitude smaller than the one we will be considering.

We now proceed to place our study in its proper historical context, while briefly outlining its main contents.

Background and Contents

This work is at the intersection between two main historical trends in the science of thin films, one primarily phenomenological, the other predicated on rigorous electromagnetic principles.

The first trend probably started when Kundt (1886) observed polarization effects in several metal films by placing them between Nicol prisms at orthogonal orientations. Supporting reports by Braun (1905), Bergholm (1914), Cau (1928), and later by Coper, Frommer and Zocher (1931), followed.

From that time, when thin film technology was in its early stages of evolution, we often find peculiar expressions such as "film deflagration" and "exploding wires" in the description of deposition procedures (sputtering was also used). It seems that the proximity of sources to substrates initially required by such processes, by inducing the deposition to occur at high angles in some regions, was the triggering cause for those early observations.

Another wave of interest, mainly in obliquely deposited metal films, emerged in the 1950's with investigations by Holland (1953) and Reimer (1957). In 1959, Thiessen and Broglia came across an unwelcomed

polarization effect at the edges of their thermally-aluminized astronomical mirror.

It should also be mentioned that a magnetic counterpart of the optical anisotropy considered here was noticed in evaporated Permalloy films (Smith, 1959; Smith, Cohen and Weiss, 1960).

In the last few years, apart from its use for metal polarizers in the near-infrared (Slocum, 1981) and as a rather small birefringence detected in a few waveguiding dielectric films deposited at low angles of incidence (King and Talim, 1981), the polarization effect attracted little attention.

More recently, a significant retarder-like behavior was observed in a zirconium oxide film deposited at a high angle of incidence. Its amount of birefringence, as well as that of dichroism for a semitransparent aluminum film deposited in similar conditions, were quantitatively estimated at the HeNe wavelength by analyzing their transmittance variations with azimuth angle in a conveniently adapted ellipsometer. This work (Horowitz and Macleod, 1983) is reproduced in Chapter 2 of this dissertation with some extensions. It is still along the first trend, essentially characterized by a (semi)phenomenological approach.

As to the second trend, it probably acquired its initial well-defined forms in the classic article published by Abelés (1950), which presents the following three particularly attractive aspects. (1) The

theory starts directly from Maxwell Equations. (2) Interference effects are taken into account without need to explicitly consider multiple traversals of traveling waves within the medium. (3) The resulting 2x2 matrix treatment is a powerful and simple tool for multilayer calculations.

The problem then arose of finding a similar treatment which would apply equally well for arbitrary anisotropic thin films. Early theories by Schopper (1952) and by Bousquet (1957a) provide valuable predictions but lack items (2) and (3) above, and are only valid when one of the principal axes lies normal to the plane of the film (see also Heavens, 1965, p. 92).

Goncharenko and Fedorov (1963) considered the problem of an arbitrary absorbing crystal of arbitrary orientation in plane-parallel plate form at normal incidence. However, their approach lacks item (3) and cannot be extended to an arbitrary angle of incidence.

A useful 2x2 matrix technique was developed by Holmes and Feucht (1966) for the case in which one principal axis is perpendicular to the plane of incidence. Schesser and Eichmann (1972) proposed a general theory for wave propagation in layered anisotropic media, although their method lacks the simplicity mentioned in (3).

All three requirements are potentially fulfilled, with a high degree of generality, by a 4x4 matrix formulation developed in the following different contexts. In 1970 Teitler and Henvis extended the traditional two-dimensional approach to handle the case of refraction

under magnetically induced anisotropy in an otherwise isotropic semiconductor. Later Berreman (1972) announced a solution to the problem of reflection and transmission by cholesteric and other liquid crystals with continuously varying but planar ordering, in which he utilized a 4 x 4 differential-matrix technique. More recently, Yeh (1979) presented a similar formalism in a solid state physics context, and applied it to the Solc birefringent layered media, to the exchange Bragg scattering, and for a mode dispersion relation in guided waves.

It was hinted by Berning (1963, p. 71) that if a procedure were to be found for anisotropic films that would lead to the results obtained by several authors through different methods, each appropriate for a particular case, then such a procedure should arise from fundamental principles based on electromagnetic theory.

In Chapter 3 of this dissertation we begin from Maxwell's equations and recreate the Teitler and Henvis formalism, with its potential application for thin films in mind. Their approach is particularly suited to our purposes because it retains a close resemblance to the original Abelès method. Once the 4 x 4 propagation matrix of a system is known, transmittances and reflectances are obtainable in a straightforward manner.

It is not made clear in their formalism, however, how the elements of the propagation matrix are to be determined for applications other than the particular one they were studying. Additional insight is

required to fully enable the theory to handle problems on thin-film multilayer design.

We have interpreted the propagation matrix as an operator that maps one vector basis onto another, each corresponding to one of the film surfaces. With this understanding, we show that in the isotropic limit the matrix, properly inverted, is composed of a pair of independently operating submatrices, and these are identified as the 2 x 2 Abelès matrices connected to the s and p-polarization modes. When the same procedure is systematically applied for different anisotropic cases, the results attained by Schopper (1952), Bousquet (1957a), and Holmes and Feucht (1966) arise quite naturally.

In principle, apart from a few mathematical singularities, the theory is capable of producing the results of all treatments previously mentioned. At the end of Chapter 3 we go beyond them and consider the interaction of normally incident light with a stratified system composed of anisotropic layers, each with an arbitrary orientation of its optical axes (here a convenient vector operation is defined to greatly simplify the formalism).

A computer program was developed to turn the above considerations into a practical tool. It is briefly described in the beginning of Chapter 5. To determine reflectances and transmittances corresponding to an anisotropic multilayer system, each of its component layers (biaxial in the most general case) is specified by three pairs of principal optical constants, a physical thickness, and the direction of

columnar growth (which represents the average preferential orientation in the film microstructure).

The last of these is easily obtained from the so-called tangent rule

$$\text{tg}\phi \ = \ \frac{1}{2} \ \text{tg}\nu, \tag{1.1}$$

where ϕ is the columnar orientation angle and ν is the angle of vapor incidence, both with respect to the substrate normal. This identity was first experimentally determined by Nieuwenhuizen and Haanstra (1966) and its universality has been confirmed for a large number of film materials, as shown in Figure 1.2 with data from several investigators collected by Leamy, Gilmer, and Dirks (1980). The observation that the columns are oriented closer to the substrate normal than the vapor beam dates back to 1950. At that time, König and Helwig also stated that the anisotropic structures they observed with an electron microscope in obliquely deposited films was apparently due to shadowing of the impinging molecules by molecules already settled within the growing film. This idea has been recently supported by computer simulations of thin film growth (Dirks and Leamy, 1977), and the tangent rule statistically interpreted in terms of a stochastic process. The geometrical nature of the "self-shadowing" effect, as it is called, is evidenced by the fact that the models utilized for the simulated growth are able to reproduce the main structural features of the films without
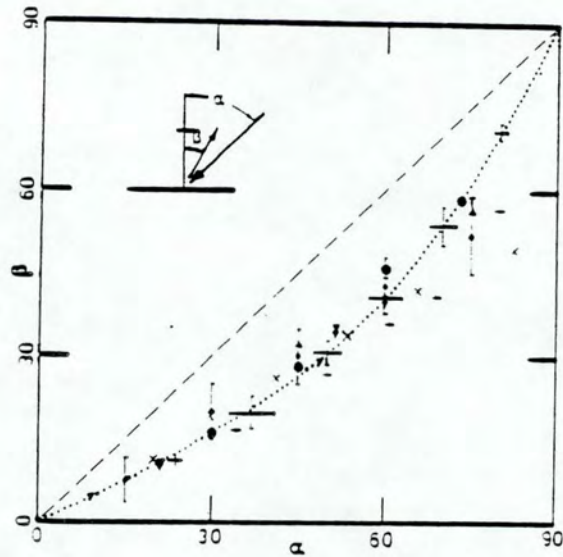
Figure 1.2. The Tangent Rule is Illustrated with Data from Several Investigators and a Variety of Film Materials.

The rule is obeyed well for all situations except for the data shown at + and x, which has been traced to a geometrical artifact of that particular experiment. Here α is the vapor angle of incidence and β is the columnar orientation angle. (From Leamy, Gilmer, and Dirks, 1980.)

taking into account crystalline texture, oxygen adsorption, momentum, or facet formation (Dirks, Leamy, and Gilmer, 1980).

With respect to the physical thickness, it can be determined by the observation of fringes of equal chromatic order (FECO) or by a stylographic measurement, as well as by simply counting repeated patterns of colored fringes with the simple technique we used for the obliquely deposited film we consider in Chapter 4.

On the optical constants of such anisotropic films, however, quantitative information is extremely scarce, if not absent, in the literature. For that reason we present a method that interprets ellipsometric measurements in light of the film columnar microstructure, and whose calculations can be performed with a simple pocket calculator.

In 1960, Bousquet and Rouard, reviewing experiments performed for a decade involving the determination of optical constants in thin films and their theoretical framework, concluded "...it well seems that the granular structure of the films remains the main cause for the anomalies observed in the optical constants...." (our translation)

We hope our method will facilitate the understanding of these anomalies during the course of the vast amount of work that lies ahead in this area.

Following the description of the method, a simple model of the microstructure is considered. The columns are taken as solid rods of infinite length with elliptical cross section and refractive index of the bulk material randomly distributed in an air matrix. A plausibility

argument is then presented that shows reasonable agreement between model predictions and measured values of the principal refractive indices.

Another clear realization that arises from the interpretation of the experiment, in the framework of the theory we have developed, is that Brewster's law does not hold for anisotropic media, films deposited at normal incidence included. A simple explanation for this is discussed, and a more general expression attained through the more fundamental "admittance-matching" between the two media involved. For practical reasons, this expression is derived for the case in which one principal axis is perpendicular to the plane of incidence so that it still retains some of the simplicity of Brewster's law, while reducing to it in the isotropic limit.

With the above considerations, we finally arrive at a stage in which the intersection between the two trends can be undertaken. In Chapter 5 we compare theory and experiment of transmittance measurements with variations of angle of incidence and azimuth angle for a simple dielectric film, as well as with respect to the spectral behavior of a narrowband filter with 21 layers. The properties of a hypothetical metal film are discussed at the end, in parallel with the aluminum sample deposited at 85° described in Chapter 2.

In the last chapter we summarize the results from this work and their possible extensions, followed by potential applications and further suggestions for future work.

A simplified map of our approach, as it was initially idealized, is shown in Figure 1.3.
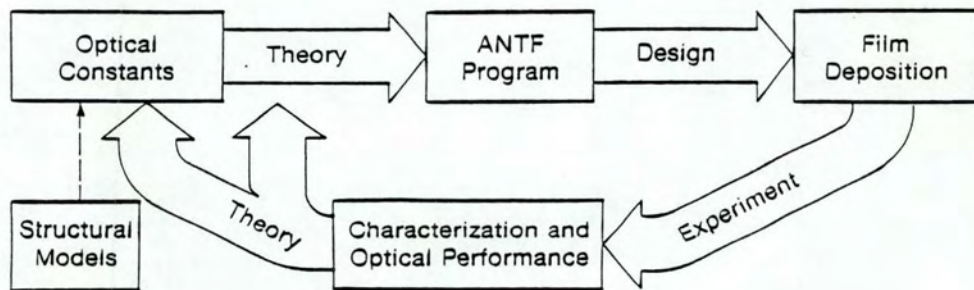
Figure 1.3. A Simplified Map of Our Approach.

CHAPTER 2

POLARIZATION EFFECTS IN METAL AND DIELECTRIC FILMS

We consider in this chapter the major features of the anisotropic
microstructure contribution to the polarization effect in thin films
deposited at high angles of vapor incidence. Previous reports that metal
films mainly respond as polarizers under such conditions are confirmed.
Structural anisotropy in dielectric films, rather than affecting the
extinction coefficient values differently along different directions,
seems to induce significant asymmetry in the refractive index values
that enables us to find a retarder-like behavior. Quantitative analysis
of the effect under normal incidence light at 632.8 nm is presented for
aluminum and zirconium oxide films, and its structural origin is
discussed.

Sample Preparation and Characterization

The films were vapor deposited by thermal evaporation in vacuo
on glass substrates at room temperature and pressures of the order of
10^{-6} Torr. Prior to the deposition of the semitransparent aluminum and
zirconium oxide films, the substrates were positioned to allow average
vapor angles of incidence of 85° and 70° respectively. The distance
between sources and substrates was approximately 250 mm. A directly
heated tungsten spiral was used as the aluminum source. An electron-
beam source with water-cooled copper hearth was used for the zirconium
oxide.

An ellipsometer with Glan-Thompson polarizers that provided extinction ratios of at most one part in 10^6 was adapted to function as a polarimeter (Figure 2.1). The source was a single-mode HeNe laser, followed by a neutral density filter and a quarterwave plate that converted the plane polarized laser output to circularly polarized light. The neutral density filter and quarterwave plate together ensured that the signal was processed in the linear region of the photomultiplier whatever the orientation of the polarizer (a more detailed description of the apparatus is presented in Chapter 4).

Film thicknesses were determined with a profilometer, as well as with the fringes of equal chromatic order (FECO) technique.

Results and Discussion

Figures 2.2(a), (b) and (c) show the observed polarization response of an aluminum film as it was rotated around an axis defined by a normally incident light beam. The p-polarization was arbitrarily chosen to be horizontal. All measured values are relative to a direct signal obtained in the absence of the sample. In the following, the transmittance is indicated by the symbols T_{pp}, T_{ss}, T_{ps}, and T_{sp} where the first subscript indicates polarizer orientation and the second that of the analyzer. The initial angular position of the film was set so that the projection of its optical axis, determined by the direction of columnar growth,[5] along the glass-film interface was vertical.

Figures 2.2(a) and (b) show a significant difference between the ordinary and projected extraordinary direction transmittances. Slocum has presented a plausible explanation for this effect based on the idea
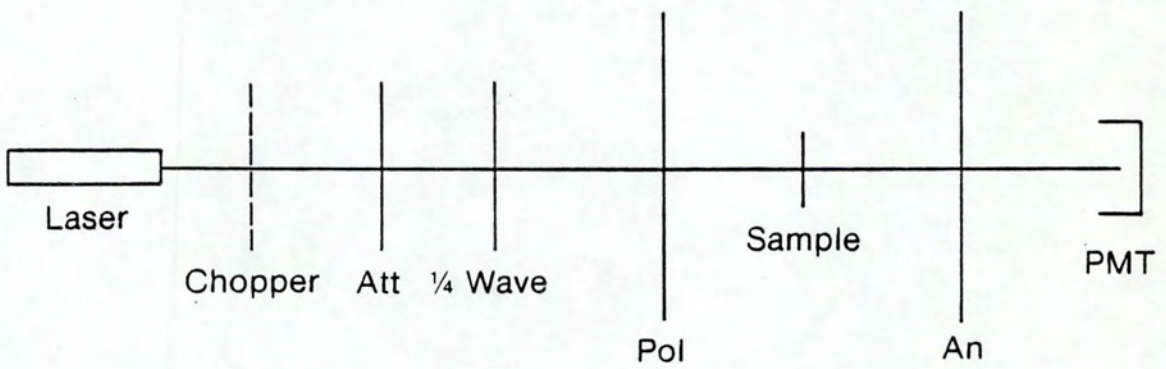
Figure 2.1. Characterization Setup.
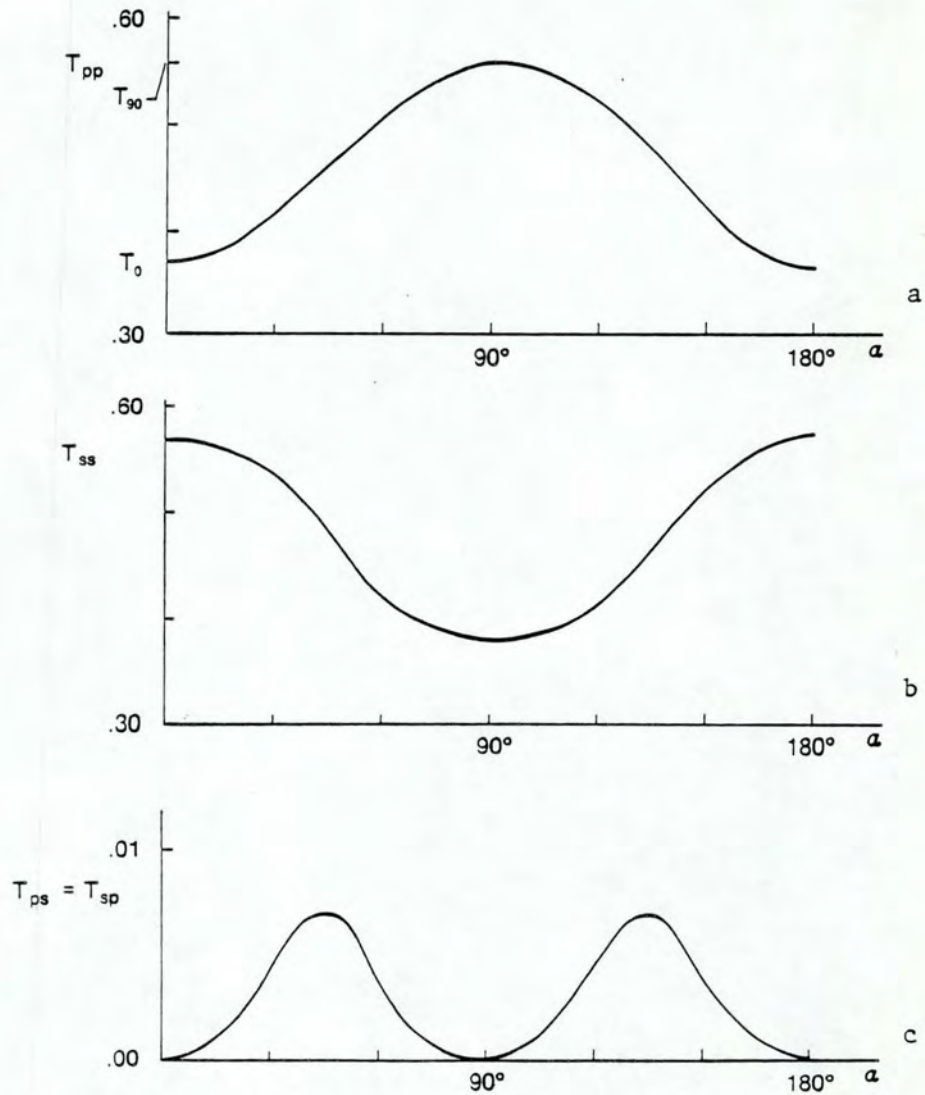
Figure 2.2. Relative Transmittances Measured as Functions of the Sample Rotation Angle for an Aluminum Sample (Al, AN 0326-85).

Error = ±0.01 for (a) and (b) and ±0.001 for (c). Since curve (b) should simply be curve (a) shifted by 90°, their equality can be used to confirm the alignment of the equipment and as a check of consistency.

of a wire grid Hertzian polarizer,[3] but the film seems to be most transmissive along the columnar direction. This property seems to be peculiar to the much smaller dimensions of the columns and their relative closeness.

It is well known that metals have extinction coefficients much larger than refractive indices in the visible. This allows us to approximately describe our aluminum film as a polarizer, based on the following reasoning. If we decompose an incident field at 45° into its components along the ordinary and projected extraordinary coordinates, each experiencing a different attenuation as indicated by T_0 and T_{90} in Figure 2a, and project the resulting fields along the direction coplanar and orthogonal to the original one, we will obtain the resulting transmittance:

$$T_{ps}^{(45°)} = \frac{1}{4} [T_{90}^{1/2} - T_0^{1/2}]^2 \simeq 0.005, \tag{1}$$

which roughly reproduces the observed value in Figure 2c.

This allows us to easily estimate the effective extinction coefficient difference:

$$\Delta k \simeq \frac{\lambda}{4\pi d} \ln \left(\frac{T_{90}}{T_0}\right) = 1.44, \tag{2}$$

where d = 14.5 nm is the measured thickness of the film.

To observe the birefringence effect in a dielectric, we deposited a 4.6-μm thick layer of zirconium oxide. The resulting data are shown in Figures 2.3(a) and (b). The polarization effect here, as opposed to that for aluminum, is due mainly to a refractive index variation. From a retarder point of view, we can estimate the effective amount of birefringence with the aid of Figure 2.3(a). We define a potential transmittance at 45°, indicated by $\psi_{pp}(45°)$, as

$$\psi_{pp}(45°) = \frac{T_{45}}{T_0}, \qquad (3)$$

where T_0 and T_{45} are the transmittances at $\alpha = 0°$ and $45°$ respectively in Figure 2.3(a). The decomposition of an incident p-polarized field at 45° into its ordinary and projected extraordinary components, which become phase-separated by $\Delta\phi$ as they travel along the material, and their subsequent projection back to the p-polarization direction yield

$$\psi_{pp}(45°) = \cos^2 \left(\frac{\Delta\phi}{2}\right). \qquad (4)$$

From Equations (3) and (4) we obtain the effective amount of birefringence

$$\Delta n = \frac{\lambda}{\pi d} \cos^{-1} \left(\frac{T_{45}}{T_0}\right)^{1/2} = 0.042. \qquad (5)$$

This actually sets a lower limit to Δn since there are many possible
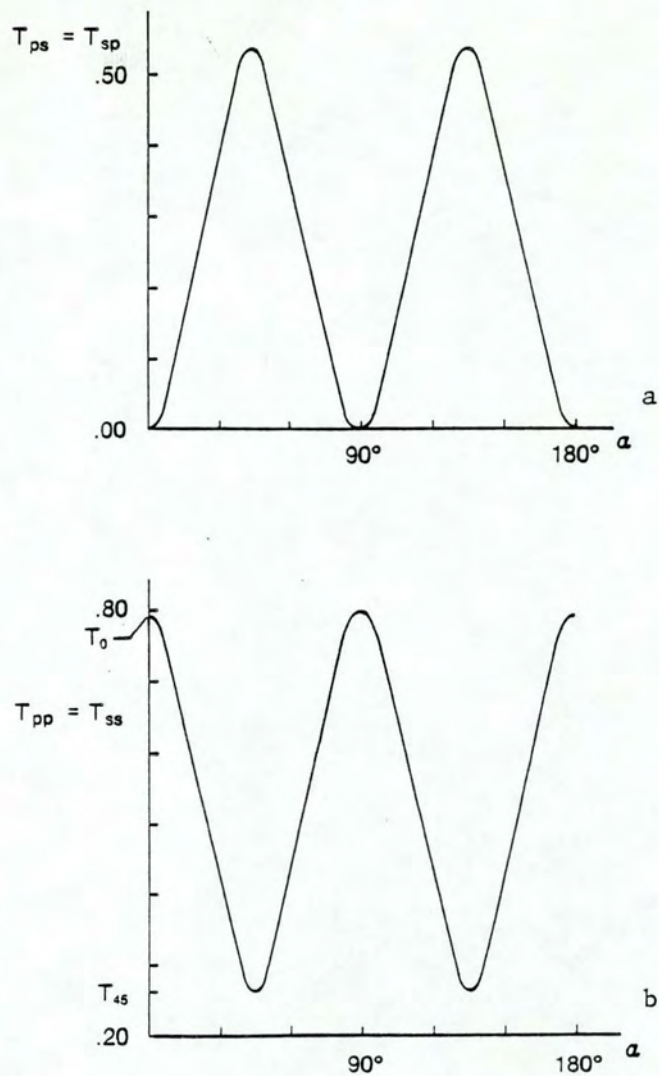
Figure 2.3.   Relative Transmittances Measured as Functions of the Sample
               Rotation Angle for a Zirconium Oxide Sample (Zr oxide, EL
               0124t-70).

               Error = ±0.01. The 90° period permits us to write T_{pp} =
               T_{ss} in curve (a).

values of $\Delta\phi$ that satisfy identity (4). The samples we have observed so far apparently point toward this lower value, but we are still intending to look at more samples over a wide thickness range to make this result more conclusive.

Structural Origin

There are many reports in the literature of thin film characterization by transmission electron microscopy of shadowed direct carbon replicas. Particularly relevant to the present study are the works by Guenter and Pulker (1976) and Nieuwenhuizen and Haanstra (1966) (where micrographs of excellent quality are reproduced. Our own measurements were similar and quite consistent with these earlier results. Column dimensions in each sample showed a spread in sizes but almost all were in the range of 30 to 100 μm diameter. These results, as well as the directional character of the polarization effect we have discussed, indicate the columnar growth origin of the effect.

Although the results that have been quoted refer to either aluminum or zirconium oxide films, these effects have also been observed in preliminary work on silver, copper, and titanium oxide films, all of which have a pronounced columnar structure. In addition, scattering measurements made on some of our samples at the Center for Thin-Film Studies in Marseille (Flory, 1978; Bousquet, Fory and Roche, 1981) have shown anisotropy related to a narrow range of sizes only. This behavior is particularly pronounced in Figures 2.4(a) and 2.4(b) for a silver film.
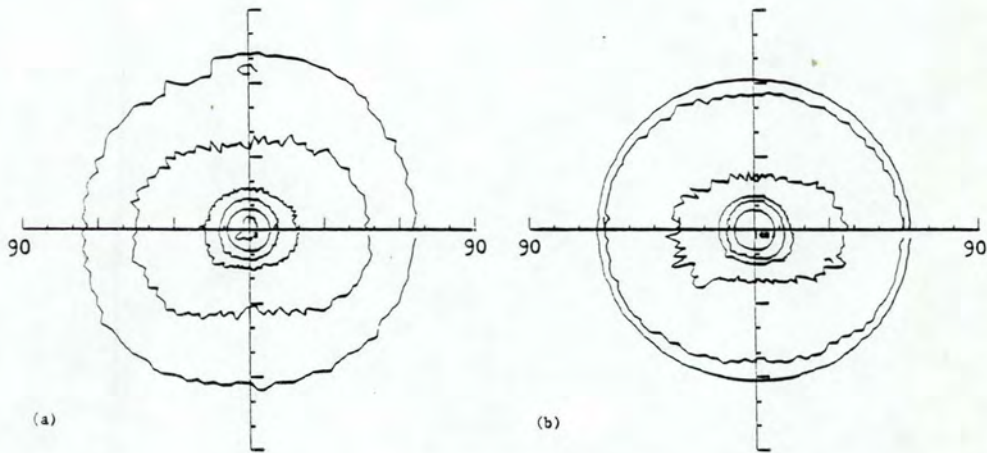
Figure 2.4. Scattering in (a) Reflection and (b) Transmission from an Anisotropic Silver Film.

Note the marked anisotropy of the third contour in (b) while the others are circular. The receiver analyzer is parallel to the plane of polarization of the incident light. The lines are constant intensity contours. Relative intensities, outer to inner, are 5×10^{-6}, 1×10^{-5}, 2×10^{-5}, 4×10^{-5}, 1×10^{-4}, and 1×10^{-3}. (Sample AG10A90)

The almost universal columnar structure of vacuum-deposited films[5] suggests strongly that behavior similar to that which we have reported should be observed in films of virtually any material.

Up to this point we have assumed a uniaxial film microstructure, with the optical axis along the columnar direction. However, experimental evidence, obtained from transmission electron microscopy observations with the electron beam parallel to the columnar orientation (Leamy, Gilmer and Dirks, 1980), has shown that for a more detailed study columns should be taken with an elliptical cross section elongated in a perpendicular direction to that of the vapor incidence. For that reason, in the theoretical analysis that follows, the microstructure is considered in the most general biaxial configuration.

CHAPTER 3

A UNIFIED MATRIX FORMULATION FOR
ANISOTROPIC MULTILAYER SYSTEMS

In this chapter we consider a general theory for stratified anisotropic media with the purpose of understanding the anisotropic optical behavior reported in Chapter 2 from electromagnetic principles. This understanding will later allow us to present a computer program developed as a test for anisotropic multilayer design.

Starting from Maxwell equations, we recreate the Teitler and Henvis formalism (1970), with homogeneous thin film multilayer systems in mind. We specialize to isotropic media (CASE 0), anisotropic media with linear polarization modes (CASE 1), and later to anisotropic media with elliptical polarization modes (CASE 2). In CASE 0, we show that the formalism can be reduced to Abelès treatment (1950) traditionally used for isotropic multilayer films. In CASE 1, we reproduce the results previously obtained by several authors for particular configurations, and form the basic framework for the experimental determination of the principal refractive indices of a biaxial dielectric film (see Chapter 4). With those indices as ad hoc parameters, the optical properties predicted from CASE 1 and CASE 2 treatments will ultimately be compared with the corresponding experimental results in Chapter 5.

23

The Propagation Matrix

We begin by recalling the curl Maxwell equations in a linear, nonmagnetic and polarizable medium in the Gaussian system

$$\nabla \times \mathbf{E} = -\frac{1}{c}\frac{\partial \mathbf{B}}{\partial t} \qquad (3.1)$$

$$\nabla \times \mathbf{H} = \frac{1}{c}\frac{\partial \mathbf{D}}{\partial t} + \frac{4\pi}{c}\mathbf{J}, \qquad (3.2a)$$

where

$$\mathbf{B} = \mu_0 \mathbf{H}, \qquad \mu_0 = 1 \qquad (3.3)$$

$$\mathbf{D} = \epsilon \mathbf{E}, \qquad \mathbf{J} = \sigma \mathbf{E}. \qquad (3.4)$$

From (3.4), (3.2a) can be rewritten

$$\nabla \times \mathbf{H} = \frac{1}{c}\epsilon_{eff}\frac{\partial \mathbf{E}}{\partial t}, \qquad \epsilon_{eff} = \epsilon + 4\pi\sigma. \qquad (3.2b)$$

For simplicity we will refer to the effective "dielectric" tensor ϵ_{eff} as ϵ, while still allowing it to be nonreal, asymmetric, or non-Hermitian as a result of current contributions.

We assume that the electromagnetic fields propagate within the medium as attenuated plane waves,

$$\mathbf{E} = \mathbf{E}(z)\exp\left[-i(\frac{S\omega}{c}x - \omega t)\right]$$

$$\mathbf{H} = \mathbf{H}(z)\exp\left[-i(\frac{S\omega}{c}x - \omega t)\right], \qquad (3.5)$$

where $S = n_0 \sin\theta_0$, and the geometry shown in Figure 3.1 is understood.

Expansion of the field amplitude vectors into their components along the coordinate axes,
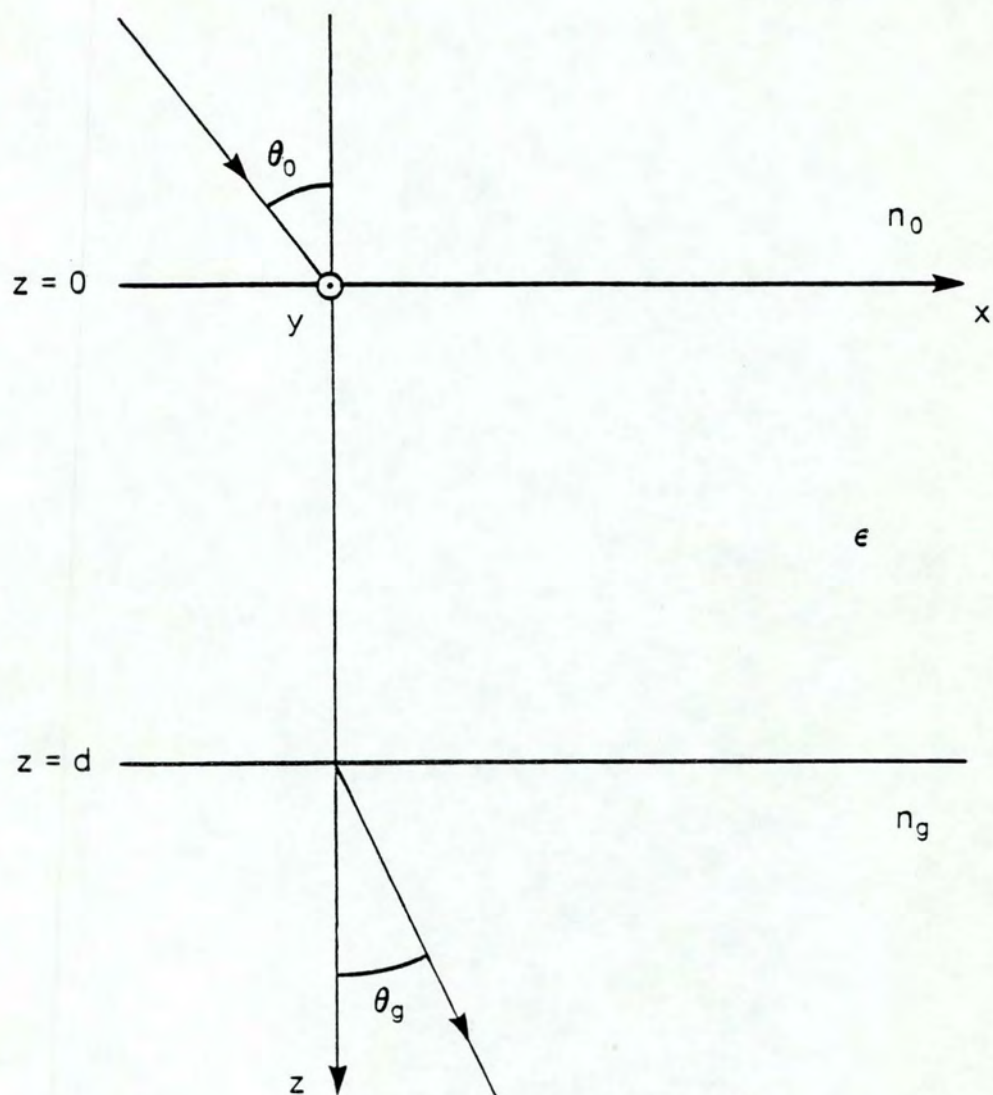
Figure 3.1. Geometry for Refraction in Anisotropic Media.

$$\mathbf{E}(z) \;=\; \sum_{j=1}^{3} E_j(z)\,\hat{e}_j$$

$$\tag{3.6}$$

$$\mathbf{H}(z) \;=\; \sum_{j=1}^{3} H_j(z)\,\hat{e}_j \;; \qquad (\hat{e}_1,\hat{e}_2,\hat{e}_3) \equiv (\hat{x},\hat{y},\hat{z}),$$

followed by direct substitution into (3.1) and (3.2b), leads to six component equations which for $\varepsilon_{33} \neq 0$ allow us to eliminate $E_3(z)$ and $H_3(z)$. If we simplify our notation through the identities,

$$u_n \equiv E_n(z),\; u_{n+2} \equiv H_n(z) \;;\quad n = 1,2$$

and

$$D \equiv \frac{c}{i\omega}\,\frac{d}{dz}\,,$$

the remaining four equations become

$$Du_1 \;=\; c_{11}u_1 + c_{12}u_2 + c_{14}u_4$$
$$Du_2 \;=\; u_3$$
$$Du_3 \;=\; c_{31}u_1 + c_{32}u_2 + c_{34}u_4 \tag{3.7}$$
$$Du_4 \;=\; c_{41}u_1 + c_{42}u_2 + c_{44}u_4\,,$$

where

$$c_{11} = \frac{S}{\varepsilon_{33}}\,\varepsilon_{31} \qquad c_{12} = \frac{S}{\varepsilon_{33}}\,\varepsilon_{32} \qquad c_{14} = \frac{S}{\varepsilon_{33}}\,S - 1$$

$$c_{31} = \varepsilon_{21} - \varepsilon_{31}\frac{\varepsilon_{23}}{\varepsilon_{33}} \qquad c_{32} = \varepsilon_{22} - S^2 - \varepsilon_{32}\frac{\varepsilon_{23}}{\varepsilon_{33}} \qquad c_{34} = -S\frac{\varepsilon_{23}}{\varepsilon_{33}}$$

$$c_{41} = \varepsilon_{31}\frac{\varepsilon_{13}}{\varepsilon_{33}} - \varepsilon_{11} \qquad c_{42} = \varepsilon_{32}\frac{\varepsilon_{13}}{\varepsilon_{33}} - \varepsilon_{12} \qquad c_{44} = -S\frac{\varepsilon_{13}}{\varepsilon_{33}}\,.$$

$$\tag{3.8}$$

Any solution of the system of four linear equations (3.7) can be expressed as a linear combination of four independent solutions. Teitler and Henvis (1970) suggest we choose these, called u^{α} (α=a,b,c,d), with components $u_{\beta}{}^{\alpha}$ (β=1,2,3,4) that satisfy the boundary conditions

$$u_{\beta}{}^{\alpha}(z=0) = \delta_{\alpha\beta}, \tag{3.9}$$

where $\delta(\alpha\beta)$ is the Kronecker delta function, and collect them to form the matrix

$$L(z) = \begin{bmatrix} u_1{}^a(z) & u_1{}^b(z) & u_1{}^c(z) & u_1{}^d(z) \\ u_2{}^a(z) & u_2{}^b(z) & u_2{}^c(z) & u_2{}^d(z) \\ u_3{}^a(z) & u_3{}^b(z) & u_3{}^c(z) & u_3{}^d(z) \\ u_4{}^a(z) & u_4{}^b(z) & u_4{}^c(z) & u_4{}^d(z) \end{bmatrix} . \tag{3.10}$$

This matrix has the property of mapping the tangential field component $u_{\beta}{}^0$ at the interface $z = 0$ onto the corresponding components $u_{\beta}(z)$ at $z \geq 0$ within the same medium:

$$\begin{bmatrix} u_1 \\ u_2 \\ u_3 \\ u_4 \end{bmatrix} = L(z) \begin{bmatrix} u_1{}^0 \\ u_2{}^0 \\ u_3{}^0 \\ u_4{}^0 \end{bmatrix} . \tag{3.11}$$

For that reason, we refer to $L(z)$ as the propagation matrix for one layer. Formally its two-dimensional analog is the inverse of the Abelès (1950) characteristic matrix traditionally used for the isotropic case, as will be shown later.

If N layers are present between 0 and z, (3.11) can be simply extended to

$$\mathbf{u}(z) = \left[\prod_{j=1}^{N} \mathbf{L_j}(z) \right] \mathbf{u^0} , \qquad (3.12)$$

which makes the propagation matrix particularly useful for multilayer systems.

Our interpretation of the Teitler and Henvis prescription can be found in Appendix A. This understanding will later enable us to apply the propagation matrix technique to some cases of practical interest.

The Reflectance and Transmittance Matrices

We now proceed to determine the reflectance and transmittance matrices. We assume that the incident electric field E_o^+ consists of two plane-wave components, i.e.,

$$\mathbf{E_o^+} = \begin{bmatrix} E_{op}^+ \\ \\ E_{os}^+ \end{bmatrix} \exp\left[-i\left(\frac{S\omega}{c} x - \omega t \right) \right]$$

$$(3.13)$$

polarized parallel and perpendicular to the plane of incidence, respectively. Similar conventions for the reflected and transmitted electromagnetic fields are shown in Figure 3.2.

Using the boundary conditions provided by the continuity of the tangential components of the **E** and **H** fields at the interfaces $z = 0$ and $z = d$, and connecting the tangential fields within the anisotropic layer through the L-matrix, we obtain the expressions:

$$a_p^- E_{op}^- + a_s^- E_{os}^- + a_p^+ E_{op}^+ + a_s^+ E_{os}^+ = 0$$

$$(3.14)$$
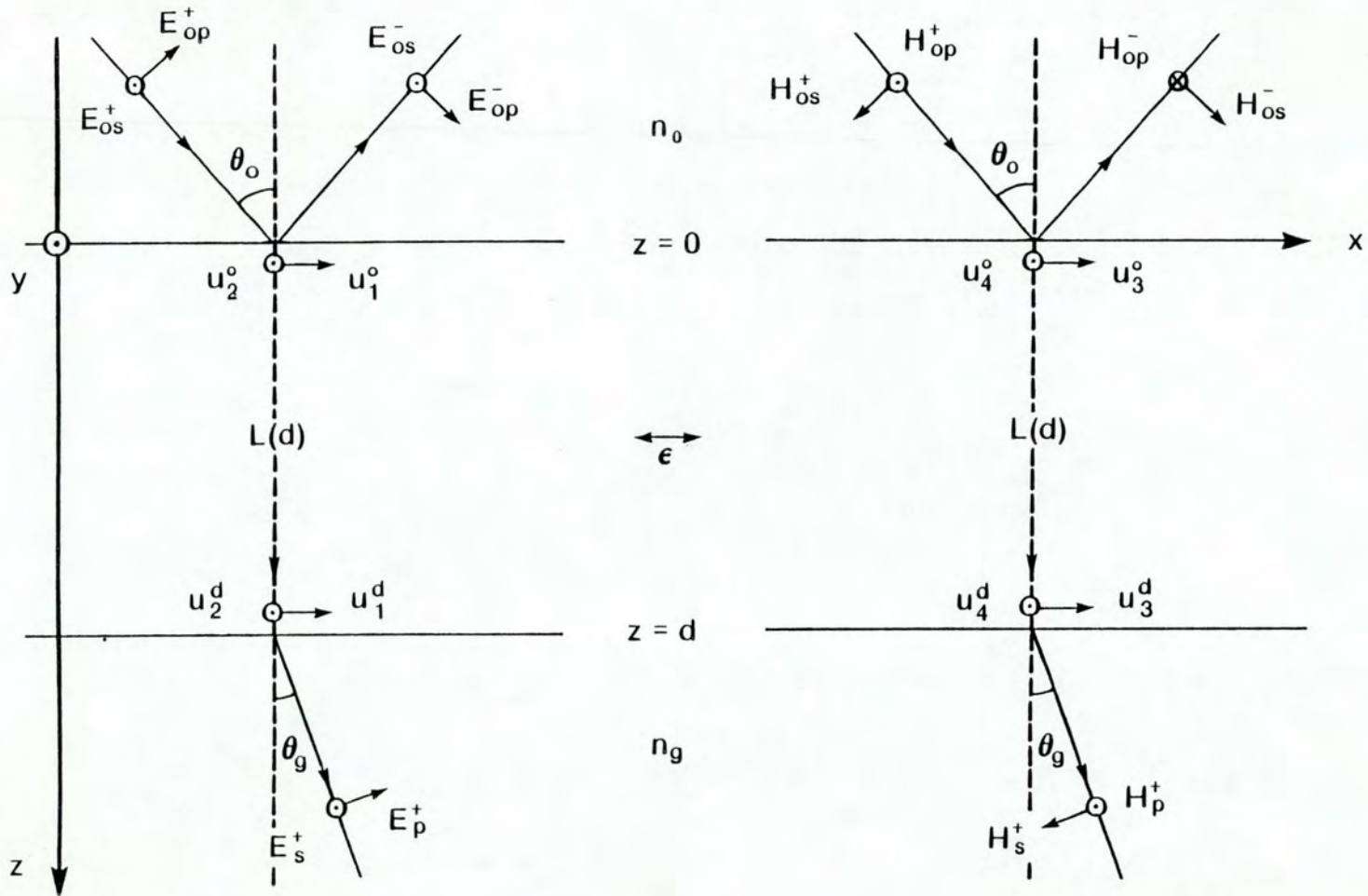
Figure 3.2. Conventions and Schematic for the Determination of the Reflectance and Transmittance Amplitude Coefficients.

$$b_p^- E_{op}^- + b_s^- E_{os}^- + b_p^+ E_{op}^+ + b_s^+ E_{os}^+ = 0,$$

where

$$a_p^\pm = (\ell_{11} \cos\theta_0 \pm \ell_{14} n_0) n_g - (\ell_{41} \cos\theta_0 \pm \ell_{44} n_0) \cos\theta_g$$

$$a_s^\pm = (\ell_{12} \mp \ell_{13} N_0) n_g - (\ell_{42} \mp \ell_{43} N_0) \cos\theta_g$$

$$(3.15)$$

$$b_p^\pm = (\ell_{21} \cos\theta_0 \pm \ell_{24} n_0) N_g + (\ell_{31} \cos\theta_0 \pm \ell_{34} n_0)$$

$$b_s^\pm = (\ell_{22} \mp \ell_{23} N_0) N_g + (\ell_{32} \mp \ell_{33} N_0),$$

with $N_0 = n_0 \cos\theta_0$, $N_g = n_g \cos\theta_g$, and ℓ_{ij} is the ijth element of the **L**-matrix at $z = d$.

We define amplitude reflectance and transmittance matrices by

$$E_o^- = [r] E_o^+$$
$$(3.16)$$
$$E^+ = [t] E_o^+ ,$$

and through (3.14) determine their elements. We get

$$\begin{bmatrix} r_{pp} & r_{ps} \\ r_{sp} & r_{ss} \end{bmatrix} = (a_s^- b_p^- - a_p^- b_s^-)^{-1} \begin{bmatrix} a_p^+ b_s^- - a_s^- b_p^+ & a_s^+ b_s^- - a_s^- b_s^+ \\ a_p^- b_p^+ - a_p^+ b_p^- & a_p^- b_s^+ - a_s^+ b_p^- \end{bmatrix}$$

$$\begin{bmatrix} t_{pp} & t_{ps} \\ t_{sp} & t_{ss} \end{bmatrix} = N_g^{-1} \begin{bmatrix} a_{p1}^- & a_{s1}^- \\ b_{p1}^- & b_{s1}^- \end{bmatrix} \begin{bmatrix} r_{pp} & r_{ps} \\ r_{sp} & r_{ss} \end{bmatrix} + N_g^{-1} \begin{bmatrix} a_{p1}^+ & a_{s1}^+ \\ b_{p1}^+ & b_{s1}^+ \end{bmatrix} ,$$

$$(3.17)$$

where the subscript $_1$ (e.g. α_{p1}^-) refers to the first term of the corresponding quantity in (3.15) (e.g. a_p^-). Note that the last

contribution in the expression above is the amplitude potential transmittance matrix. (Potential transmittance is the maximum transmittance achievable in a system as allowed by material constraints.)

From (3.17) we finally obtain the corresponding reflectance and transmittance matrices

$$[R] = [r*.r] \tag{3.18}$$

$$[T] = \frac{N_g}{N_0} [t*.t] ,$$

where the symbol * denotes the complex conjugate.

Homogeneous Anisotropic Medium

The treatment we have considered up to now is valid for general, inhomogeneous (layered) anisotropic media. Let us apply it to the simpler homogeneous anisotropic case.

Consider a solution basis set consisting of vectors with components

$$u_j(z) = A_j \exp(-ik_0\eta z), \qquad k_0 \equiv \frac{\omega}{c} = \frac{2\pi}{\lambda_0} \tag{3.19}$$

where the A_j's are the constant coefficients, λ_0 is the light wavelength in vacuum and η is a parameter that will be determined later.

Equations (3.7) then take the form

$$(\eta + c_{11})u_1 + c_{12}u_2 + c_{14}u_4 = 0$$

$$\eta u_2 + u_3 = 0 \tag{3.20}$$

$$c_{31}u_1 + c_{32}u_2 + \eta u_3 + c_{34}u_4 = 0$$

$$c_{41}u_1 + c_{42}u_2 + (\eta + c_{44})u_4 = 0.$$

Nontrivial solutions exist for (3.20) provided they satisfy the corresponding secular equation

$$\eta^4 + G_3\eta^3 + G_2\eta^2 + G_1\eta + G_0 = 0, \tag{3.21}$$

where

$$G_3 = c_{11} + c_{44}$$

$$G_2 = c_{11}c_{44} - c_{32} - c_{14}c_{41}$$

$$G_1 = c_{34}c_{42} + c_{12}c_{31} - c_{32}c_{44} - c_{11}c_{32}$$

$$G_0 = c_{11}c_{34}c_{42} + c_{12}c_{31}c_{44} + c_{14}c_{32}c_{41} - c_{11}c_{32}c_{44}$$
$$- c_{12}c_{34}c_{41} - c_{14}c_{31}c_{42}.$$

The quartic equation above becomes a simpler biquadratic when $G_3 = G_1 = 0$. With identities (3.8) in mind, this occurs whenever the ε tensor is diagonal, which characterizes the cases we consider next.

CASE ZERO: The Isotropic Limit

Consider a homogeneous isotropic layer with thickness d, associated with an ε tensor expressed as

$$\begin{bmatrix} \varepsilon & 0 & 0 \\ 0 & \varepsilon & 0 \\ 0 & 0 & \varepsilon \end{bmatrix} . \tag{3.23}$$

From (3.8) it follows that

$$c_{11} = 0 \qquad c_{12} = 0 \qquad c_{14} = \frac{S^2}{\varepsilon} - 1$$

$$c_{31} = 0 \qquad c_{32} = \varepsilon - S^2 \qquad c_{34} = 0$$

$$\tag{3.24}$$

$$c_{41} = -\epsilon \qquad c_{42} = 0 \qquad c_{44} = 0 \quad ,$$

and the secular equation (3.21) becomes

$$\eta^4 + 2(S^2-\epsilon)\eta^2 + (S^2-\epsilon)^2 = 0, \tag{3.25}$$

leading to the allowed η-values

$$\eta^{\mp} \equiv \pm\eta = \pm (\epsilon - S^2)^{1/2}. \tag{3.26}$$

The four component equations (3.20) take the form

$$\pm\eta u_1 - \frac{1}{\epsilon}\eta^2 u_4 = 0$$

$$\pm\eta u_2 + u_3 = 0$$

$$\eta^2 u_2 \pm \eta u_3 = 0 \tag{3.27}$$

$$-\epsilon u_1 \pm \eta u_4 = 0.$$

This is clearly an undetermined equation system that can provide only the ratios

$$\frac{u_4}{u_1} = \pm \frac{\epsilon}{\eta} \qquad \frac{u_3}{u_2} = \pm \eta \quad , \tag{3.28}$$

unless $u_1 = u_4 = 0$ or $u_2 = u_3 = 0$.

We thus form the plane-wave component solutions from

$$u_1 = A_1 \exp(\mp ik_0\eta z) \quad u_2 = A_2 \exp(\mp ik_0\eta z)$$

$$u_4 = \pm A_1 \frac{\epsilon}{\eta} \exp(\mp ik_0\eta z) \quad u_3 = \pm A_2\eta \exp(\mp ik_0\eta z) \tag{3.29}$$

and the above pairs of trivial values.

We take linear combinations of these solutions in such a way that boundary conditions (3.9) are satisfied. For example, take two independent solutions

$$\left[A_1 \exp(-ik_0\eta z), \; 0, \; 0, \; A_1 \frac{\epsilon}{\eta} \exp(-ik_0\eta z) \right]$$

$$\tag{3.30}$$

$$\left[A_1 \ \exp(+ik_0\eta z), \ 0, \ 0, \ -A_1 \ \frac{\epsilon}{\eta} \ \exp(+ik_0\eta z) \right],$$

add them up and choose $A_1 = 1/2$ to obtain

$$u^a = \left[\cos(k_0\eta z), \ 0, \ 0, \ -i \ \frac{\epsilon}{\eta} \ \sin(k_0\eta z) \right], \qquad (3.31a)$$

so that $u^a(z=0) = [1,0,0,0]$, as required. (We are here interchangeably expressing the "column vectors" in Appendix A as "line vectors.)

Similarly,

$$u^b = [0, \ \cos(k_0\eta z), \ -i\eta \ \sin(k_0\eta z), 0] \qquad (3.31b)$$

$$u^c = \left[0, \ \frac{-i}{\eta} \ \sin(k_0\eta z), \ \cos(k_0\eta z), \ 0 \right] \qquad (3.31c)$$

$$u^d = \left[-i \ \frac{\eta}{\epsilon} \ \sin(k_0\eta z), \ 0, \ 0, \ \cos(k_0\eta z) \right] \qquad (3.31d)$$

We are now able to construct the L-matrix representing the propagation of the tangential fields from the $z = 0$ to the $z = d$ interfaces

$$L(z=d) = \begin{bmatrix} \cos\delta & 0 & 0 & -i \ \frac{\eta}{\epsilon} \ \sin\delta \\ 0 & \cos\delta & -\frac{i}{\eta} \ \sin\delta & 0 \\ 0 & -i\eta \ \sin\delta & \cos\delta & 0 \\ -i \ \frac{\epsilon}{\eta} \ \sin\delta & 0 & 0 & \cos\delta \end{bmatrix} \qquad (3.32)$$

where

$$\delta \equiv \frac{2\pi}{\lambda_0} \ \eta d.$$

For simplicity let us examine the case of a single dielectric layer with refractive index n. With $\epsilon = n^2$ and from (3.26):

$$\eta = (n^2 - S^2)^{1/2} = n \cos\theta , \qquad (3.33)$$

where Snell's law was used and θ is the angle of refraction within the

medium. We conveniently reorder the tangential field components to get from (3.32)

$$
\begin{bmatrix} u_1{}^d \\ u_4{}^d \\ u_2{}^d \\ u_3{}^d \end{bmatrix}
\begin{bmatrix}
\cos\delta & -i\,\dfrac{\cos\theta}{n}\sin\delta & 0 & 0 \\[2mm]
-i\,\dfrac{n}{\cos\theta}\sin\delta & \cos\delta & 0 & 0 \\[2mm]
0 & 0 & \cos\delta & -i\,\dfrac{\sin\delta}{n\cos\theta} \\[2mm]
0 & 0 & -in\,\cos\theta\,\sin\delta & \cos\delta
\end{bmatrix}
\begin{bmatrix} u_1{}^0 \\ u_4{}^0 \\ u_2{}^0 \\ u_3{}^0 \end{bmatrix}
$$

$$(3.34)$$

If we recall the convention $[u_1,u_2,u_3,u_4] \equiv [E_x,E_y,H_x,H_y]$ and split the 4×4 propagation matrix above into its 2×2 submatrices, their inverses will provide

$$
\begin{bmatrix} E_x{}^0 \\ H_y{}^0 \end{bmatrix}
=
\begin{bmatrix}
\cos\delta & \dfrac{i}{n_p}\sin\delta \\[2mm]
in_p\sin\delta & \cos\delta
\end{bmatrix}
\begin{bmatrix} E_x{}^d \\ H_y{}^d \end{bmatrix}
$$

$$(3.35)$$

$$
\begin{bmatrix} E_y{}^0 \\ H_x{}^0 \end{bmatrix}
=
\begin{bmatrix}
\cos\delta & \dfrac{i}{n_s}\sin\delta \\[2mm]
in_s\sin\delta & \cos\delta
\end{bmatrix}
\begin{bmatrix} E_y{}^d \\ H_y{}^d \end{bmatrix}
$$

where

$$n_p = \frac{n}{\cos\theta}$$

$$n_s = n\cos\theta$$

and

$$\delta = \frac{2\pi}{\lambda_0} nd \cos\theta.$$

We have just obtained the traditional Abelès (1950) characteristic matrices.

CASE 1: Linear Polarization Modes

Consider a homogeneous anisotropic layer with thickness d whose principal axes, or axes of electrical symmetry, coincide with the coordinate axes defined previously. See Figure 3.3(a) for the corresponding columnar structure configurations. Such a material is associated with an ϵ tensor expressed as

$$\begin{bmatrix} \epsilon_{11} & 0 & 0 \\ 0 & \epsilon_{22} & 0 \\ 0 & 0 & \epsilon_{33} \end{bmatrix} \quad ; \quad \epsilon_{jj} = n_j^2 \quad (j=1,2,3). \tag{3.36}$$

From (3.8) we get the coefficients

$$c_{11} = 0 \qquad c_{12} = 0 \qquad c_{14} = \frac{S^2}{\epsilon_{33}} - 1$$

$$c_{31} = 0 \qquad c_{32} = \epsilon_{22} - S^2 \qquad c_{34} = 0 \tag{3.37}$$

$$c_{41} = -\epsilon_{11} \qquad c_{42} = 0 \qquad c_{44} = 0 \; ,$$

and component equations (3.20) become

$$\eta u_1 + c_{14} u_4 = 0$$

$$\eta u_2 + u_3 = 0 \tag{3.38}$$

$$c_{32} u_2 + \eta u_3 = 0$$

$$c_{41} u_1 + \eta u_4 = 0 \; ,$$

from which we determine the allowed η-values
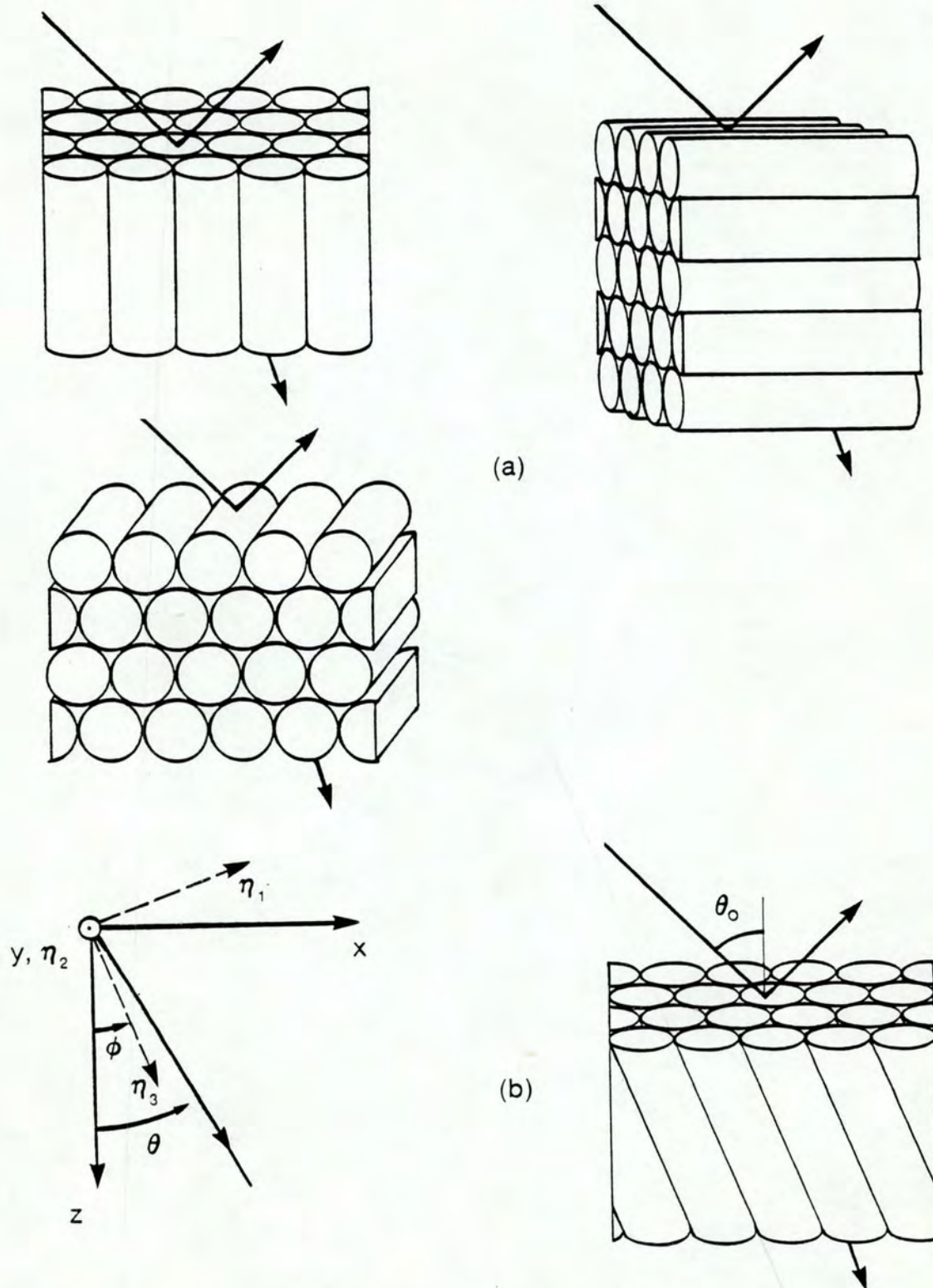
Figure 3.3. Possible CASE 1 Columnar Structure Configurations.

$$\eta_s^{\pm} \equiv \pm\eta_s = \pm(c_{32})^{1/2}$$

$$\eta_p^{\pm} \equiv \pm\eta_p = \pm(c_{14}c_{41})^{1/2}.$$

(3.39)

We have already labeled these two pairs of solutions as s and p because they are independently attached to $\{u_2, u_3\}$ and $\{u_1, u_4\}$, in that order.

The corresponding two pairs of nontrivial component solutions are

$$u_2 = A_2 \exp(\mp ik_0\eta_s) \quad u_1 = A_1 \exp(\mp ik_0\eta_p)$$

(3.40)

$$u_3 = \pm\eta_s A_2 \exp(\mp ik_0\eta_s) \quad u_4 = \pm \frac{\varepsilon_{11}}{\eta_p} A_1 \exp(\mp ik_0\eta_p).$$

We take convenient linear combinations of the basis vectors composed of these and of trivial components, in a manner similar to that shown in the isotropic case, to obtain

$$u^a = \left[\cos(k_0\eta_p z), 0, 0, -i \frac{\varepsilon_{11}}{\eta_p} \sin(k_0\eta_p z)\right]$$

$$u^b = [0, \cos(k_0\eta_s z), -i\eta_s \sin(k_0\eta_s z), 0]$$

(3.41)

$$u^c = \left[0, -\frac{i}{\eta_s} \sin(k_0\eta_s z), \cos(k_0\eta_s z), 0\right]$$

$$u^d = \left[-i \frac{\eta_p}{E_{11}} \sin(k_0\eta_p^2), 0, 0, \cos(k_0\eta_p^2)\right],$$

which satisfy boundary conditions (3.9), as required.

The following propagation matrix at z=d results

$$
L(z=d) = \begin{bmatrix} \cos\delta_p & 0 & 0 & -i\,\dfrac{\eta_p}{\eta_1^{\,2}}\,\sin\delta_p \\[2em] 0 & \cos\delta_s & -\dfrac{i}{\eta_s}\,\sin\delta_s & 0 \\[2em] 0 & -i\eta_s\,\sin\delta_s & \cos\delta_s & 0 \\[2em] -i\,\dfrac{\eta_1^{\,2}}{\eta_p}\,\sin\delta_p & 0 & 0 & \cos\delta_p \end{bmatrix},
$$

$$(3.42)$$

where

$$
\delta_s = \frac{2\pi}{\lambda_0}\,\eta_s d
$$

$$
\delta_p = \frac{2\pi}{\lambda_0}\,\eta_p d \qquad\qquad (3.43)
$$

and

$$
\eta_s^{\,2} = \eta_2^{\,2} - \eta_0^{\,2}\sin^2\theta_0 \,, \quad \eta_p^{\,2} = \frac{\eta^2}{\eta_3^{\,2}}(\eta_3^{\,2}-\eta_0^{\,2}\sin^2\theta_0);
$$

$$
\eta_j^{\,2} \equiv \varepsilon_{jj} \quad (j=1,2,3).
$$

Identities (3.43) are consistent with the results presented by Bousquet (1957a) in the theory he developed for this particular case.

The matrix above is easily split into its two-dimensional submatrices, and by taking their inverses we can write

$$\begin{bmatrix} E_y^0 \\ H_x^0 \end{bmatrix} = \begin{bmatrix} \cos\delta_s & \dfrac{i}{\eta_s}\sin\delta_s \\ i\eta_s\sin\delta_s & \cos\delta_s \end{bmatrix} \begin{bmatrix} E_y^d \\ H_x^d \end{bmatrix}$$

$$\begin{bmatrix} E_x^0 \\ H_y^0 \end{bmatrix} = \begin{bmatrix} \cos\delta_p & i\,\dfrac{\eta_p}{\eta_1^2}\sin\delta p \\ i\,\dfrac{\eta_1^2}{\eta_p}\sin\delta_p & \cos\delta_p \end{bmatrix} \begin{bmatrix} E_x^d \\ H_y^d \end{bmatrix}$$

$$(3.44)$$

Note the similarity between these and matrices (3.35) for the isotropic case. They are the same for $\eta_1 = \eta_2 = \eta_3$, as expected. At normal incidence we get $\eta_s = \eta_2$ and $\eta_p = \eta_1$, and each of the matrices above is still formally equivalent to (3.35). This implies that in this situation the anisotropic layer behaves as if it were isotropic for each polarization mode separately. In other words, the concept of "equivalent (isotropic) admittance" still applies, as long as we think in terms of two "equivalent isotropic layers," one for each polarization mode.

These are the same when $\eta_1 = \eta_2$ ($\neq \eta_3$), which supports the validity of optical measurements performed with normally vapor-deposited films under normal light incidence while still disregarding the anisotropy of the films. However, care must be taken in oblique light incidence measurements, since it is clear from identities (3.43) that anisotropy can significantly influence optical behavior in some cases.

Generalization

An important point to be realized is that a 2×2 matrix treatment is valid if and only if the s- and p-polarized fields are uncoupled. In terms of equations (3.20), for an arbitrary angle of incidence, that means

$$c_{12} = c_{31} = c_{34} = c_{42} = 0, \tag{3.45a}$$

or, from (3.8)

$$\varepsilon_{12} = \varepsilon_{21} = \varepsilon_{23} = \varepsilon_{32} = 0. \tag{3.45b}$$

Whenever these conditions are satisfied, the s- and p-polarized fields will travel independently along the medium. This is always the case when one of them vibrates along one of the principal axes of the material.

Consider the geometry shown in Figure 3.3(b). The principal axis along which an electric field experiences an admittance η_3 is at an arbitrary angle ϕ from the z axis, but still in the plane of incidence. This implies that the s-polarized field is always at another principal axis and thus propagates independently from the p field.

This configuration is still associated with the diagonal ε matrix (3.36) in the principal axes representation. Since these axes are obtainable from the coordinate axes system through a counterclockwise rotation by ϕ around the y axis, as considered in Appendix B, the following coordinate axes representation will result:

$$\begin{bmatrix} \epsilon_{11}\cos^2\phi + \epsilon_{33}\sin^2\phi & 0 & (\epsilon_{11}-\epsilon_{33})\sin\phi\cos\phi \\ 0 & \epsilon_{22} & 0 \\ (\epsilon_{11}-\epsilon_{33})\sin\phi\cos\phi & 0 & \epsilon_{11}\sin^2\phi + \epsilon_{33}\cos^2\phi \end{bmatrix}, \quad (3.46)$$

and the (3.8) coefficients become

$$c_{11} = S\,\frac{\epsilon'_{31}}{\epsilon'_{33}} \qquad c_{12} = 0 \qquad c_{14} = \frac{S^2}{\epsilon'_{33}}$$

$$c_{31} = 0 \qquad c_{32} = \epsilon'_{22} - S^2 \qquad c_{34} = 0 \qquad\qquad (3.47)$$

$$c_{41} = \frac{\epsilon'_{13}\epsilon_{31}}{\epsilon_{33}} - \epsilon'_{11} \qquad c_{42} = 0 \qquad c_{44} = S\,\frac{\epsilon'_{13}}{\epsilon'_{33}}$$

where the ϵ'_{ij}'s $(i,j=1,3)$ refer to the elements of matrix (3.46).

The component equations (3.20) related to the s-polarization mode take the form

$$\eta u_2 + u_3 = 0$$

$$(\epsilon_{22}-S^2)u_2 + \eta u_3 = 0, \qquad\qquad (3.48)$$

from which we obtain

$$\eta_s^2 = \eta_2^2 - S^2 ; \qquad S = n_0\sin\theta_0 . \qquad\qquad (3.49)$$

In the p-polarization case the equations are

$$(\eta+c_{11})u_1 + c_{14}u_4 = 0$$

$$(c_{41}u_1 + (\eta+c_{44})u_4 = 0, \qquad\qquad (3.50)$$

which combined with (3.46) and (3.47) allow us to write the resulting η-solutions in a concise way as

$$\eta_p^{\pm} = -c_{11} \pm g , \qquad\qquad (3.51)$$

where g is such that

$$g^2 = c_{14}c_{41} = \left(1 - \frac{S^2}{\epsilon'_{33}}\right)\eta^2_{po} .$$

For this last identity we have defined the quantity η_{po} so that

$$\frac{1}{\eta^2_{po}} \equiv \frac{1}{c_{41}} = \frac{\cos^2\phi}{\eta_1{}^2} + \frac{\sin^2\phi}{\eta_3{}^2} . \tag{3.52}$$

Since at normal incidence $S = 0$, it is easy to see from (3.51) and (3.47) that

$$\eta_p^{\pm}(\theta_0=0) = \pm\,\eta_{po} . \tag{3.53}$$

From (3.48) and (3.50) we get the nontrivial component solutions

$$u_2 = A_2 \exp(\mp ik_0\eta_s{}^2)$$
$$u_3 = \pm\,\eta_s u_2 \tag{3.54}$$

and

$$u_1 = A_1 \exp(iK_0 c_{11} z) \exp(\mp ik_0 gz)$$
$$u_4 = \pm\gamma u_1 ; \quad \gamma = -\frac{c_{41}}{g} , \tag{3.55}$$

where (3.51) was used.

Proceeding exactly as we did following (3.40), we obtain the propagation matrix at $z = d$

$$\begin{bmatrix} \Phi\cos\delta_p{}' & 0 & 0 & -\dfrac{i\Phi}{\gamma}\sin\delta_p{}' \\[2ex] 0 & \cos\delta_s & -\dfrac{i}{\eta_s}\sin\delta_s & 0 \\[2ex] 0 & -i\eta_s\sin\delta_s & \cos\delta_s & 0 \\[2ex] -i\gamma\Phi\sin\delta_p{}^2 & 0 & 0 & \Phi\cos\delta_p{}' \end{bmatrix} \tag{3.56}$$

where

$$\delta_s = \frac{2\pi}{\lambda_0} \eta_s d, \qquad \delta_p' = \frac{2\pi}{\lambda_0} g d$$

$$\eta_s^2 = \eta_2^2 - S^2, \qquad g^2 = (1 - \frac{S^2}{\epsilon_{33}'}) \eta_{po}^2 \qquad (3.57)$$

$$\phi = \exp(i \frac{2\pi}{\lambda_0} dS \frac{\epsilon_{31}'}{\epsilon_{33}'}), \qquad \gamma = \frac{\eta_{po}^2}{g} .$$

The inverse of the s-submatrix is identical to that in (3.44). As for the p-submatrix, we take its inverse and get

$$\begin{bmatrix} E_x^0 \\ H_y^0 \end{bmatrix} = \phi * \begin{bmatrix} \cos\delta_p' & \frac{i}{\gamma} \sin\delta_p' \\ i\gamma \sin\delta_p' & \cos\delta_p' \end{bmatrix} \begin{bmatrix} E_x^d \\ H_y^d \end{bmatrix} . \qquad (3.58)$$

Careful examination of the results (3.57) and (3.58) shows that they are in agreement with (3.43) and (3.44) in the $\phi = 0$ limit, as expected. They are also consistent with an independent calculation performed by Ian Hodgkinson in connection with the two-dimensional matrix treatment by Holmes and Feucht (1966).

Discussion

We now consider the results we have attained so far for the simple case of a dielectric single layer.

Bearing in mind our comments following (3.44), let n_{eq} be an "equivalent (isotropic) refractive index" that allows us to use Snell's law

$$S \equiv n_0 \sin\theta_0 = n_{eq} \sin\theta. \qquad (3.59)$$

For the s-polarization mode, obviously $n_{eq} = n_2$ at any angle of incidence. This is confirmed by direct comparison between (3.33) and (3.57), Snell's law considered.

To determine η_{eq} for the p-mode we use (3.33) and Snell's law, combined with (3.51) and its auxiliary relations (3.47), (3.46) and (3.52). After a laborious but straightforward algebraic exercise we obtain

$$\frac{1}{n^2_{eq}} = \frac{\cos^2(\theta-\phi)}{n_1^2} + \frac{\sin^2(\theta-\phi)}{n_3^2} . \tag{3.60}$$

In the isotropic limit $n_{eq} = n_1 = n_3$, as expected. This expression is consistent with (3.52) at normal incidence. It also agrees with (3.43) in the $\phi = 0$ limit.

The dependence of n_{eq} on the angle between the wavevector inside the medium and the η_3-axis (see Fig. 3.3(b)) leads us to a simple physical interpretation of (3.60). From it we derive the phase-velocity relation

$$v^2_{eq} = v_1^2 + v_3^2 , \tag{3.61}$$

where $v_{eq} = c/n_{eq}$; v_1 and v_3 are the phase velocities, in the plane of incidence, respectively perpendicular to the η_1 and η_3 axes. In other words, Snell's law can be used as if for an isotropic dielectric layer provided we decompose the "equivalent (isotropic) phase velocity vector" v_{eq} into its components along the principal axes, whose contributions account for the angular dependence of n_{eq} according to expression (3.60).

CASE 2: Elliptical Polarization Modes

Consider a homogeneous anisotropic layer with thickness d whose principal axes system is at an arbitrary orientation. A general ϵ tensor, expressed in the coordinate axes representation by the matrix

$$\begin{bmatrix} \varepsilon'_{11} & \varepsilon'_{12} & \varepsilon'_{13} \\ \varepsilon'_{21} & \varepsilon'_{22} & \varepsilon'_{23} \\ \varepsilon'_{31} & \varepsilon'_{32} & \varepsilon'_{33} \end{bmatrix} \qquad (3.62)$$

can be easily obtained from the principal axes diagonal representation as shown in Appendix B.

Identities (3.22) and (3.8) in mind, the quartic equation (3.21) simplifies to a biquadratic whenever $S = 0$. It is fortunate that we can still find an analytical solution for all normal incidence configurations, which constitute most circumstances of practical interest.

For $S = 0$ the (3.8) coefficients become

$$c_{11} = 0 \qquad\qquad c_{12} = 0 \qquad\qquad c_{14} = -1$$

$$c_{31} = \varepsilon'_{21} - \varepsilon'_{31} \frac{\varepsilon'_{23}}{\varepsilon'_{33}} \qquad c_{32} = \varepsilon'_{22} - \varepsilon'_{32} \frac{\varepsilon'_{23}}{\varepsilon'_{33}} \qquad c_{34} = 0$$

$$c_{41} = \varepsilon'_{31} \frac{\varepsilon'_{13}}{\varepsilon'_{33}} - \varepsilon'_{11} \qquad c_{42} = \varepsilon'_{32} - \frac{\varepsilon'_{13}}{\varepsilon'_{33}} - \varepsilon'_{12} \qquad c_{44} = 0 \ ,$$

$$(3.63)$$

so that the secular equation (3.21) can be written

$$\eta^4 + G_2 \eta^2 + G_0 = 0,$$

where

$$G_2 = -c_{32} - c_{14} c_{41} \qquad\qquad (3.64)$$

$$G_0 = c_{14}(c_{32} c_{41} - c_{31} c_{42}).$$

We then obtain two pairs of allowed η-values

$$\eta_1^{\pm} \equiv \pm\eta_1 = \pm \left(\frac{-G_2+F}{2}\right)^{1/2} \qquad (3.65)$$

$$\eta_2^{\pm} \equiv \pm\eta_2 = \pm \left(\frac{-G_2-F}{2}\right)^{1/2}$$

where

$$F = ((G_2)^2 - 4G_0)^{1/2}.$$

The nontrivial component solutions to equations (3.20) associated with the first pair of η-values are

$$u_1(\eta_1) = A_1 \exp(-ik_0\eta_1 z)$$

$$u_2(\eta_1) = r_{21}(\eta_1) \cdot u_1 ; \qquad r_{21}(\eta_1) = (\eta_1^2 - c_{14}c_{41})/c_{14}c_{42} \qquad (3.66)$$

$$u_3(\eta_1) = r_{31}(\eta_1) \cdot u_1 ; \qquad r_{31}(\eta_1) = -\eta_1 r_{21}(\eta_1)$$

$$u_4(\eta_1) = r_{41}(\eta_1) \cdot u_1 ; \qquad r_{41}(\eta_1) = -(c_{41} + c_{42}r_{21}(\eta_1))/\eta_1.$$

(The last of identities (3.66) is not in agreement with the corresponding expression for r_{41} presented by Teitler and Henvis (1970), which, as printed in p. 832 of their article, requires a sign correction.) Similar nontrivial component solutions hold in connection with the second pair of admittances. They are directly obtained from (3.66) by performing the changes $A_1 \rightarrow A_2$ and $\eta_1 \rightarrow \eta_2$.

At this point we note that r_{21}, r_{31}, and r_{41} are functions with well-defined parity with respect to the η-values. This allows us to follow naturally the procedure used in previous cases to determine the propagation matrix.

We take the first two independent solutions

$$\omega_1 = [u_1(\eta_1), r_{21}(\eta_1)u_1(\eta_1), r_{31}(\eta_1)u_1(\eta_1), r_{41}(\eta_1)u_1(\eta_1)]$$

$$(3.67)$$

$$\omega_2 = \omega_1(-\eta_1)$$

$$= [u_1(-\eta_1), r_{21}(\eta_1)u_1(-\eta_1), -r_{31}(\eta_1)u_1(-\eta_1), -r_{41}(\eta_1)u_1(-\eta_1)]$$

and sum them up at $z = d$ to get

$$\omega_{12} = 2A_1[\cos\delta_1, r_{21}(\eta_1)\cos\delta_1, -ir_{31}(\eta_1)\sin\delta_1, -ir_{41}(\eta_1)\sin\delta_1],$$

$$(3.68a)$$

where we have used the identity

$$\delta_i \equiv \frac{2\pi}{\lambda_0} n_i d ; \qquad i = 1,2. \tag{3.69}$$

Similarly we obtain from the second pair of independent solutions

$$\omega_{34} = 2A_2[\cos\delta_2, r_{21}(\eta_2)\cos\delta_2, -ir_{31}(\eta_2)\sin\delta_2, -ir_{41}(\eta_2)\sin\delta_2].$$

$$(3.70a)$$

To simplify the notation, let us define the "direct vector product" operation @ such that, given two arbitrary vectors

$$a \equiv [a_1, a_2, a_3, a_4]$$

and

$$b \equiv [b_1, b_2, b_3, b_4],$$

$$a @ b \equiv [a_1 b_1, a_2 b_2, a_3 b_3, a_4 b_4]. \tag{3.71}$$

With this in mind, we can rewrite (3.68a) and (3.70a) as

$$\omega_{12} = 2A_1 \, p(\delta_1) @ r(\eta_1) \tag{3.68b}$$

$$\omega_{34} = 2A_2 \, p(\delta_2) @ r(\eta_2), \tag{3.70b}$$

where

$$p(\delta_i) \equiv [\cos\delta_i, \cos\delta_i, -i\sin\delta_i, -i\sin\delta_i] \tag{3.72}$$

$$r(\eta_i) \equiv [1, r_{21}(\eta_i), r_{31}(\eta_i), r_{41}(\eta_i)]; \qquad i=1,2. \tag{3.73}$$

We now take the difference

$$u^a = \omega_{12} - \omega_{34} = 2A_1 \, p(\delta_1) \, @ \, r(\eta_1) - 2A_2 \, p(\delta_2) \, @ \, r(\eta_2), \tag{3.74}$$

and choose

$$2A_2 = \frac{r_{21}(\eta_1)}{r_{21}(\eta_2)-r_{21}(\eta_1)} \, , \qquad 2A_1 = \frac{r_{21}(\eta_2)}{r_{21}(\eta_1)} \, 2A_2 \tag{3.74a}$$

so that $u^a(d=0) = [1,0,0,0]$, as required by (3.9).

In a similar way we get

$$u^b = u^a \text{ (formally)},$$

where now the choice is

$$2A_1 = 2A_2 = [r_{21}(\eta_1) - r_{21}(\eta_2)]^{-1}. \tag{3.74b}$$

The other two solution vectors are

$$u^{c \text{ or } d} = 2A_1 \, q(\delta_1) \, @ \, r(\eta_1) - 2A_2 \, q(\delta_2) \, @ \, r(\eta_2), \tag{3.75}$$

where

$$q(\delta_i) = [-i \, \sin\delta_i, \, -i \, \sin\delta_i, \, \cos\delta_i, \, \cos\delta_i]; \quad i=1,2$$

and u^c:

$$2A_1 = \frac{r_{41}(\eta_2)}{r_{31}(\eta_1)r_{41}(\eta_2)-r_{41}(\eta_1)r_{31}(\eta_2)} \, , \qquad 2A_2 = \frac{r_{41}(\eta_1)}{r_{41}(\eta_2)} \, 2A_1$$

$$\tag{3.75a}$$

for u^d

$$2A_1 = \frac{-r_{31}(\eta_2)}{r_{31}(\eta_1)r_{41}(\eta_2)-r_{41}(\eta_1)r_{31}(\eta_2)} \, , \qquad 2A_2 = \frac{r_{31}(\eta_1)}{r_{31}(\eta_2)} \, 2A_1.$$

$$\tag{3.75b}$$

The usual construction of the L-matrix follows, with its elements l_{jk} given by the components u_j of the solution vectors

$$l_{j1} = u_j{}^a, \ l_{j2} = u_j{}^b, \ l_{j3} = u_j{}^c, \ l_{j4} = u_j{}^d \ ; \quad j = 1,2,3,4.$$

$$(3.76)$$

Discussion

The detailed final structure of the l_{jk} elements is of no practical interest to us because the above recurrence relations already allow for a compact and systematic calculation in the ANTF program, which will be introduced later. All general expressions (3.12) to (3.18) follow, leading to the determination of the reflectance and transmittance of multilayer systems.

A novel feature that arises in this case is that the cross terms in the amplitude reflectance and transmittance matrices are generally nonzero. When this happens linearly polarized light may become elliptically polarized after interaction with the anisotropic system. Also the p and s-polarizations lose their traditional roles as eigenmodes since, as already evident from equations (3.20) with coefficients (3.63), their corresponding fields may propagate in a coupled manner along the medium, and this is the physical cause for the appearance of the nonzero amplitude cross terms.

It should be mentioned that this problem was also tackled by Goncharenko and Fedorov (1963). However, their treatment applies for normal incidence only and, far from a matrix formulation, is not appropriate for multilayer system calculations. It seems impractical to compare their results with ours.

With regard to expression (3.66), we have implicitly assumed in our treatment that $c_{42} \neq 0$. When $c_{42} = 0$ and $c_{31} = 0$ (also $c_{12} = c_{34} = 0$ for normal incidence), equations (3.20) split into two independent pairs, the s and p-polarized fields travel uncoupled along the medium and we are back to CASE 1. $c_{42} = 0$ implies $c_{31} = 0$ for any lossless medium since, (3.63) considered, no energy loss in the system implies that the ϵ tensor is symmetrical, as elegantly demonstrated in Born and Wolf (1975, p. 666). Consequently the actual restriction in our formulation occurs when $c_{42} = 0$ and $c_{31} \neq 0$ for lossy media (or eventually when one denominator in identities (3.74a) or (3.75) becomes zero).

The method is potentially extendable to arbitrary principal axes orientation under arbitrary oblique incidence situations. This would involve solving the quartic equation (3.21) with the aid of numerical techniques like, for example, the algorithm for complex polynomials by Jenkins and Traub (1972).

CHAPTER 4

MEASUREMENT OF PRINCIPAL REFRACTIVE INDICES
OF BIREFRINGENT THIN FILMS

An arbitrary, biaxial dielectric film is ideally specified by its physical thickness d and a set of three refractive indices $\{n_1,n_2,n_3\}$, each along one of the principal axes of the material. Therefore at least four independent observations are required for its complete characterization.

It should be clear from our considerations in the previous chapter that a conveniently simple configuration involving a single-layer film, vapor-deposited at an arbitrary angle, consists of allowing the so-formed columnar axis to lie in the plane of incidence. In other words, one of the principal dielectric axes is perpendicular to that plane, and thus the s and p-polarized fields travel independently along the material.

Also for simplicity, we turn to advantage the nonuniform thickness distribution produced by oblique deposition. We carefully scan the sample position until the light beam interacts with an area of the film where the optical thickness is an integer number of quarterwaves (STEP 1). This will ultimately enable us to obtain explicit expressions for the refractive indices in terms of the experimental observables.

52

In what follows, we will be using two standard procedures in ellipsometry (Winterbottom, 1948; Azzam and Bashara, 1977; Bennett and Bennett, 1978), although in a different context from that in which the usual Fresnel equations or identities involving Airy functions are assumed to be valid (STEPS 2 and 3). These procedures have the advantage of high accuracy inherent in null measurements.

The fourth observation will utilize the Abelès technique (1949) for its extreme simplicity, although the Brewster angle will be located photoelectrically rather than visually only (Kelly and Heavens, 1959). The polarimetric extension of the technique as proposed by Hacskaylo (1964) will be incorporated to increase further the accuracy of the measurement (STEP 4).

These four experimental steps will be described in some detail in our exposition of the measurement method.

Setup Description and Operation

The arrangement of the ellipsometer is shown in Figure 4.1. The source is a single-mode HeNe laser whose output power varies by less than half of a percent over extended periods of time. It is followed by a chopper operating in tune with a lock-in amplifier at the receiver end of the apparatus. A quarterwave retarder converts the linearly polarized laser output to circularly polarized light, and is followed by a neutral density filter to ensure that the signal is processed in the linear region of the photomultiplier response whatever the orientation of the polarizer.
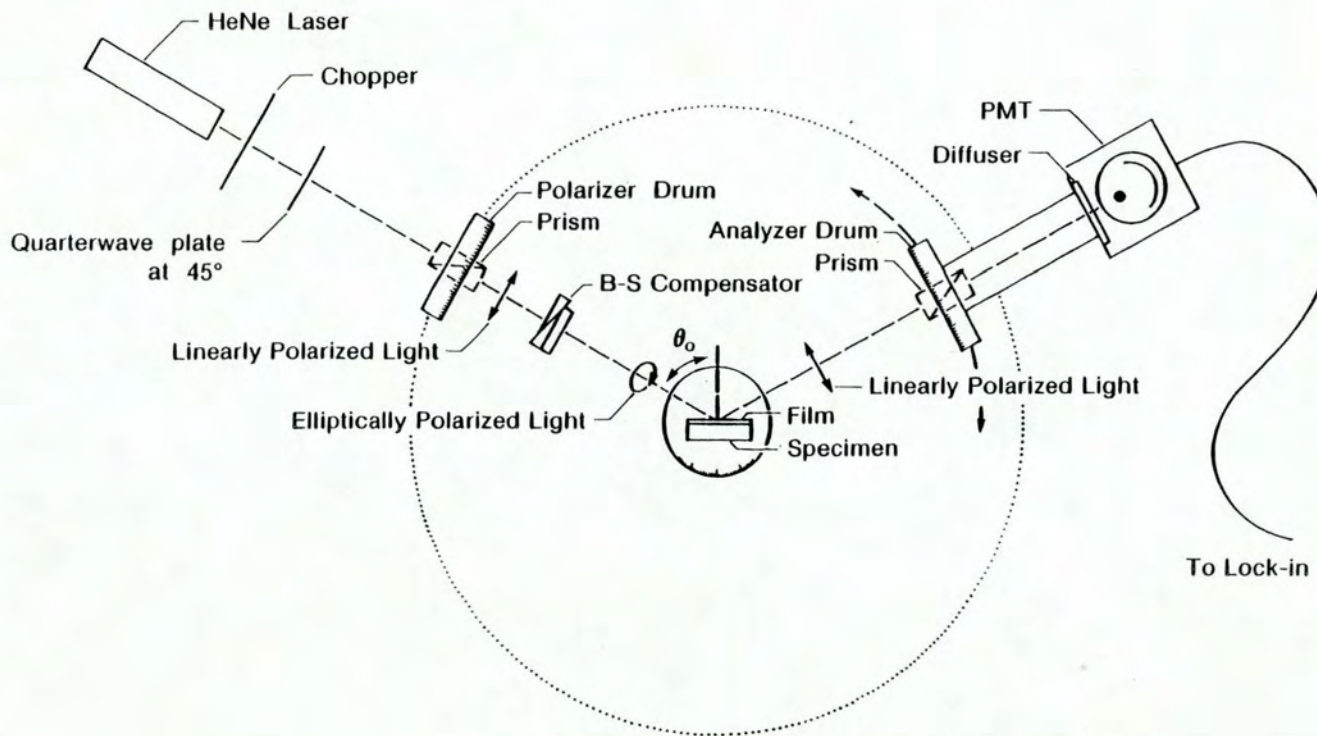
Figure 4.1. Schematic Diagram of Experimental Setup.

The polarizer and analyzer are Glan-Thompson prisms which provide extinction ratios of at most one part in 10^6. Their angular position can be read at their respective drums to an accuracy of 0.01° of arc.

A Babinet-Soleil compensator, preceding the sample, makes possible the determination of optical path differences smaller than 0.2% of the HeNe wavelength. Its calibration was performed with a high-quality quarterwave retarder at that wavelength, and later its zero position was checked by producing a dark field with the polarizer and analyzer crossed.

The sample holder is positioned on a rotating table surrounded by a horizontal master circle scaled to an accuracy of 20 sec of arc.

A critical feature of the ellipsometer (see Figure 4.2) is that the rotation of the specimen table and that of the analyzer-receiver arm must share the same central axis. At the intersection between this axis and the laser beam, centered in both arms of the instrument, lies the spot under observation. This spot is to remain ideally in the same location on the specimen as the table is rotated.

To ensure that those conditions were reasonably fulfilled, the various alignment stages of the ellipsometer were performed in accordance with the high precision procedure described by Zeidler, Kohles, and Bashara (1974) except for the following point. Since our interest was on a thin film coating rather than on a slab of material, only one surface of a glass slide was partially aluminized for the
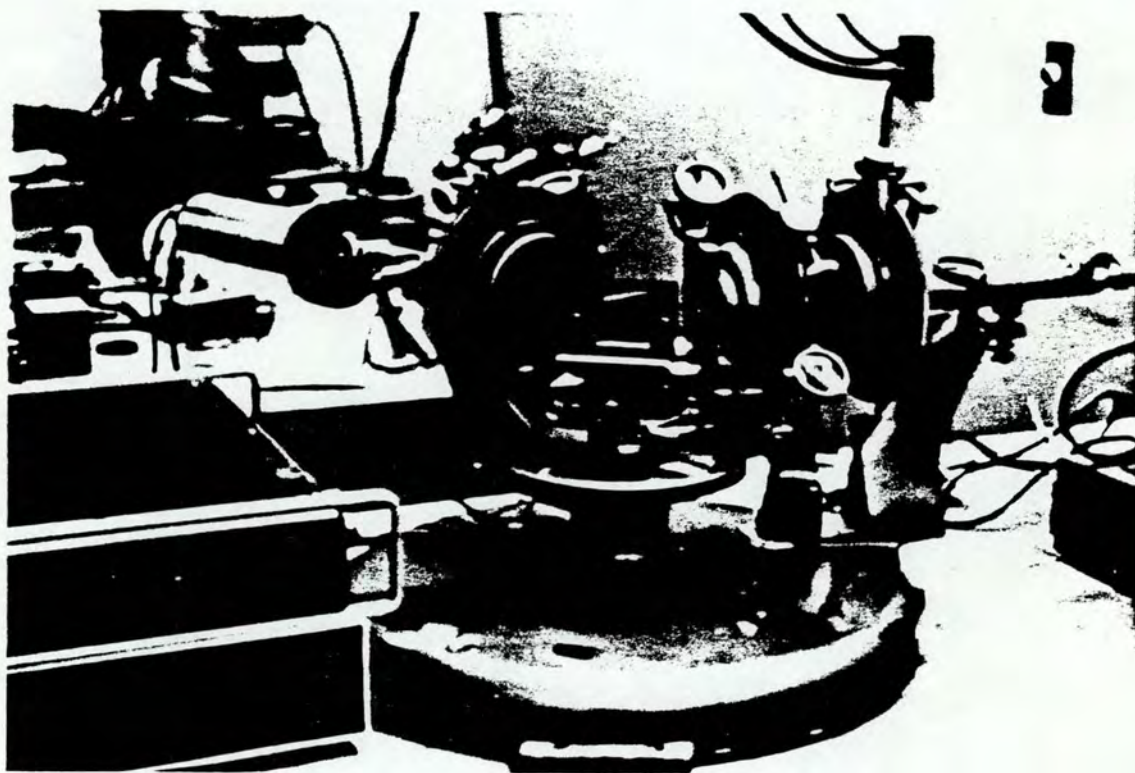
Figure 4.2. Sideview of the Ellipsometer.

alignment procedure. This ensured that the film, not the substrate, contained the central axis of rotation, and furthermore eliminated the strict requirement of parallelism between two aluminized surfaces encountered by the above authors.

A slight lateral shift of the beam over the photocathode surface occurs when a transmittance measurement is in operation at oblique angles of incidence. The consequent variation in detector sensitivity was minimized by placing a diffuser at the entrance of the photomultiplier.

Another difficulty appeared when the data showed significant dependence on touch pressure as a sample was manually scanned during the Brewster angle measurement between its coated and uncoated parts. This was circumvented by attaching a metal rod to the substrate holder (see Figure 4.3). The rod, always in contact with two fixed bolts, allowed for a smooth sliding of the holder while keeping a uniform pressure against a fixed mount. A clamp marker always ensured that the same location on the coated portion of the sample was illuminated during the iterative procedure. Reproducible results were then finally achieved.

Method

The method consists of determining $\{n_1, n_2, n_3, d\}$ from the observables $\{\Lambda_s, \Lambda_\Delta, \psi_t, \theta_B\}$, as defined in the steps below. Prior to observation, the dielectric film is obliquely deposited at a known angle ν of vapor incidence on a partly masked substrate of known refractive
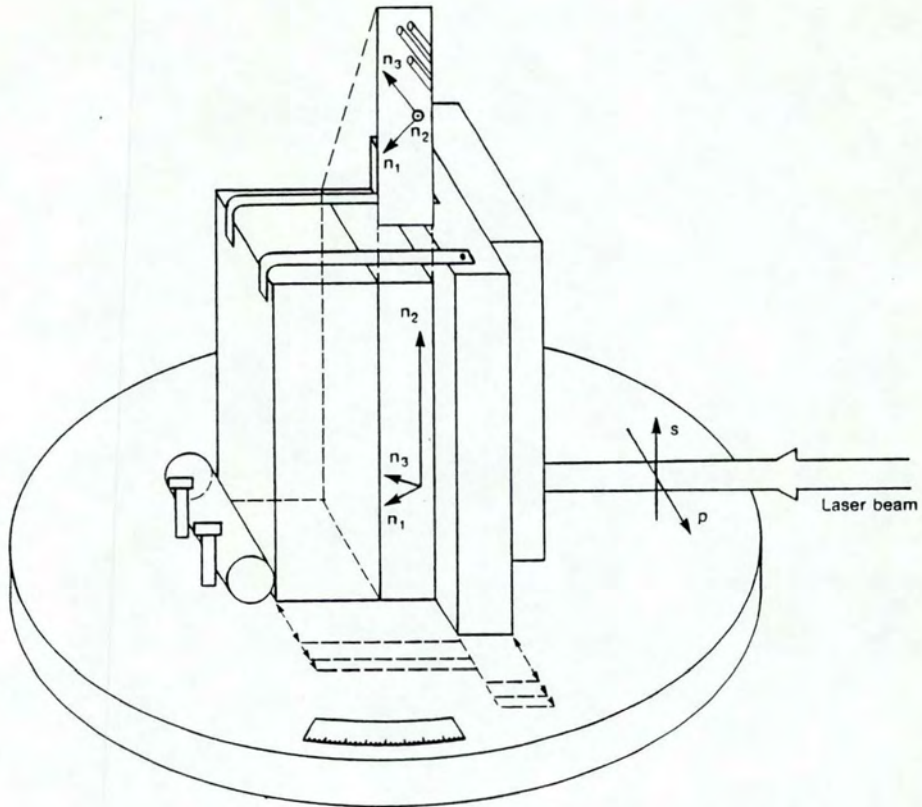
Figure 4.3.   Closeup of the Ellipsometer.

index n_g. The resultant specimen is placed in the ellipsometer holder so that the columnar axis of the film microstructure lies in the horizontal plane of incidence. This can be checked with the colored fringes of constant thickness seen by reflection under fluorescent light illumination. The fringes are perpendicular to the columnar axis.

Measurements in Transmission at Normal Incidence (Steps 1 to 3)

1. With the polarizer and analyzer transmission axes vertical, the specimen is scanned across the laser beam until a region is located where the transmittance value is an extremum. At this region Λ_s, the optical path length for s-polarized light, is given by

$$\Lambda_s \equiv n_s d = \left(\frac{\lambda_0}{4} \text{ or } \frac{\lambda_0}{2}\right) + m \frac{\lambda_0}{2} , \qquad (4.1)$$

corresponding to a minimum or a maximum in transmittance, respectively ($n_s > n_g$ assumed). A convenient way of determining the integer number m is by simply counting the number of repeated patterns of colored fringes at a film wedge whose thickness varies from zero to that of the spot under observation. When the deposition is to occur at high angles, this wedge can be formed by placing a small obstacle under the substrate, so that a portion of the latter is partially vapor-shadowed. Another alternative is to combine a FECO or a stylograph measurement of d with a rough estimate for n_s.

For steps 2 and 3, the transmission axis of the polarizer is positioned at a 45° azimuth angle. The compensator phase retardation is varied until it is equal and opposite to that produced by the specimen.

Proper analyzer orientation is then able to bring the resultant plane polarized light to nearly total extinction. In practice extinction is achieved after a very quick iteration.

2. From the compensator reading we directly obtain Λ_Δ, the optical path difference between the p and s-polarized modes,

$$\Lambda_\Delta \equiv \Delta d = (n_{po} - n_s)d \ . \tag{4.2}$$

3. The angular displacement of the analyzer transmission axis from the horizontal position, here represented by ψ_t after reduction to the first quadrant, leads to the amplitude transmittance ratio through the identity

$$\text{tg}\psi_t = \left| \frac{t_{pp}}{t_{ss}} \right| \simeq \begin{cases} \dfrac{n_{po}}{n_s} \left(\dfrac{n_s^2 + n_g}{n_{po}^2 + n_g} \right), & \text{for a quarterwave} \\[4ex] n_{po} \left(\dfrac{1 + n_g}{n_{po}^2 + n_g} \right), & \text{for a halfwave.} \end{cases} \tag{4.3}$$

The last relation is shown in the next section to be a reasonable approximation arising from the theory developed in Chapter 3.

Measurement at Oblique Incidence

4a. Preliminary. A lens is introduced right after the polarizer, set with its transmission axis horizontal, to diverge the laser beam into a bright spot containing parts of the specimen coated and uncoated regions. The angle of incidence is scanned by rotating the central table. As the reflected spot is viewed from a screen, the angular range over which a nearly uniform field can be visualized is then determined.

4b. Accurate. The observation proceeds over this angular range with the polarizer transmission axis now oriented at about 1° off the horizontal position. At each chosen angle of incidence, the specimen coated and uncoated portions are illuminated alternately while the output from the photomultiplier collecting the reflected light is examined for modulation. The analyzer orientation angle θ_M, with its origin when the transmission axis lies along the horizontal position, is varied until the modulation is zero. A set of values for $|\theta_M|$ is then plotted as a function of angle of incidence. Properly evaluated, this function is seen to converge quickly to the $\theta_M = 0$ limit corresponding to the Brewster angle (or to the absentee-layer condition, as will be explained later). An accurate result is then obtained by straightforward graphic interpolation, and the following relations among the refractive indices hold:

$$tg^2\theta_B = \frac{1-n_{po}^{-2}}{n_{po}^{-2}-(n_1 n_3)^{-2}} \text{ , for Brewster's angle,}$$

or
$$\hspace{10cm} (4.4)$$

$$\left[1 - \left(\frac{n_{po}}{n_1 n_3}\right)^2 \sin^2\theta_{abs} \right]^{1/2} n_{po}d = m\frac{\lambda_0}{2} \text{ , for absentee-layer.}$$

These two alternatives will be considered in the next section.

Data Analysis

5. From expressions (4.1) through (4.4) the physical thickness and three refractive indices of the film are obtained as follows:

$$d = \Lambda_s / n_s$$

$$n_s = n_{po}/\sigma; \quad \sigma = \frac{\Lambda_\Delta}{\Lambda_s} + 1$$

quarterwave: $n_{po} \simeq \left(\frac{\sigma^2 - \sigma\, tg\psi_t}{\sigma\, tg\psi_t - 1}\, n_g\right)^{1/2}$ (4.5)

halfwave: $n_{po} \simeq \rho \pm (\rho^2 - n_g)^{1/2}; \quad \rho = \frac{1 + n_g}{2\, tg\psi_t}$

Brewster: $(n_1 n_3)^{-2} = n_{po}^{-2} csc^2\theta_B - ctg^2\theta_B$

absentee: $(n_1 n_3)^{-2} = \frac{1 - (g/n_{po})^2}{n_{po}^2 sin^2\theta_{abs}}; \quad g = \frac{m'\lambda_0}{2d}.$

These relations are easily translated into the three principal refractive indices by use of the "equivalent (isotropic) refractive index" concept discussed in Chapter 3 leading to (3.60):

$$n_s = n_2$$

$$\frac{1}{n_{po}^2} = \frac{cos^2\phi}{n_1^2} + \frac{sin^2\phi}{n_3^2},$$ (4.6)

where ϕ defines the columnar orientation in accordance with the tangent rule (1.1)

$$tg\,\phi = \frac{1}{2}\, tg\,\nu.$$ (4.7)

Theory of the Measurement

We now apply the theory from Chapter 3 to substantiate the two arguments leading to expressions (4.3) and (4.4) left open in the description of our method.

On Relations (4.3): First-Order Approximation

Consider the particular situation for which the following conditions between the impinging light and the dielectric thin film are satisfied:

1. The s-polarization direction lies along one of the principal axes as shown in Figure 3.3(b).

2. The light beam is normally incident.

3. At least in the area where it is hit by the light beam, the film has a quarterwave optical thickness with respect to the s-polarized mode.

In the context of Chapter 3, these conditions imply that expressions (3.56) and (3.57) can be used with $S = 0$ and $\delta_s = \pi/2$, so that the propagation matrix becomes

$$
\begin{bmatrix}
\cos\delta_{po} & 0 & 0 & -\dfrac{i}{n_{po}}\sin\delta_{po} \\[2ex]
0 & 0 & -\dfrac{i}{n_s} & 0 \\[2ex]
0 & -in_s & 0 & 0 \\[2ex]
-in_{po}\sin\delta_{po} & 0 & 0 & \cos\delta_{po}
\end{bmatrix}
\tag{4.8}
$$

where now, (3.52) considered,

$$
\delta_{po} = \frac{2\pi}{\lambda_0} n_{po}d \,, \qquad \delta_s = \frac{2\pi}{\lambda_0} n_s d
$$

$$
\frac{1}{n_{po}^2} = \frac{\cos^2\phi}{n_1^2} + \frac{\sin^2\phi}{n_3^2} \,, \qquad n_s = n_2 \,.
\tag{4.9}
$$

Let

$$\Delta \equiv n_{po} - n_s, \qquad \delta \equiv \delta_{po} - \delta_s. \qquad (4.10)$$

By hypothesis $\delta_s = \pi/2$. In addition, we expect δ to be in practice sufficiently small to allow us to write in first order approximation

$$\cos\delta_{po} \simeq -\delta, \qquad \sin\delta_{po} \simeq 1. \qquad (4.11)$$

The coefficients (3.15) can then be written

$$a_p^\pm \simeq (-\delta \mp i/n_{po})n_g + in_{po} \pm \delta$$
$$a_s^\pm = b_p^\pm = 0 \qquad\qquad (4.12)$$
$$b_s^\pm \simeq \pm i\, n_g/n_s - in_s,$$

where air was taken as the incident medium.

It follows that the nontrivial amplitude reflectance coefficients from (3.17) become

$$r_{pp} = -\frac{a_p^+}{a_p^-} \simeq -\frac{(n_{po}^2-n_g) + i\delta n_{po}(n_g-1)}{(n_{po}^2-n_g) + i\delta n_{po}(n_g+1)}$$

$$ \qquad\qquad (4.13)$$

$$r_{ss} = -\frac{b_s^+}{b_s^-} \simeq -\frac{n_s^2-n_g}{n_s^2+n_g},$$

which are easily seen to coincide with their counterparts for an isotropic quarterwave layer in the $\delta = 0$ limit.

From the above, neglecting terms in δ^2,

$$\left|\frac{r_{pp}}{r_{ss}}\right| \simeq \left|\frac{n_{po}^2-n_g}{n_s^2-n_g}\right| \cdot \frac{n_s^2+n_g}{n_{po}^2+n_g}. \qquad (4.14)$$

Also from (3.17), we similarly get

$$|t_{pp}| \simeq |i(1-r_{pp})/n_{po} + \delta(1+r_{pp})| \simeq 2n_{po}/(n_{po}^2+n_g)$$

$$ \qquad\qquad (4.15)$$

$$|t_{ss}| \simeq |i(1-r_{ss})/n_s| \simeq 2n_s/(n_s^2+n_g),$$

where (4.13) and first order approximation were used.

It is interesting to note that this approximation allows conservation of energy to be valid in its exact form, i.e., the approximate amplitude coefficients expressed above, (3.18) considered, are still such that in first order $R_{pp} + T_{pp} = R_{ss} + T_{ss} = 1$.

From (4.15) we get

$$\left| \frac{t_{pp}}{t_{ss}} \right| \simeq \frac{n_{po}}{n_s} \cdot \frac{n_s^2 + n_g}{n_{po}^2 + n_g} , \tag{4.16}$$

which is the quarterwave expression in (4.3).

A similar procedure, involving a calculation even simpler than the above, leads to its halfwave counterpart in (4.3).

On Relations (4.4): Absentee Layer and Admittance Matching

Consider the configuration shown in Figure 3.3(b), the s-polarized electric field experiences a refractive index n_2 as it oscillates along the y axis, for which the propagation matrix (3.56) applies.

From the elements of this matrix, through coefficients (3.15) we determine the amplitude reflectance r_{pp} as expressed in (3.17). The corresponding reflectance can then be written

$$R_{pp} = |a_p^+/a_p^-|^2$$

$$= \frac{(\gamma_g - \gamma_0)^2 \cos^2 \delta_p{}' + (\gamma - \gamma_0 \gamma_g / \gamma)^2 \sin^2 \delta_p{}'}{(\gamma_g + \gamma_0)^2 \cos^2 \delta_p{}' + (\gamma + \gamma_0 \gamma_g / \gamma)^2 \sin^2 \delta_p{}'} , \tag{4.17}$$

where γ, $\gamma_g = n_g / \cos\theta_g$ and $\gamma_0 = n_0 / \cos\theta_0$ are the admittances of the film, substrate, and incident medium, respectively, for p-polarized light.

It is easy to see from (4.17) that R_{pp} becomes identical to the reflectance of the bare substrate,

$$R_{pp}{}^g = \left| \frac{\gamma_g - \gamma_0}{\gamma_g + \gamma_0} \right|^2 , \tag{4.18}$$

when one out of two conditions is satisfied.

The first occurs when $\delta_p{}'$ is a multiple of π or, from (3.57), with the aid of (3.46), (3.52), and (3.59), at $\theta_0 = \theta_{abs}$:

$$\left[1 - \frac{n_0 n_{po}}{n_1 n_3}^2 \sin^2\theta_{abs} \right]^{1/2} n_{po} d = m' \frac{\lambda_0}{2} ; \quad m' = 1,2,\ldots \tag{4.19}$$

With regard to traditional thin film theory, noting that when this identity holds the effective optical path traversed by p-polarized light is an integer number of halfwaves, we refer to (4.19) as the "absentee-layer" condition. It becomes the first of expressions (4.4) for air as the incident medium.

The second condition occurs when $\gamma = \pm\gamma_0$, to which we refer as "admittance-matching." With (3.57), (3.46), and (3.59), this implies that at $\theta = \theta_B$

$$\frac{1}{\gamma^2} = \frac{1}{n_{po}^2} - \frac{n_0 \sin^2\theta_M}{n_1{}^2 n_3{}^2} = \frac{\cos^2\theta_B}{n_0{}^2} , \tag{4.20}$$

which after a straightforward manipulation leads to

$$tg^2\theta_B = \frac{n_0{}^{-2} - n_{po}{}^{-2}}{n_{po}{}^{-2} - n_0{}^2 (n_1 n_3)^{-2}} . \tag{4.21}$$

For $n_0 = 1$ we obtain the second of expressions (4.4).

Discussion

In the isotropic limit, $n_{po} = n_1 = n_3$, (4.21) takes the form

$$tg\theta_B = \pm \frac{n_3}{n_0} , \tag{4.22}$$

from which it becomes evident that Brewster's law is a particular consequence of the admittance-matching condition.

It is interesting to note that, even under the presence of a strongly asymmetric microstructure, (4.21) still allows for the existance of a pair of angles θ_B symmetrically located with respect to the surface normal. This is consistent with the periodicity of the T_{pp} versus θ_0 curve shown in Chapter 2.

Why does Brewster's law become invalid for anisotropic media?

A way of looking at this question is as follows. In the isotropic case, Brewster's law is derivable from Snell's law and by taking the refracted ray in a direction orthogonal to that of the reflected ray (virtual, if light is p-polarized only). This last ingredient is physically attributed to the well known radiation pattern that results from dipole oscillations along the refracted electric field E_p^+ direction. In the anisotropic case, however, the refracted ray is perpendicular to the displacement vector D_p^+, and <u>not</u> to E_p^+, as shown in Figure 4.4. Therefore, for the dipole oscillations to occur perpendicularly to the reflected ray direction, the refracted ray must <u>not</u> be orthogonal to that direction and Brewster's law does not apply (although we keep calling θ_B by "Brewster's angle" for convenience).

Very significantly, that is still the case for films deposited at normal vapor incidence. Here $\phi = 0$, from (3.52) $n_{po} = n_1$, and thus (4.21) becomes
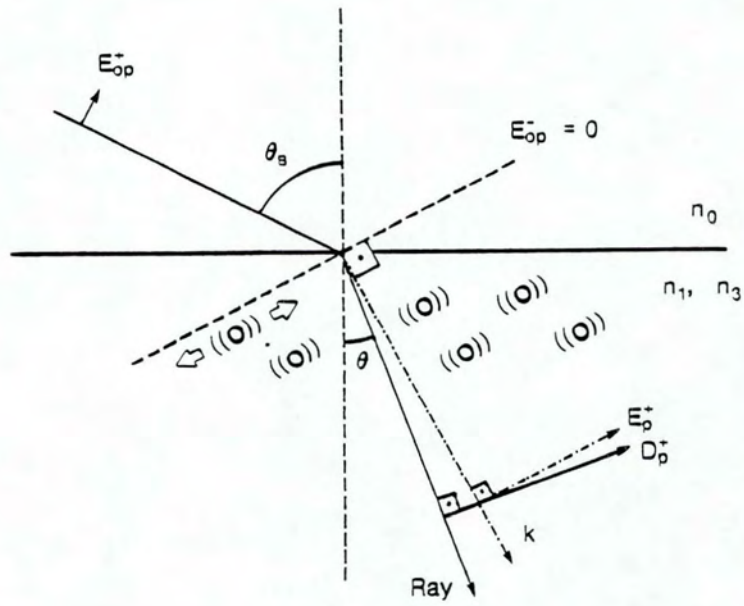
Figure 4.4. Brewster Reflection for Anisotropic Media.

$$tg^2\theta_B \ = \ \left(\frac{n_3}{n_0}\right)^2 \ \cdot \ \frac{n_1^2 - n_0^2}{n_3^2 - n_0^2} \ . \tag{4.23}$$

This result alone is good reason for careful interpretation of thin film measurements at the Brewster angle.

For $\phi = 90°$ we reobtain (4.23) with the permutation $n_1 \leftrightarrow n_3$.

These two particular cases were reported by Malleman and Suhner (1944), and their results are in perfect agreement with ours.

Example

For illustration we now apply our method to the determination of the principal refractive indices of a zirconium oxide film deposited at 65° onto a glass substrate (sample ZO 0808-65), corresponding to a columnar orientation angle $\phi \simeq 46.997°$ in accordance with (4.7).

Prior to deposition, the substrate is masked in two regions, as shown in Figure 4.5. The horizontal mask allows for the measurement at oblique incidence, step 4 in the exposition of the method, involving the alternate illumination of the specimen's coated and uncoated portions. The vertical mask is elongated perpendicularly to the loci of constant thickness. It produces a sharp step which, properly aluminized, will later enable the determination of the physical thickness of the film through a FECO observation at, or in the neighborhood of, the locus of constant thickness where the ellipsometer measurements are carried.

These measurements start with the determination of n_g, the refractive index of the glass substrate. Here we utilize the Abelès technique with photoelectric detection and the Hacskaylo polarimetric
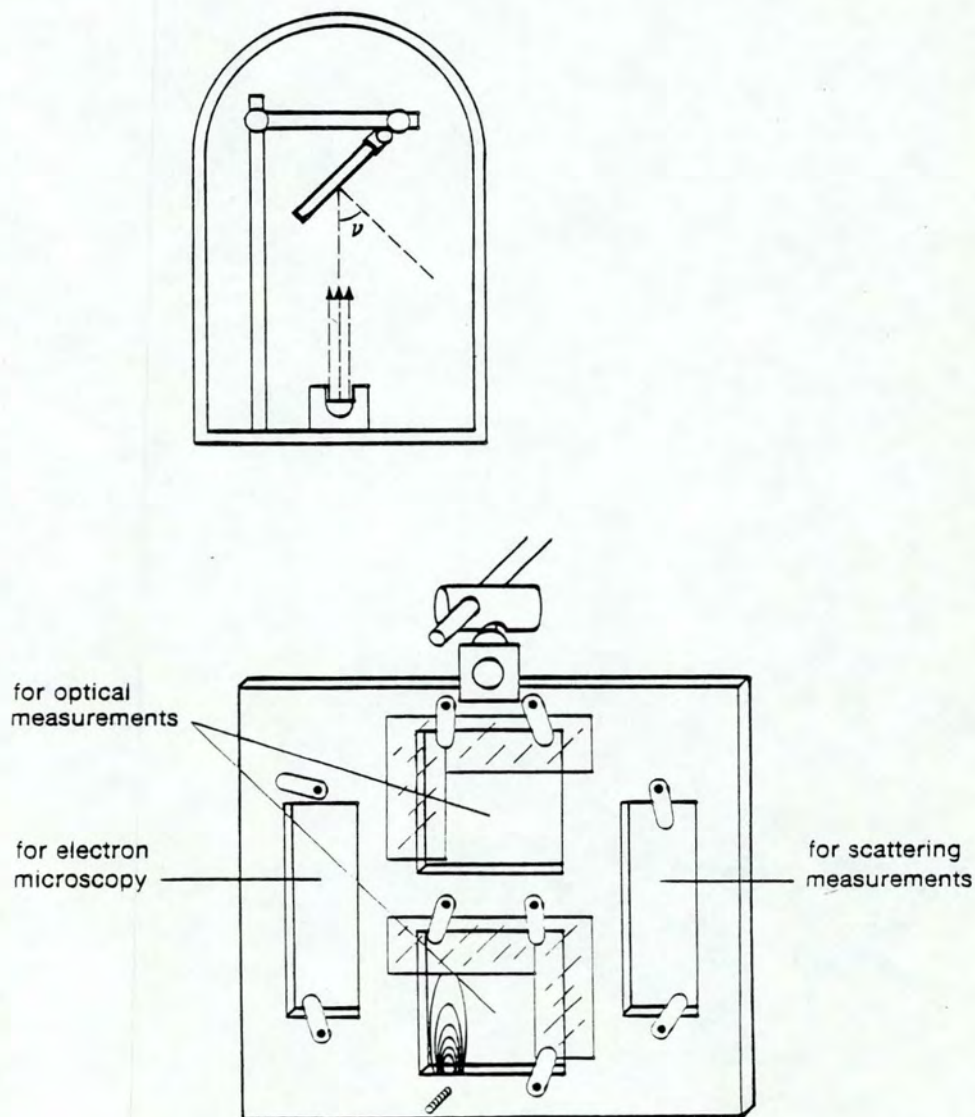
Figure 4.5.   Deposition Geometry and Sample Holder.

At the bottom, the colored fringes seen under fluorescent light on the wedge produced by the partial vapor-shadow of a bolt are represented.

extension, as described in step 4b, with the only difference that we now look for a null rather than a matching reflectance. Figure 4.6 shows the outcome of this observation, followed by a close-up in Figure 4.7. The resulting refractive index value is

$$n_g = 1.5131 \ (\pm 0.0005). \tag{4.24}$$

Our error estimate is slightly more conservative than that reported by Hacskaylo (1964) because in our understanding the error contribution from the graphical interpolation process should be taken into account.

We now proceed with the characterization of the specimen through the steps outlined in the exposition of the method. The resulting data are as follows:

$$\Lambda_S = 3/2 \ \lambda_0$$

$$\Lambda_\Delta = 0.05783 \ (\pm 0.00010) \ \lambda_0 \tag{4.25}$$

$$\psi_t = 44.460° \ (\pm 0.005°)$$

$$\theta_B = 58°31'12'' \ (\pm 30'') = 58.520° \ (\pm 0.008°).$$

The graphical determination of Brewster's angle is shown in Figure 4.8.

Analysis of these data, with $\phi = 46.997°$, $h_g = 1.5131$, and $h_0 = 1.0000$, leads to the four characterization parameters

$$n_1 = 1.502 \ (\pm 0.009)$$

$$n_2 = 1.575 \ (\pm 0.001) \tag{4.26}$$

$$n_3 = 1.788 \ (\pm 0.015)$$

$$d = 0.952 \ (\pm 0.001) \ \lambda_0 \approx 602.5 \ (\pm 0.6) \ nm,$$

while the "equivalent refractive index" at normal incidence for p-polarized light (see discussion following (3.59))
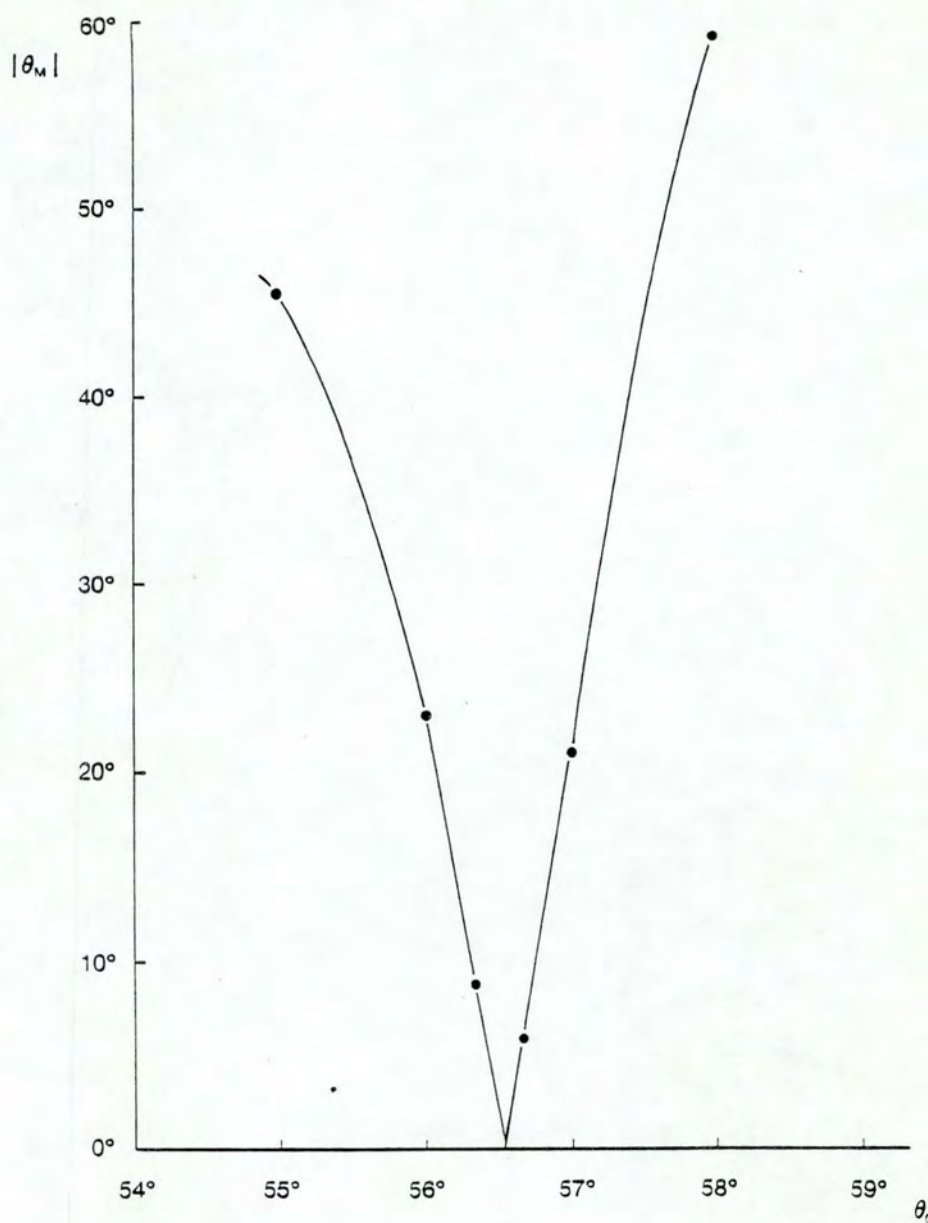
Figure 4.6. Experimental Data for the Determination of the Refractive Index of a 2 in. x 2 in. Glass Slide.

θ_n is the azimuth angle of the analyzer transmission axis, with origin at the horizontal position, for which the reflectance is extinguished at a given angle of incidence θ_0.
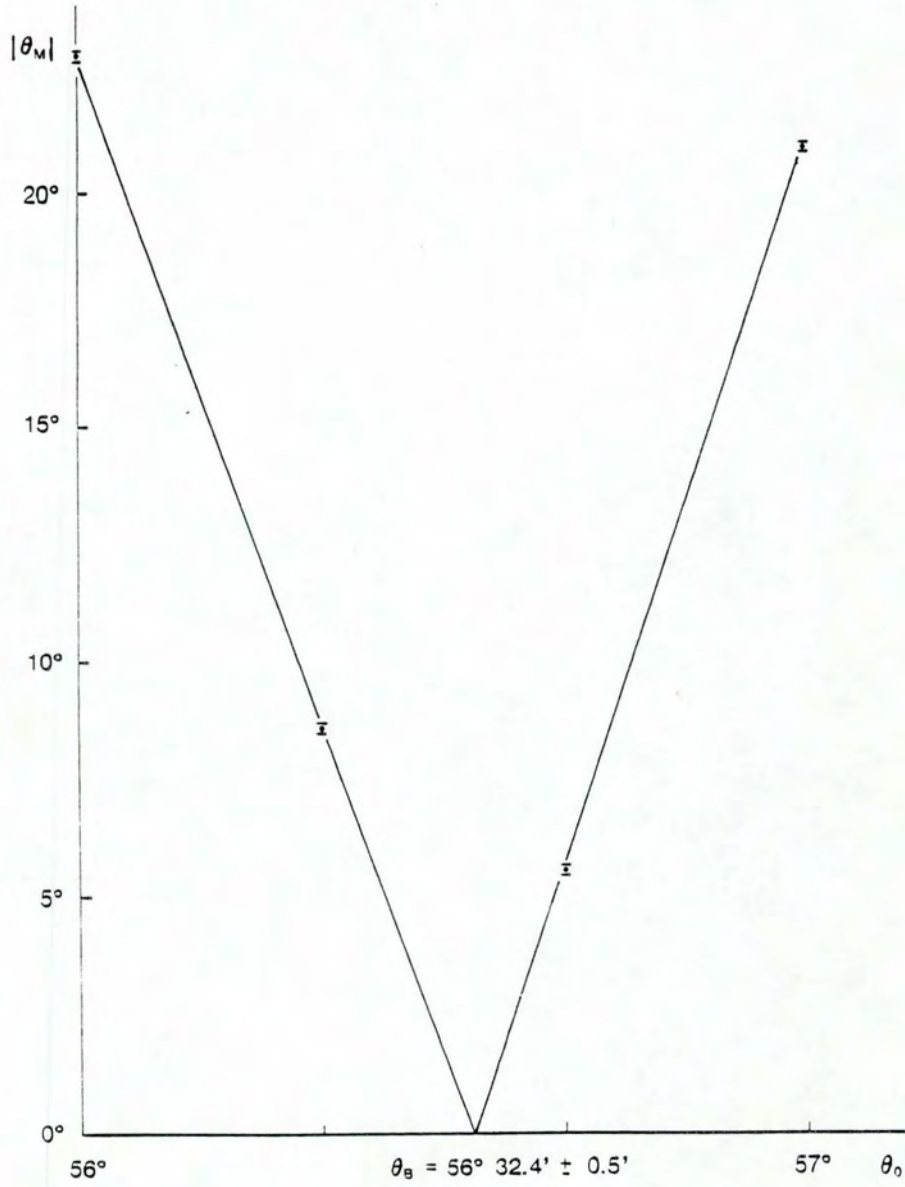
Figure 4.7.   Closeup of Figure 4.6.
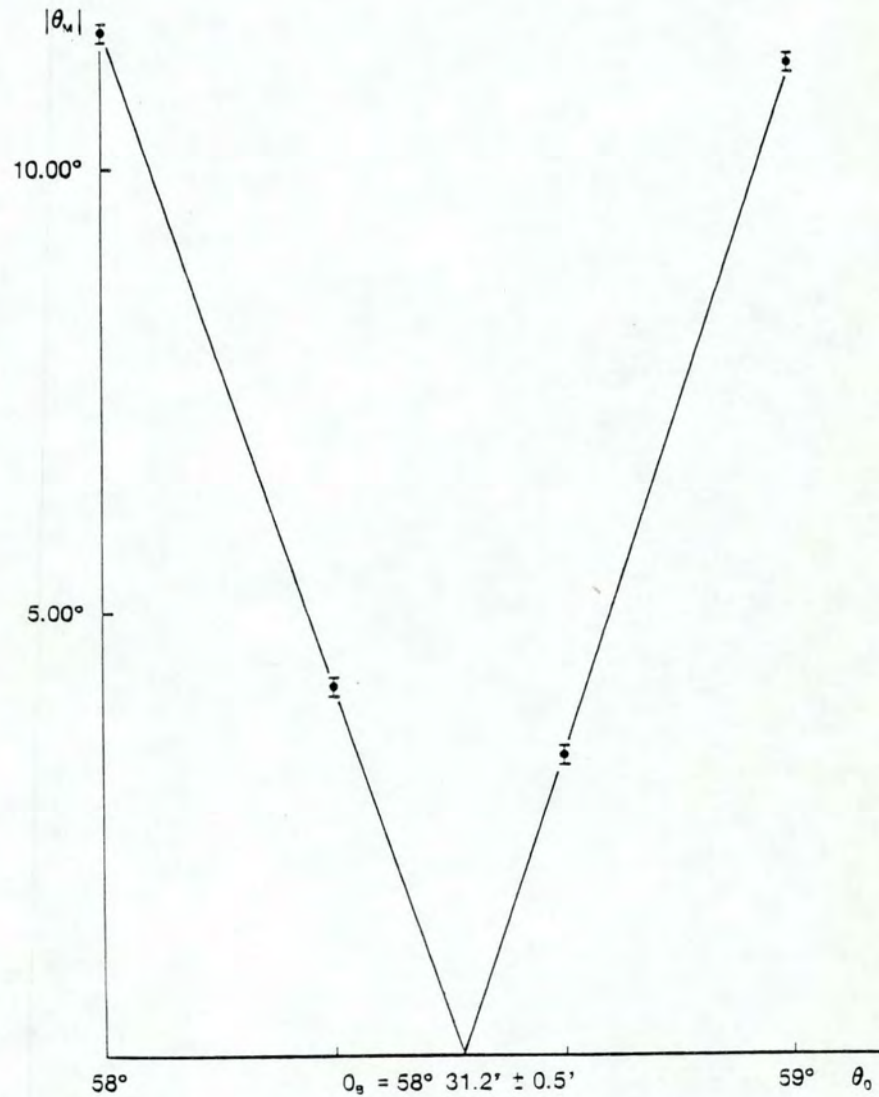
Figure 4.8.   Experimental Data for the Determination of Brewster's Angle
for a Zirconium Oxide Sample.

θ_M is the azimuth angle of the analyzer transmission axis,
with the origin at the horizontal position, for which the
reflectances of the coated and uncoated parts of the speci-
men are matched at a given angle of incidence θ_0.

$$n_{po} = 1.636 \ (\pm 0.001), \hspace{4cm} (4.27)$$

so that the effective amount of birefringence at normal incidence results as

$$n_{po} - n_s = 0.061 \ (\pm 0.002). \hspace{3cm} (4.28)$$

The numbers indicated in parentheses are rough error estimates originated in the measurement process and magnified as they propagated through the calculation.

Interpretation

Do parameters (4.26) make sense? Given the literature omission on quantitative information about form birefringence in thin films, we now resort to some other evidence that is available to us. The considerations that follow are not to be taken rigorously, but rather as constituting a plausibility argument.

We performed a FECO measurement at, or in the neighborhood of, the locus of constant thickness where the ellipsometer measurements were made. The observed physical thickness is of the order of 530 nm, which indicates that the value for d obtained in (4.26) is not unreasonable. Their difference may be partly due to the strong nonuniformity in film thickness we have observed, which makes the FECO measurement extremely dependent on position. It may also be due to dissimilar phase changes by reflection on the aluminized film and (much smoother) aluminized glass surfaces.

As to the refractive indices, we now consider a simple columnar structure model in connection with the thin film growth simulation

performed by Marten Sikkens. His two-dimensional results for 60° and normal incidence are shown in Figure 4.9.

In a three-dimensional situation we can imagine those pictures, in that order, as representing the projected film microstructure in a plane parallel and perpendicular to the plane defined by the vapor beam and the substrate normal.

The perpendicular plane clearly presents a larger amount of solid material per unit area. Therefore, if we are to model the three-dimensional microstructure as a sequence of identical columns, each column must have an elliptical cross section elongated in the perpendicular direction. In fact, experimental evidence for this elongation was found by Leamy, Gilmer, and Dirks (1980) through a transmission electron microscopy observation with the electron beam parallel to the columnar orientation.

Howe elongated should it be in our case? A crude estimate can be made by counting the number of solid disks along a typical horizontal section AB in Figures 4.9(a) and (b), and taking their ratio. The ellipticity that follows is

$$b/a = 58/40 = 1.45. \qquad (4.29)$$

The microstructure of the film can then be modeled as consisting of solid rods with an elliptical cross section, infinite length, and refractive index n, randomly distributed in an air matrix. A simple adaptation of Wiener's expression (Bragg and Pippard, 1953) leads to the effective refractive indices along the principal axes
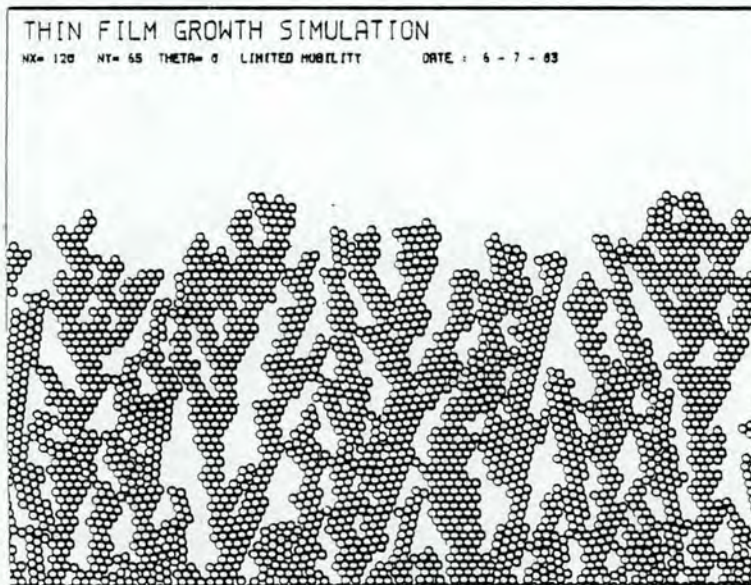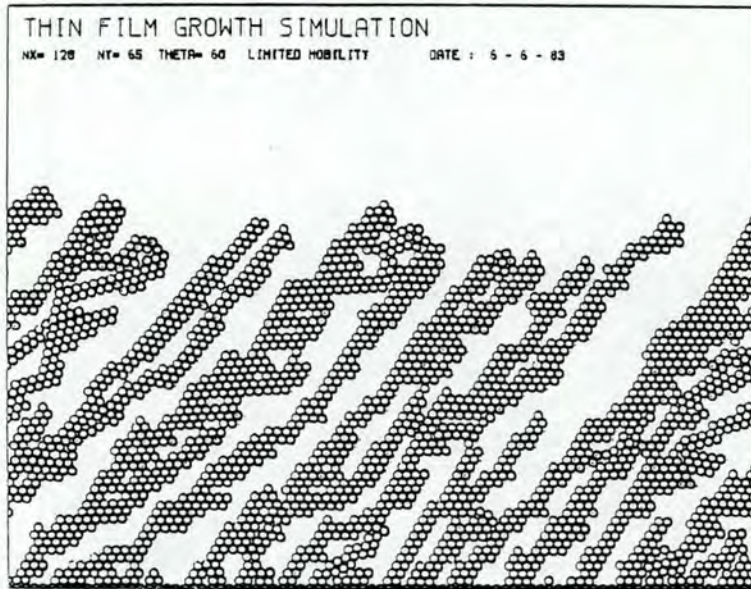
Figure 4.9. Film Structure Resulting from the Simulated Deposition
Process at (a) v = 60° and (b) v = 0°.

Each impinging molecule, represented by a hard disk, was
allowed to "move" randomly until contact with other two
was reached (by Marten Sikkens).

$$n_j^2 = 1 + \frac{p(n^2-1)}{1 + (1-p)(n^2-1)L_j} \; ; \qquad j = 1,2,3 \; , \tag{4.30}$$

where p is the packing density, or fractional volume of solid material in the medium, and the depolarization factors are

$$L_1 = \frac{b}{a+b} \; , \qquad L_2 = \frac{a}{a+b} \; , \qquad L_3 = 0. \tag{4.31}$$

From the CRC Handbook (Weast, 1980, p. B-166) we know that zirconium dioxide in bulk form has an average refractive index of 2.17. We use this value for n.

Now we set the packing density value so that $n_3 = 1.80$, say, and from (4.30) and (4.31) get p = 0.60. Identity (4.30) is not strictly valid for this packing density value, but can reasonably be used for our rough estimation.

The above considerations result in the following set of principal refractive indices:

$$\begin{aligned} n_1 &= 1.48 \\ n_2 &= 1.55 \\ n_3 &= 1.80, \end{aligned} \tag{4.32}$$

which are less than 2% off their corresponding measured values in (4.26). This seems to indicate that our measurement does indeed make sense, as well as in the simple model we have used.

CHAPTER 5

OPTICAL PROPERTIES: THEORY AND EXPERIMENT

Our task here is to collect experimental evidence on the optical properties of an anisotropic thin film and compare it with the predictions of the theory developed in Chapter 3. To do this quantitatively, we need the optical constants and physical thicknesses that specify the film under study. That was our concern in Chapter 4. In practice we connect these characterization parameters to optical properties through a computer program developed directly from the theory. We call it the "anisotropic thin film (ANTF) program," and begin with a brief description of its main features.

The ANTF Program

The program applies for CASES 0, 1, and 2 of homogeneous, biaxial thin films (see Chapter 3). Absorption is allowed for all media but the incident. Although it was devised with the columnar model in mind, it is valid as well for any other source of optical anisotropy, as long as principal axes are still definable. From a user's point of view, the program can be specified as follows:

Input:

    Refractive index for the incident medium and optical constants for the substrate.

    Initial and final values of variable, and variable interval

(variable = wavelength, angle of incidence, or azimuth angle).

Values of the two fixed variables.

For each layer: principal optical constants, two angles defining the columnar orientation and physical thickness.

Vertical scaling defined by minimum and maximum ordinate values.

Output:

Required vapor angle of incidence for each layer.

Reflectance, reflectance phase and transmittance for s, p, and crossed polarizations at chosen angle of incidence, wavelength, or azimuth angle ranges.

The overall structure of the program is shown in Figure 5.1. MAIN PROGRAM is a direct consequence of our theory without any specific particularization. SIMLAR performs a similarity transformation that allows for rotations of the principal axes (see Appendix B). MATMUL provides the product of any two square matrices (3x3 for SIMLAR and 4x4 for MAIN PROGRAM). BIQUAD particularizes the problem to situations for which the secular equation becomes biquadratic or for which the s and p-modes can be treated separately, and addresses the program to CASE1 or CASE2 after testing for a few mathematical restrictions. VECMUL performs the "direct vector product" operation, as defined in Chapter 3. PLOT plots.

The program was initially tested in the isotropic limit through a few multilayer design problems by comparing its results to those of
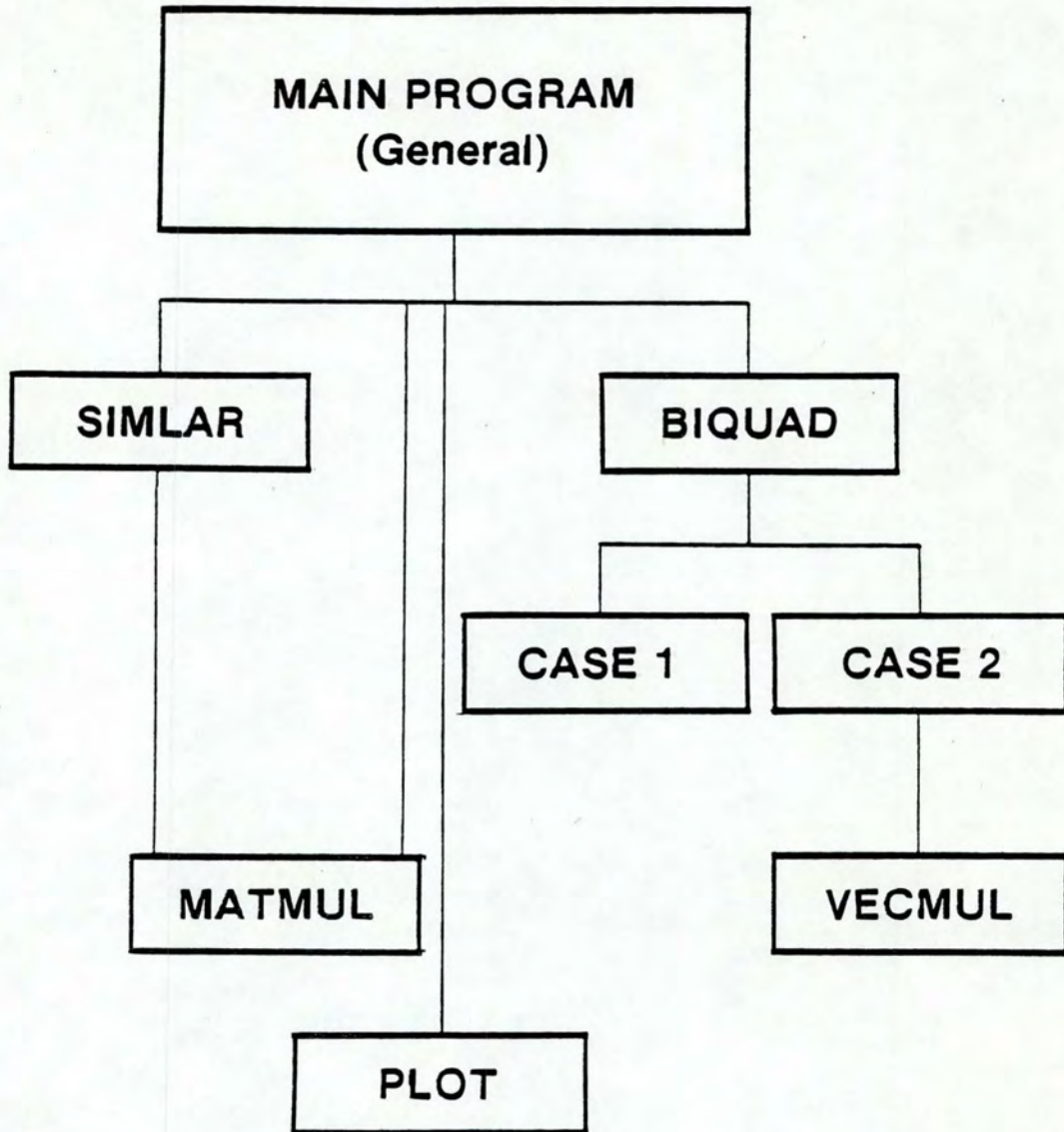
Figure 5.1. Overall Structure of the ANTF Program.

Prof. Angus Macleod's OPTF. The agreement was complete, at least up to the six-decimal digits provided by the output of the two programs, in all cases considered.

The decisive tests for the ANTF program, however, are in its main purpose of dealing with anisotropic films. In the process of allowing us to place the consequences of the theory side by side with the experimental data, which we describe next, one should bear in mind that the validity of the program itself is also under question.

Experimental Evidence

We start from the measurements of transmittance versus angle of incidence ($T \times \theta_0$), which are not intended for the direct observation of optical anisotropy, but rather as a preparation for the transmittance measurements with variation of azimuth angle ($T \times \alpha$) in which the effect is much more pronounced. All those were performed with the setup and the zirconium oxide sample considered in the previous chapter. Later we present spectral data ($T \times \lambda_0$) obtained from a Cary 14 spectrophotometer for a dielectric multilayer system.

$T \times \theta_0$

The results of the measurement are shown in Figure 5.2. The experimental procedure is as follows. The polarizer and analyzer transmission axes are rotated to the chosen polarization mode, horizontal for p, and the gain of the lock-in amplifier (and/or that of the voltage across the photomultiplier) is set for a digital reading of 100.0. The
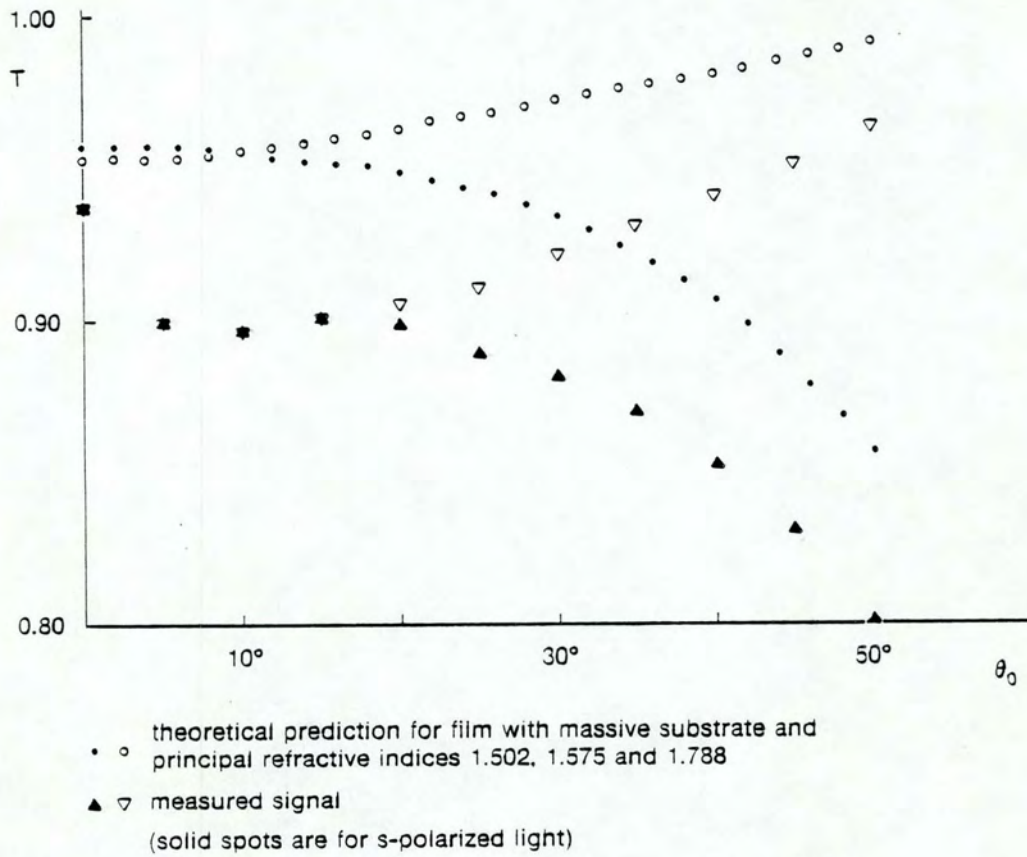
Figure 5.2. Noncrossed Transmittances versus Angle of Incidence (Zirconium Oxide Sample).

sample is then properly attached to the holder for the starting, normal incidence data point.

The positioning of the Z00808-65 sample is critical because we try to reproduce the conditions present during its characterization (see Chapter 4) as accurately as possible. This also means that the whole set of observations for an individual specimen should be performed in the period of a few days, since films deposited at high angles of vapor incidence are very porous and thus extremely susceptible to water adsorption from the atmosphere.

The laser fluctuations, up to 0.5% in intensity, are another important source of error. Their influence is minimized, as the specimen table is rotated for each data point in Figure 5.2, by resetting the 100.0 reading in the absence of the sample whenever a signal discontinuity by more than 0.3% is noticed under otherwise unchanged conditions.

Also present in Figure 5.2 is the prediction from the theory, which assumes a massive substrate medium. If it is to be compared with the measured results, then the substrate back-reflectance must be taken into account (the glass substrate absorption is negligible for our purposes).

A rigorous treatment would require an integration of the interference fringe intensities, originated from the near-parallel surfaces of the substrate, over the detector aperture for each angle of incidence. Another alternative is to pick a similar glass slide, subject it to the same measurement conditions as that of the sample, and from

its optical behavior establish the amount of back-reflectance from the glass-air interface.

We started from this second alternative without much success because, as different portions of the slide were illuminated at low angles of incidence, we observed dramatic fluctuations in transmittance that precluded determining a typical value. Such fluctuations are clearly connected to those involving relative orientation between the two surfaces of the slide, as well as to irregularities at each surface.

We then decided to approach the problem with the simplifying assumption that the sum of the individual fringe contributions to the detector intensity signal, each resulting from a mostly coherent effect, would ultimately come close to the outcome of an incoherent formulation as many fringes were taken into account.

Multiple-beam internal reflections in a nonabsorbing slab of material, treated as incoherent contributions to its total transmittance T, lead to the well known identity

$$\frac{1}{T} = \frac{1}{T_f} + \frac{1}{T_g} - 1, \tag{5.1}$$

where T_f and T_g are the intensity transmittances of the two opposite surfaces of the material.

In our case, $T_g(\theta_0)$, referring to the glass-air interface, is determined from

$$T_g = 1 - \left| \frac{\gamma_g - \gamma_a}{\gamma_g + \gamma_a} \right|^2, \tag{5.2}$$

where $\gamma_g(\theta)$ and $\gamma_a(\theta_0)$ are the admittances of glass and air,

respectively, at a given angle of incidence θ_0 (to which θ is connected through Snell's law) and at a given polarization mode (see (3.35)).

Several values of T_g are shown in the first column of Table 5.1 (a) and (b), for which the refractive index of the glass substrate was taken as $n_g = 1.5131$ in accordance with our previous measurement (see Figure 4.6). Those values and the data shown in Figure 5.2 for T_f, the theoretical film transmittance, are used in (5.1) to produce the predicted transmittance curves with back-reflectance correction in Figure 5.3.

Also shown in Table 5.1 is the correction for the residual detector nonlinearity noticed after the experiment was completed. This correction was established by exact reproduction of the range of setup arrangements and settings utilized during all stages of the experiment, and by detailed observation of the signal when the laser beam was subjected to different amounts of attenuation under those conditions. The input to the detector was taken as a function of the corresponding signal in the quadratic form

$$I(S) = aS + bS^2. \tag{5.3}$$

Constants a and b were determined by taking a common origin and a common reference maximum, i.e., $I(0) = 0$ and $I(100) = 100$, combined with the observation of an arbitrary signal for the conditions of minimum and maximum nonlinearity. A signal reading of 91.70 corresponded to a relative input of 91.22 and 90.55 (checked in linear, very low-intensity conditions), respectively, leading to the values:

Table 5.1. Values of T_{pp} and T_{ss} for Various Angles of Incidence

θ_0 (Deg)	T_{pp} (%)[+]					T_{ss} (%)[+]				
	T_g(TH)	T(BR)	S	I_1(NL)	I_2(NL)	T_g(TH)	T(BR)	S	I_1(NL)	I_2(NL)
0	95.831	91.512	93.7	92.808	93.329	95.831	91.914	93.8	92.921	93.435
5	95.873	91.624	89.9	88.528	89.330	95.789	91.833	90.0	88.640	89.435
10	96.000	91.942	89.8	88.416	89.225	96.660	91.591	89.7	88.304	89.120
15	96.211	92.499	90.2	88.864	89.645	95.435	91.157	90.2	88.864	89.645
20	96.508	93.284	90.5	89.201	89.960	95.101	90.486	89.8	88.416	89.225
25	96.891	93.899	91.0	89.762	90.486	94.632	89.514	88.9	87.409	88.281
30	97.356	94.763	92.0	90.888	91.538	93.997	88.174	88.2	86.627	87.547
35	97.895	95.693	93.0	92.016	92.591	93.146	85.954	87.1	85.402	86.395
40	98.488	96.694	94.1	93.261	93.752	92.010	83.966	85.2	83.295	84.409
45	99.095	97.768	95.2	94.509	94.913	90.489	80.472	83.2	81.088	82.323
50	99.639	98.849	96.3	95.762	96.076	88.445	77.058	80.1	77.691	79.100

[+]Explanation of symbols:

θ_0 Angle of incidence

T_g(TH)   Glass transmittance from theoretical calculations

BR   Substrate back-reflectance considered (theory)

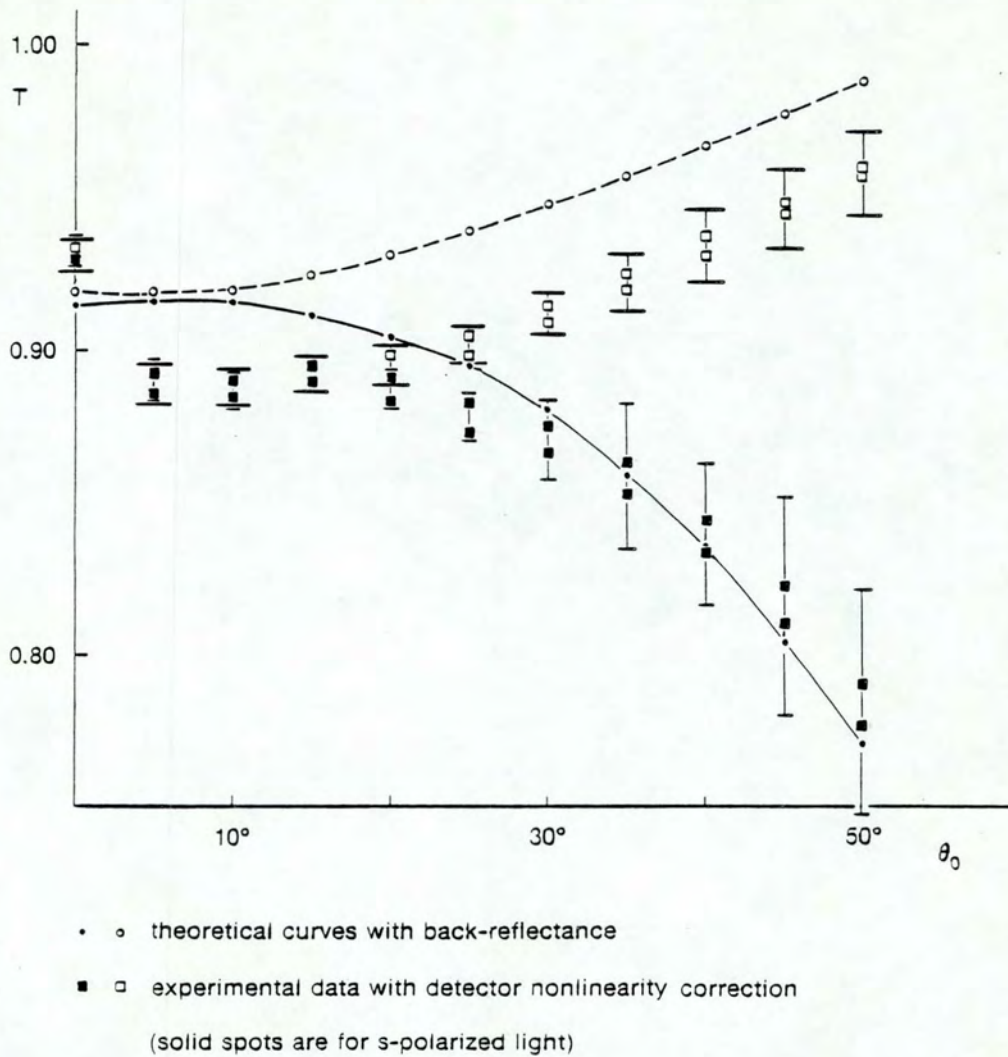S   Measured signal

NL   Detector nonlinearity corrected

Figure 5.3. Corrected Noncrossed Transmittances versus Angle of
Incidence (Zirconium Oxide Sample).

$$I_2 \text{ (min. NL):} \quad a = 9.372 \times 10^{-1}, \quad b = 6.276 \times 10^{-4}$$

$$I_1 \text{ (max. NL):} \quad a = 8.489 \times 10^{-1}, \quad b = 1.511 \times 10^{-3},$$

utilized for obtaining the last two columns in Table 5.1 (a) and (b).

The experimental data shown in Figure 5.3 are the result of the above correction applied to the measured signal in Figure 5.2. Note that the general shapes of the experimental and theoretical curves for p-polarized light, as well as those for s-polarization up to around 30°, are in reasonable agreement.

We could easily select extinction coefficients that would optimize the fitting between corresponding curves but, instead, decided to keep the comparison free from adjustable parameters, bearing in mind that the differences may be partly caused by inhomogeneity or scattering losses. The experimental results for s-polarization over 30° are relatively poor in information content due to increasing transmitted beam walkoff and elongation of the illuminated spot with increasing angle of incidence. In addition, the pronounced steepness of the curve at that region magnifies small deviations in alignment and other imperfections of the ellipsometer. Nevertheless, those results are presented here for completeness.

One problem remains in the comparison between theory and experiment: why is there such a discrepancy at normal incidence?

We got an answer to this question only after we carefully looked at the intensity-structure of the beam reflected by the sample as its supporting table was slowly rotated toward low angles of incidence.

Following the beam in this manner, we readily noticed that the number of fringes gradually decreased until essentially only one was observed at near-normal incidence. In other words, at that angle and at the particular region of the sample we picked for our measurements, the substrate happens to partially behave like a Fabry-Perot cavity!

For that reason, the normal-incidence experiments we describe next must have their results corrected accordingly.

T x α

The transmittance versus azimuth angle curves are shown in Figures 5.4 and 5.5. The substrate interference effect we have just discussed is taken into account through Table 5.2 when we multiply the measured signal by the ratio between the measured transmittances at 5° and at normal incidence shown in Figure 5.2. This simple correction is supported by the fact that the transmittance curves are expected to be nearly flat between zero and 15°.

In Figure 5.4, it is interesting to note that the theory predicts an asymmetry in the transmittance curve that could hardly be noticed during the experiment (or even later with the nonlinear correction). The asymmetry is due to the variation of the effective refractive index when the columnar orientation changes with respect to the normally incident electric field. The magnitude of this variation is well within the experimental error.

Looking at the good agreement in general shape between the theoretical and experimental curves, one may be tempted to use
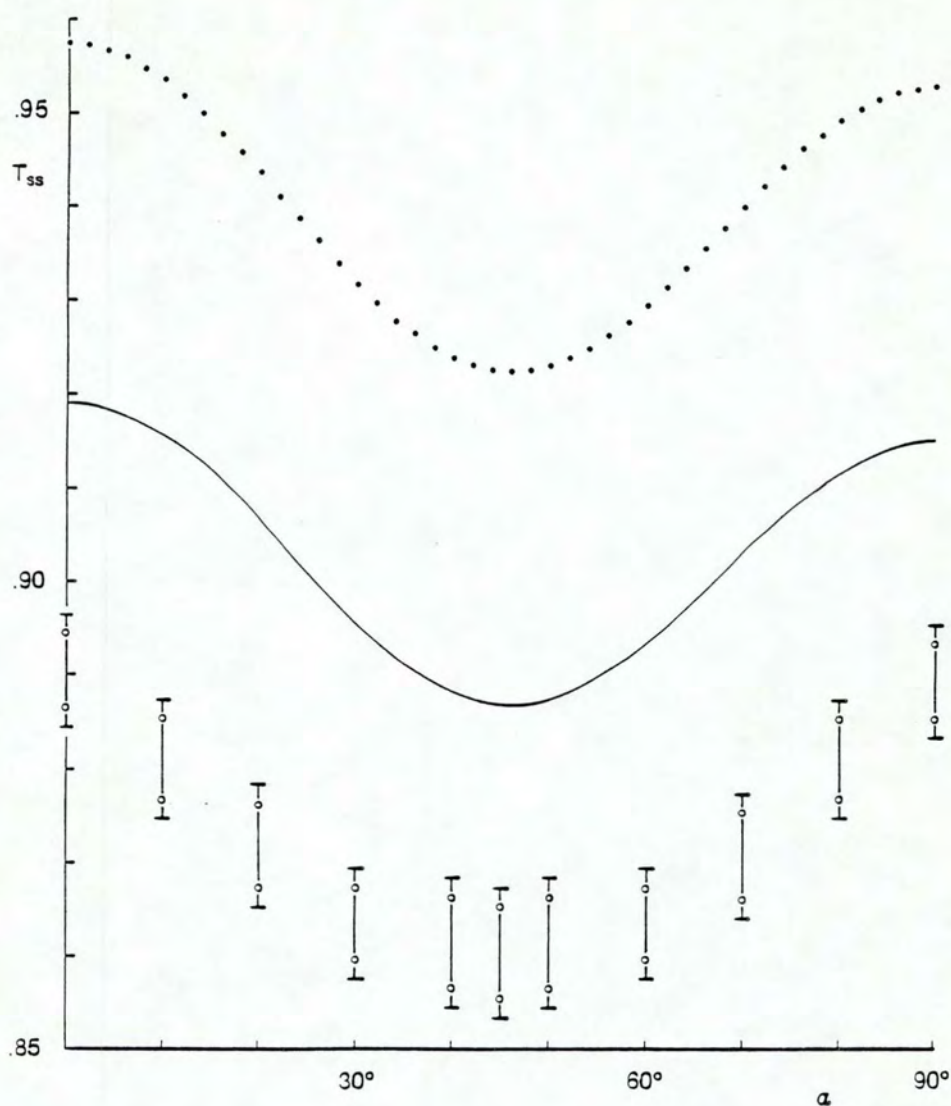
Figure 5.4. Noncrossed s-Polarization Transmittance versus Azimuth
Angle.

The corresponding T_{pp} curves can be visualized by the
mirror image of this figure. Columnar orientation is
horizontal at the origin (zirconium oxide sample).

Figure 5.5. Crossed Transmittances versus Azimuth Angle.

Sets of principal refractive indices assumed for the theoretical curves are, in descending order: [1.493, 1.574, 1.803], [1.502, 1.575, 1.788], and [1.511, 1.576, 1.773] (zirconium oxide sample).

Table 5.2. Values of T_{sp} and T_{ss} for Various Angles of Incidence

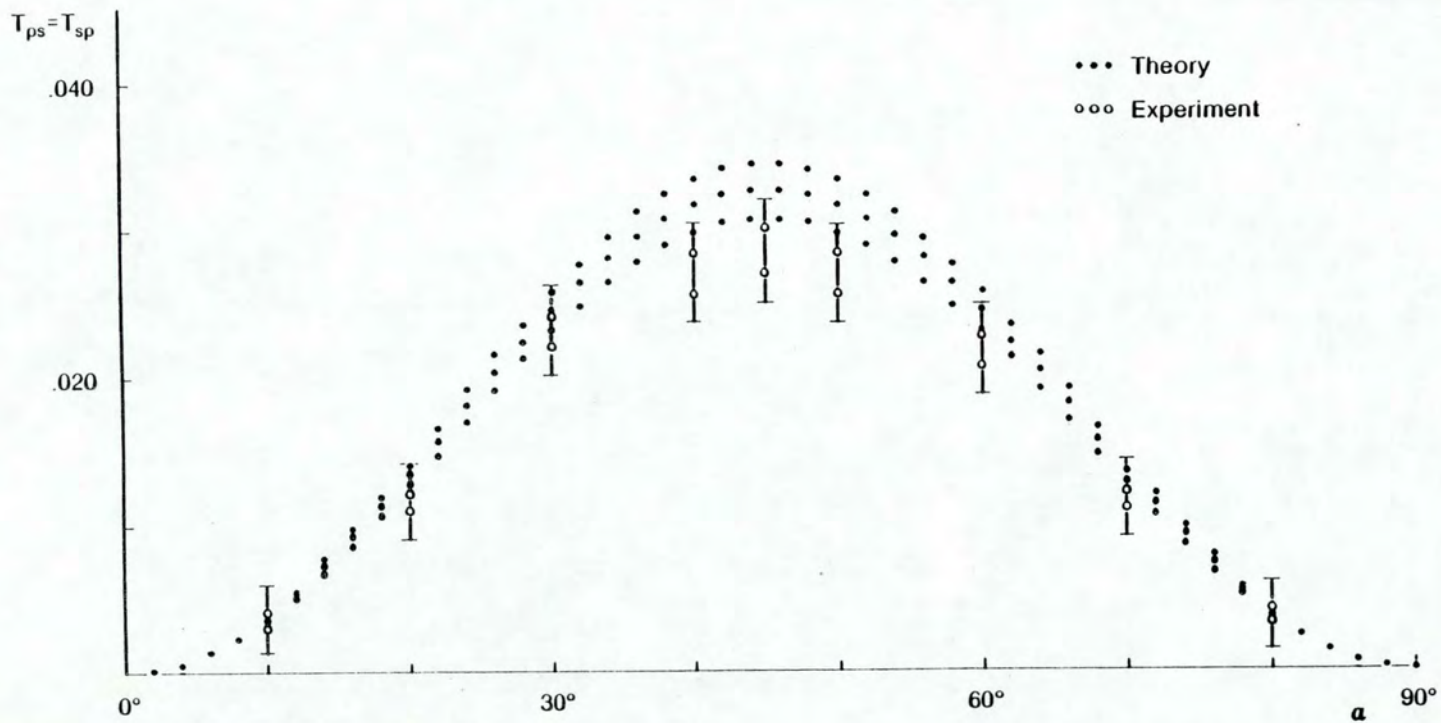| θ_0(Deg)	T_{sp} (%)[+]					T_{ss} (%)[+]				
	S	xSI	xP	T_1 (NL)	T_2 (NL)	S	xSI	T (NL)	T_1 (NL)	T_2'(BR)
0	0.0	0.000	0.000	0.00	0.00	93.8	90.000	88.64	89.43	9o.91
10	0.3	0.288	0.430	0.36	0.40	92.9	89.136	87.67	88.53	91.55
20	0.9	0.863	1.289	1.10	1.21	92.0	88.273	86.71	87.62	90.63
30	1.8	1.727	2.578	2.20	2.42	91.3	87.601	85.96	86.92	89.54
40	2.1	2.015	3.007	2.57	2.82	91.0	87.313	85.64	86.62	88.81
45	2.2	2.111	3.151	2.69	3.00	90.9	87.217	85.53	86.52	88.69
50	2.1	2.015	3.000	2.57	2.82	91.0	87.313	86.64	86.62	88.74
60	1.7	1.631	2.434	2.07	2.28	91.3	87.601	85.96	86.92	89.33
70	0.9	0.863	1.289	1.10	1.21	91.9	88.177	86.60	87.52	90.31
80	0.3	0.288	0.430	0.36	0.40	92.9	89.136	87.67	88.53	91.16
90	0.0	0.000	0.000	0.00	0.00	93.7	89.904	88.53	89.33	91.51

[+]Explanation of symbols:

α Azimuth angle
S   Measured signal
P   Polarizer correction factor = 1.4925
NL   Detector nonlinearity corrected

SI   Substrate interference correction factor = 0.9595
BR   Substrate back-reflection considered (theory)

convenient extinction coefficients to overlap them. We again choose to keep the comparison free from adjustable parameters and to leave their 2 to 4% gap for future work on inhomogeneity and scattering losses in thin films deposited at high angles of vapor incidence. Furthermore, we would expect the amount of absorption to be slightly different for different columnar orientations with respect to the electric field.

When we corrected the crossed transmittance experimental curve in the same manner as we did for the noncrossed, it would fall about 1% under the theoretical prediction. That was too large a difference (about 30% of the predicted value at $\alpha = 45°$), as can be seen from the second column in Table 5.2 (a). The substrate back-reflectance correction for such small transmittance values is negligible, and similarly minute amounts of loss were to be expected.

We then searched for another source for the disagreement and found it.

The polarizer was set (with its transmission axis) at 45°, while no other optical component was allowed to be in the beam trajectory to the analyzer. We first checked for extinction with the analyzer at 135°, and the ellipsometer performed satisfactorily. Next we oriented the analyzer transmission axis parallel to that of the polarizer and set the signal reading to 100.0, as usual in the experiment. When we turned the analyzer to 0° (horizontal position), however, the signal was 33.5. That is a pronounced departure from the expected 50% intensity transmittance and is probably due to displacement of the Glan-Thompson prisms, if not

to imperfections in the prisms themselves (about the same signal was observed with the analyzer at 180°). A polarizer correction factor is then in order, as shown in the third column in Table 5.2 (a).

Also due to the extreme sensibility of the crossed transmittance measurement, we present in Figure 5.5 theoretical curves not only for the set of principal refractive indices [1.502, 1.575, 1.788] reported in Chapter 4, but also for [1.493, 1.574, 1.803], and [1.511, 1,5767, 1733], corresponding to the upper and lower limits for the expected signal without losses. Those two additional sets are consistent with the errors estimated in (4.26) from the determination of the principal refractive indices.

The agreement in Figure 5.5 seems good supporting evidence not only to theory and experiment on the optical properties of our single dielectric film, but to the measurement of its refractive indices as well.

$T \times \lambda_0$

Figure 5.6 shows the spectral data in the visible region for a birefringent narrowband filter in the form

$$(HL)^5 \; HHHH \; (LH)^5, \tag{5.4}$$

where H stands for the zirconium oxide, high index layer and L for the silicon oxide, low index layer. Both H and L are quarterwaves at $\lambda_0 = 627.8$ nm.

The film was deposited at nearly 30° with a fixed substrate (Hodgkinson et al., 1983). Hodgkinson independently measured in
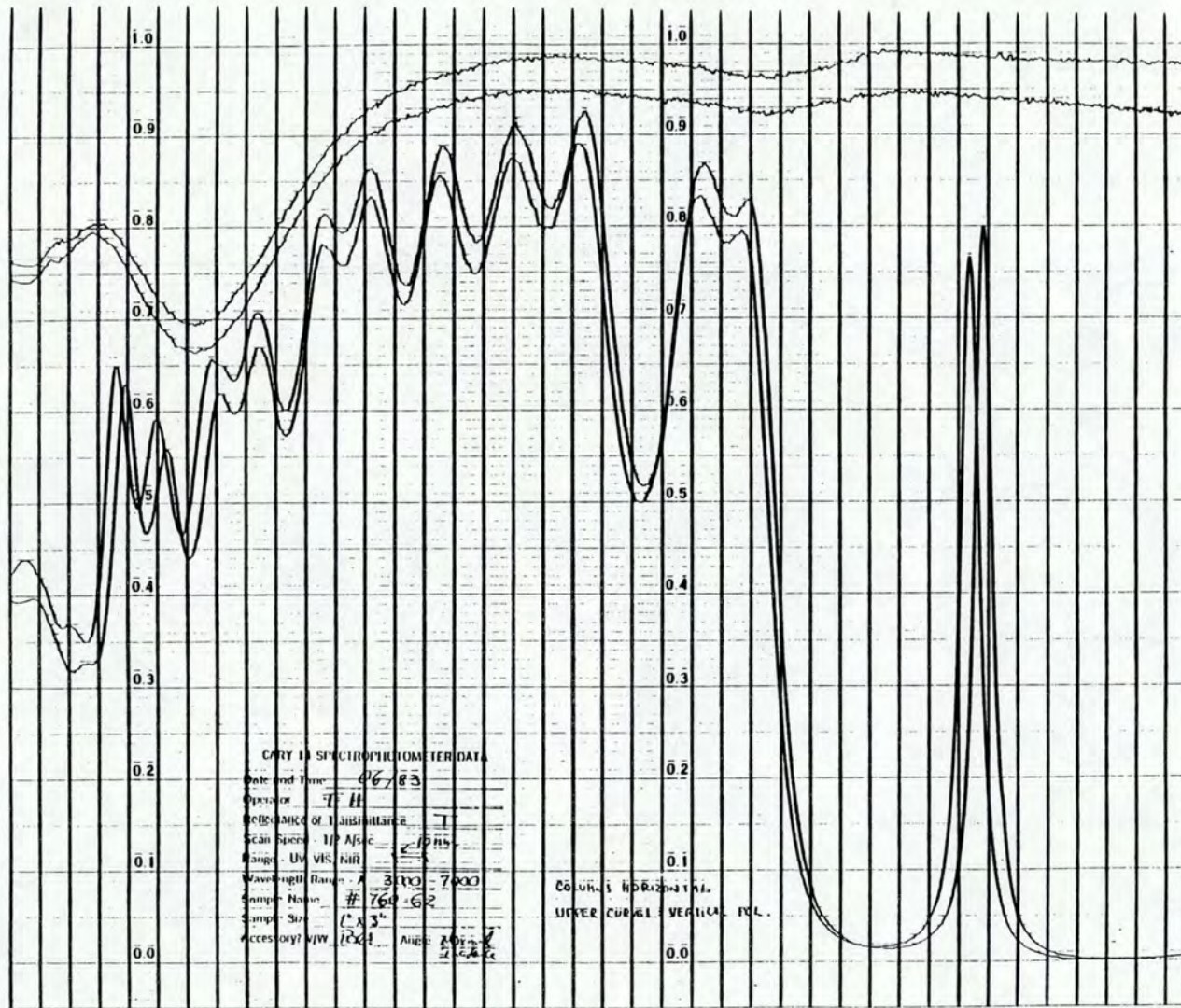
Figure 5.6. Spectral Data in the Visible Region for the Noncrossed Transmittances of a Birefringent Narrowband Filter with 21 Layers.

The upper pair of curves is a reference to the lower pair, and corresponds to the detected signal in the absence of the sample.

96

transmission the two pairs of peaks for s and p-polarized light at normal and 30° incidence shown in the close-up Figures 5.7 and 5.8. Assuming that the silicon oxide layers (structurally much more amorphous and thus with negligible birefringence as compared to those of zirconium oxide) were specified by their typical refractive index value of 1.46, and by analyzing the peaks in their highly resolved positions, he was able to provide us the following principal refractive indices for the zirconium oxide layers:

$$h_1 = 1.9476$$
$$h_2 = 1.9664 \qquad\qquad (5.5)$$
$$h_3 = 2.0332$$

The theoretical curves produced by the ANTF program with these refractive indices are shown in the upper portion of Figures 5.7 and 5.8.

The dissimilarity in predicted and measured lineshapes can be attributed to several factors. From the theoretical side, absorption or any other losses, as well as inhomogeneity, were not considered, thus producing higher and sharper peaks than otherwise expected. As to the experimental side, the rectangular cross section of the spectrophotometer beam, combined with a strong film nonuniformity, resulted in an integration over a range of different thicknesses that lowered and broadened the observed lineshape.

Still, agreement in peak position between theory and experiment is achieved within a resolution of Angstroms.
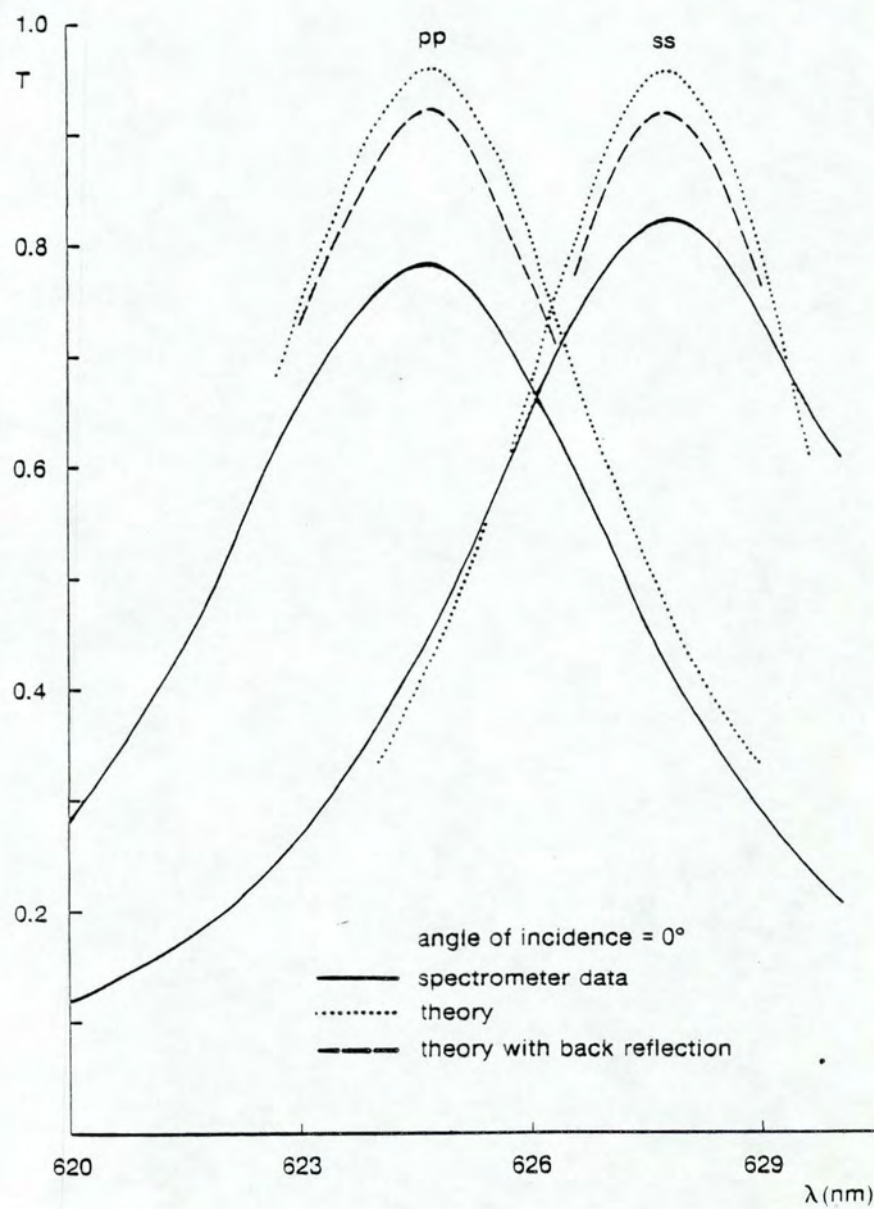
Figure 5.7.   Spectral Data for Noncrossed Transmittances at Normal Incidence.
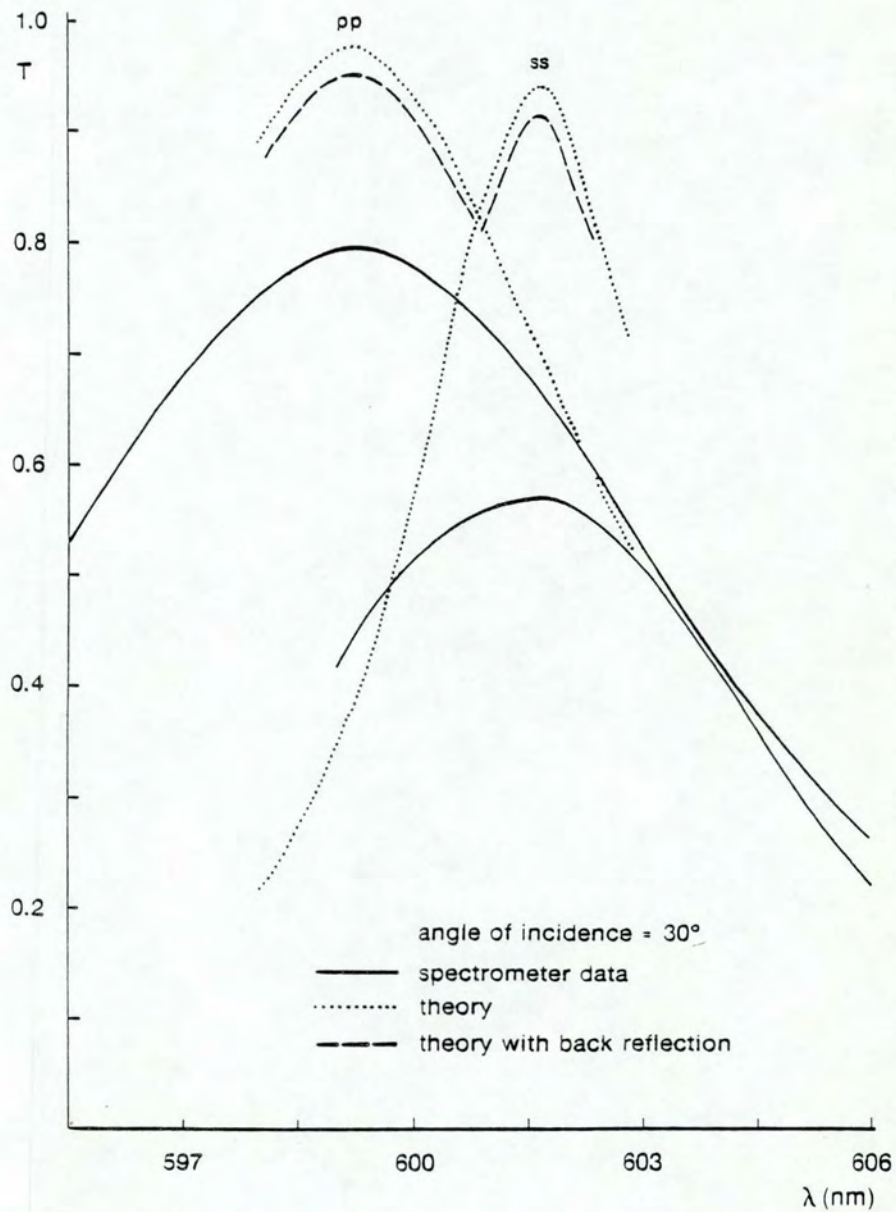
Figure 5.8.   Spectral Data for Noncrossed Transmittances at 30°.

A Hypothetical Metal Film

Although we have not measured the optical constants of an anisotropic metal film, we conclude this chapter with a brief presentation on what its optical properties might be.

We imagine a single metal film, 14.5 nm thick (semitransparent), which was vapor-deposited at 85°, corresponding to a columnar orientation angle $\phi = 80.07°$. Note the similarities in preparation conditions between our hypothetical film and those for the Al sample considered in Chapter 2, for which an effective extinction coefficient difference $\Delta k = 1.44$, identity (2.2), was experimentally determined.

For our imaginary film, we pick $\Delta k = 1.5$, disregard any slight difference in refractive indices, and choose for these a typical value in the visible region (Hass, 1965), thus generating the following optical constants:

$$
\begin{aligned}
n_1 - ik_1 &= 1.3 - i\ 2.5 \\
n_2 - ik_2 &= 1.3 - i\ 2.5 \\
n_3 - ik_3 &= 1.3 - i\ 4.0.
\end{aligned}
\tag{5.6}
$$

The resulting curves of transmittance versus azimuth angle, obtained from the theory through the ANTF program, are shown in Figure 5.9. It is interesting to notice their similarities with those in Figure 2.2.

We present in Figure 5.10 the reflectance curves for our hypothetical film and stop at this point, in the hope that this peculiar behavior will be more fully pursued in future work.

Figure 5.9. Noncrossed and Crossed Transmittances versus Azimuth Angle as Predicted from the Theory for the Hypothetical Metal Film Specified in (5.6).

Peak and valley ordinates (in percent) are 46.72 and 27.02 for (a), 1.22 and 0.00 for (b). Projection of the columnar orientation axis along the glass-film interface is vertical at the origin.
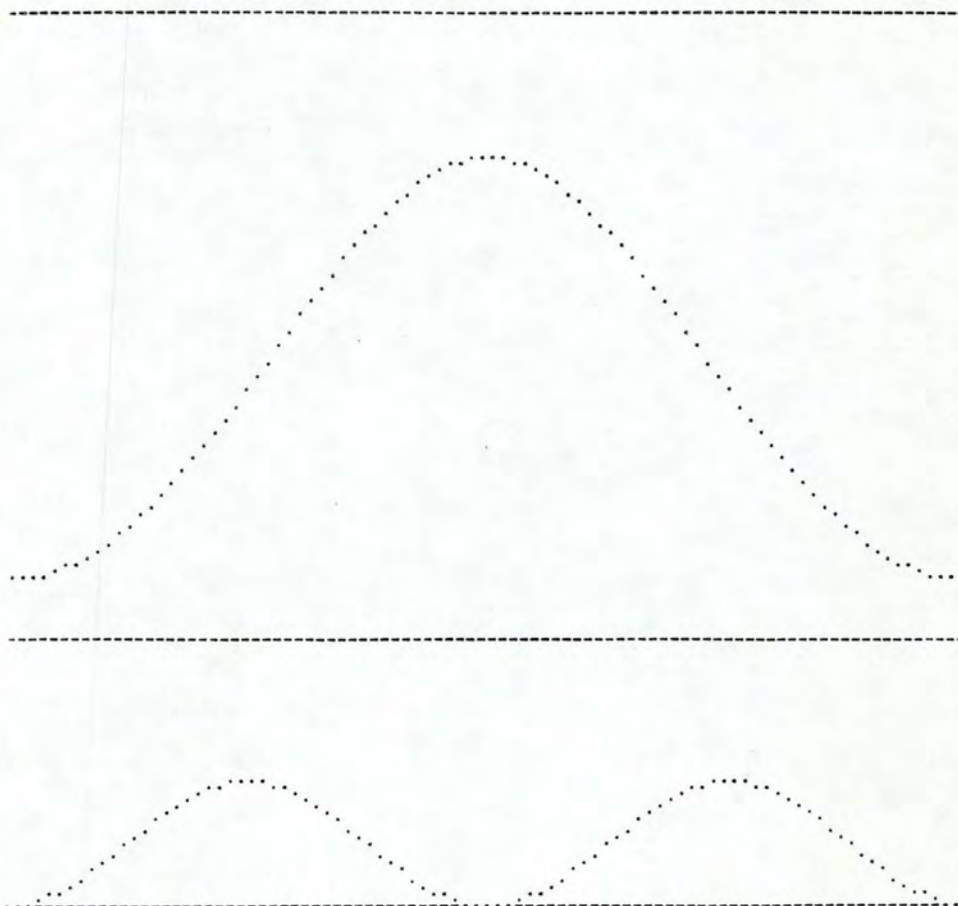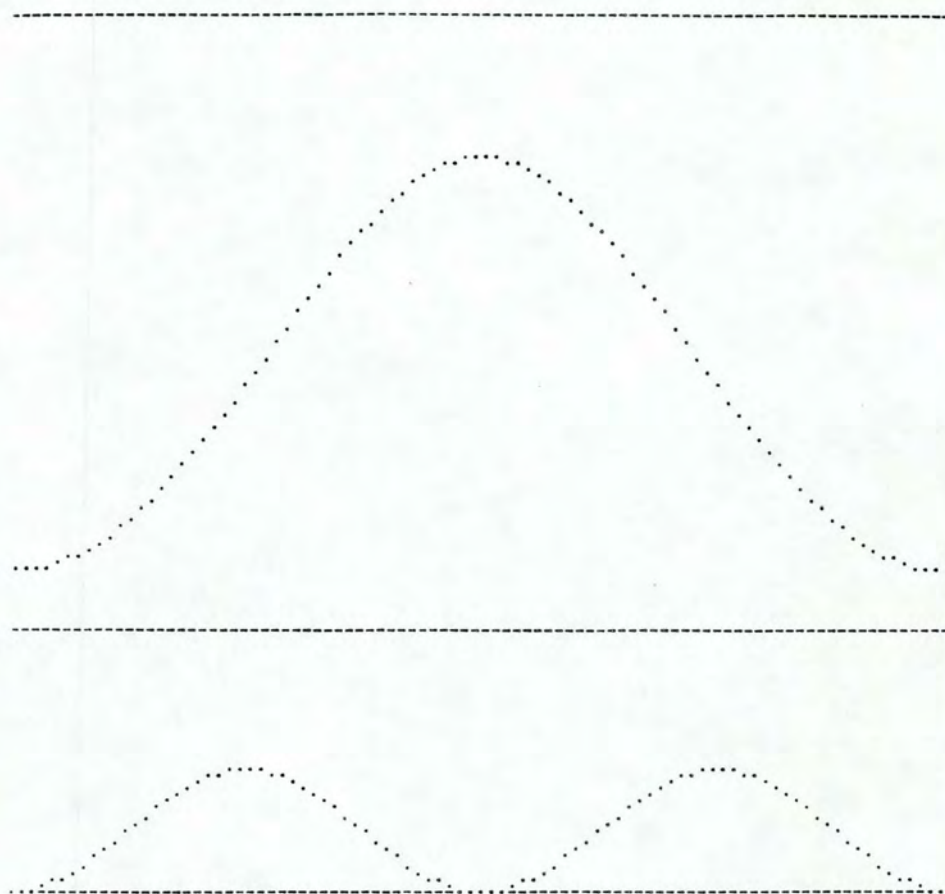
Figure 5.10.   Noncrossed and Crossed Reflectances versus Azimuth Angle
as Predicted from the Theory for the Hypothetical Metal
Film Specified in (5.6).

Peak and valley ordinates (in percent) are 43.14 and 22.95
for (a), 0.79 and 0.00 for (b). Projection of the colum-
nar orientation axis along the glass-film interface is
vertical at the origin.

CHAPTER 6

CONCLUSION

We now conclude with a brief summary of the results attained and their possible extensions, followed by some potential applications and further suggestions for future work.

Summary

The relationship between the departure from optical isotropic behavior and the microstructure of thin films was the main concern of this dissertation.

In Chapter 2, quantitative analysis of aluminum and zirconium oxide films deposited at high angles of vapor incidence indicated that metals and dielectrics present two different and analogous manifestations of the structure-induced optical anisotropy observed under normal incidence light at 632.8 nm. Such metal and dielectric films tend to behave mostly as polarizers and retarders because of significant asymmetries in extinction coefficients and refractive index values, respectively.

The almost universal columnar structure of vacuum-deposited films suggests strongly that similar behavior should be observed in films of virtually any material.

The essential thrust of this work was to grasp the fundamental reasons for this behavior beyond the phenomenological level. With

103

multilayer systems in mind, a four-dimensional theory was presented in Chapter 3 that starts from first principles, unifies previous treatments developed by several investigators for particular cases of film anisotropy, and properly handles the most general case of coupled mode propagation. Although it was built with the columnar model in mind, the theory is also valid for other sources of optical anisotropy, as long as principal axes are still definable.

In Chapter 4, the insights obtained from the theory allowed us to establish an experimental method for the determination of the three principal refractive indices and physical thickness of a single dielectric film with explicit consideration of its microstructure. The procedure is essentially straightforward, and intricate iterative calculations, common in this area, unnecessary.

All measurements in transmission can alternatively be performed in reflection, a requirement for opaque samples, and their results interpreted with an analogous outcome from the theory. The method can eventually be extended for metal films by, for example, additional retardation measurements at nonnormal incidence, although at the expense of its simplicity.

Experiment and theory were placed side by side in Chapter 5. Here the goal was to test the theoretical predictions, as well as the values previously determined for the refractive indices, against transmittance curves obtained from the ellipsometer, with the same zirconium oxide sample and under similar conditions. Although the

ellipsometer performed well in extinction measurements, detailed examination of the instrument disclosed the need for corrections in the transmittance data. After instrumental errors were identified, and the substrate role was also taken into account, the experimental curves with varying angle of incidence or azimuth angle exhibited good agreement with the corresponding predictions. A similar comparison involving a zirconium oxide/silicon oxide narrowband filter with 21 layers deposited at 30° resulted in an agreement in peak position within a resolution of Angstroms. Finally, optical properties were considered through the ANTF program for a hypothetical metal film, and similarities were pointed out between its crossed and noncrossed transmittance curves with those reported in Chapter 2 for an aluminum sample deposited at 85°.

Potential Applications

We indicate the potential usefulness of the polarization effects we have considered through examples that come to mind as these lines are being written. Some of these examples may become viable applications as control is gained over film properties.

Polarizers

Slocum (1981) has reported a metal film polarizer for the 0.8 to 1.1 m region with transmission higher than 0.40 and a degree of polarization in excess of 0.88. This element could be used in electro-optical systems, lasers, and other devices requiring a thermally stable polarizer (the common HR Polaroid sheet degrades when subjected to

temperatures above 55°C for extended periods of time). Figures 5.9(a) and 5.10(a), combined with the 90° shift in those curves from one polarization state to the other, suggest a simple and inexpensive polarizing beamsplitter. It is especially promising for the infrared, where efficiencies are expected to be higher.

Retarders

It is well known that crystal retarders require a delicate cleavage process in their manufacture and become excessively costly for large-aperture configurations, while being extremely fragile. In addition, materials like calcite, exhibiting large amounts of birefringence, can hardly be used for single-piece retarders due to prohibitive physical thickness requirements. Birefringent films of zirconium oxide, as well as of other dielectric materials, involve a much simpler fabrication process and can be easily deposited onto large areas. Tunable retarders, with different calibrations for different wavelengths, could be made by turning to advantage the gradual thickness variations of those films.

FTR Filters

Dr. Phillip Baumeister called to our attention the paper by Billings (1950), in which the use of a birefringent layer in the Turner frustrated total reflection filter (Leurgans and Turner, 1947) is proposed to induce an overlap of the otherwise separated transmission bands corresponding to the s- and p-polarizations. By using organic

birefringent films composed of benzene rings (see for example Barr and West, 1945), Billings was able to produce a single band, although without effective gain in transmission and with a much larger halfwidth. The use of our inorganic dielectric films instead would possibly provide more flexibility in design with varying deposition angles, but their discontinuous microstructure constitutes a serious source of waveguide scattering that would preclude obtaining efficient performances from the device (Burke, 1983). Nevertheless, we present it here as an illustration of the principle.

Bifocal Elements

Coating lenses or mirrors with birefringent films may induce them to exhibit two foci in distinct locations. An application for this effect was devised by Shack (1983) when he used one of the foci from a specially made quartz lens as a focusing aid for a scanning microscope. Birefringent films could be applied to existing glass elements, as well as provide more design flexibility.

Birefringent Narrowband Filters

The performance of such filters is shown in Figures 5.6 to 5.8 (Hodgkinson et al., 1983). They may find some application in information processing, for example.

Compact Birefringent Filters

Conventional Solc and Lyot filters (Evans, 1958), consisting of different combinations of birefringent crystal plates and polarizers, may have a good chance of being totally or partly translated into properly designed multilayer films composed of obliquely deposited components.

Understanding the Human Eye

It has been shown (Laties, Liebman, and Campbell, 1968) that cones in primate eyes are not perpendicular to the retina, pointing toward the center of the pupil. Hochheimer and Kues (1982) report the observation of retinal polarization effects as a clinical tool for diagnosing diaseases affecting the macula. The polarized-light retinal pattern is attributed to birefringence in cone-photoreceptor outer segments. Haidinger's brushes, a manifestation of a weak sensitivity of the human eye to polarization (Minnaert, 1954), are probably due to birefringence dispersion and dichoism of those segments.

Toward Real Films

Real films are not only anisotropic, but are inhomogeneous and scatter light. Also, their interfaces with other media are not well defined plane-parallel surfaces.

Although we were able to support qualitatively the measured results for the refractive indices with a model for the anisotropy alone,

the challenge remains for a simple effective index theory that would be valid for the whole range of film packing densities.

In principle, inhomogeneity can be treated with the matrix formulation by dividing each layer of a system into sublayers as thin as required. Similarly, interface imperfections can be taken into account by postulating the so-called "couches de passage" (transition layers), although increasing the complexity of the problem.

Analytical theories and measurement techniques have been developed for inhomogeneity and scattering problems. Perhaps the final goal toward real films will be achieved when all those departures from isotropic behavior are integrated in a common framework.

Current efforts to modify film microstructures may provide important clues in this direction. Conversely, a better understanding of those microstructures as they are, a context where this dissertation belongs, may stand as a valuable tool for monitoring such efforts.

APPENDIX A

COMPOSING THE **L**-MATRIX WITH A VECTOR BASIS

Let an arbitrary vector $\mathbf{v}(z)$ in the solution-space of equations (3.7) be represented by

$$\begin{bmatrix} v_1(z) \\ v_2(z) \\ v_3(z) \\ v_4(z) \end{bmatrix}$$

Let $\mathbf{u}^1(z)$, $\mathbf{u}^2(z)$, $\mathbf{u}^3(z)$, and $\mathbf{u}^4(z)$ be four independent solutions of (3.7) that have the following property at the $z = 0$ boundary:

$$\mathbf{u}^1(0) = \begin{bmatrix} 1 \\ 0 \\ 0 \\ 0 \end{bmatrix}, \quad \mathbf{u}^2(0) = \begin{bmatrix} 0 \\ 1 \\ 0 \\ 0 \end{bmatrix}, \quad \mathbf{u}^3(0) = \begin{bmatrix} 0 \\ 0 \\ 1 \\ 0 \end{bmatrix}, \quad \mathbf{u}^4(0) = \begin{bmatrix} 0 \\ 0 \\ 0 \\ 1 \end{bmatrix}. \tag{A.1}$$

Let $\mathbf{u}(z)$ be a solution of (3.7) such that $\mathbf{u}(0) = \mathbf{u}_0$. It can be expressed in terms of the basis set $\{\mathbf{u}^1(z), \mathbf{u}^2(z), \mathbf{u}^3(z), \mathbf{u}^4(z)\}$ as

$$\mathbf{u}(z) = u_1{}^0\mathbf{u}^1(z) + u_2{}^0\mathbf{u}^2(z) + u_3{}^0\mathbf{u}^3(z) + u_4{}^0\mathbf{u}^4(z) \tag{A.2}$$

or, in component form,

$$u_\beta(z) = \sum_{\alpha=1}^{4} u_\beta^\alpha(z)\, u_\alpha{}^0; \qquad \beta = 1,2,3,4. \tag{A.3}$$

This is equivalent to writing

$$
\begin{bmatrix} u_1(z) \\ u_2(z) \\ u_3(z) \\ u_4(z) \end{bmatrix} = \begin{bmatrix} u_1{}^1(z) & u_1{}^2(z) & u_1{}^3(z) & u_1{}^4(z) \\ u_2{}^1(z) & u_2{}^2(z) & u_2{}^3(z) & u_2{}^4(z) \\ u_3{}^1(z) & u_3{}^2(z) & u_3{}^3(z) & u_3{}^4(z) \\ u_4{}^1(z) & u_4{}^2(z) & u_4{}^3(z) & u_4{}^4(z) \end{bmatrix} \begin{bmatrix} u_1{}^0 \\ u_2{}^0 \\ u_3{}^0 \\ u_4{}^0 \end{bmatrix}, \qquad (A.4)
$$

which reproduces identities (3.10) and (3.11) in the text. Note also that boundary conditions (A.1) consistently allow the L-matrix to become the identity matrix at $z = 0$.

APPENDIX B

COORDINATE AXES REPRESENTATION OF THE ε TENSOR

By definition the ε tensor is represented in the principal axes system $P \equiv (\eta_1, \eta_2, \eta_3)$ by a diagonal matrix in the form

$$\varepsilon_P \equiv \begin{pmatrix} \varepsilon_{11} & 0 & 0 \\ 0 & \varepsilon_{22} & 0 \\ 0 & 0 & \varepsilon_{33} \end{pmatrix} . \tag{B.1}$$

Let P be obtainable from the coordinate axes system $C \equiv (x,y,z)$ shown in Figure 3.1 through a counterclockwise rotation around the y-axis, say, by an arbitrary angle ϕ. We represent this operation by the well known rotation matrix

$$R \equiv \begin{pmatrix} \cos\phi & 0 & -\sin\phi \\ 0 & 1 & 0 \\ \sin\phi & 0 & \cos\phi \end{pmatrix} . \tag{B.2}$$

Therefore, the identity connecting the displacement and the electric field vectors can be shifted from the P-representation to the C-representation through the following steps:

$$\begin{aligned} D_P &= \varepsilon_P E_P \\ R^{-1} D_C &= \varepsilon_P (R^{-1} E_C) \\ D_C &= (R \varepsilon_P R^{-1}) E_C , \end{aligned} \tag{B.3}$$

from where it becomes clear that

$$\varepsilon_C = R \varepsilon_P R^{-1} . \tag{B.4}$$

112

We have also considered in this work situations in which P is obtainable from C through the **R**-rotation, followed by a counterclockwise rotation around the z-axis by an arbitrary angle ξ represented by

$$S \equiv \begin{array}{ccc} \cos\xi & -\sin\xi & 0 \\ \sin\xi & \cos\xi & 0 \\ 0 & 0 & 1 \end{array} \qquad (B.5)$$

With the same reasoning that led to (B.4), we can promptly write

$$\epsilon_C = SR\epsilon_p R^{-1} S^{-1}. \qquad (B.6)$$

In the most general case we perform one more rotation in a similar fashion.

SELECTED BIBLIOGRAPHY

Abeles, Florin, C. R. Acad. Schi. Paris 228, 553 (1949.

Abeles, Florin, Ann. Phys. (Paris), 12th series, 5, 596 (1950).

Azzam, R. M. A., and Bashara, N. M., Chapter 4 in Ellipsometry and
    Polarized Light (North-Holland, Amsterdam, New York, 1977).

Barr, E. E., and West, C. D., U.S. Patent No. 2447790 (1945).

Bennett, Jean M., and Bennett, Harold E., Section 10 in Handbook of Optics,
    W. G. Driscoll, ed. (McGraw-Hill, New York, 1978).

Bergholm, Carl, Ann. Phys. 43, 1 (1914).

Berning, Peter H., Chapter 2 in Physics of Thin Films, 1, 71 (1963).

Berreman, Dwight W., J. Opt. Soc. Am. 62, 502 (1972).

Billings, B. H., and Pittman, M. A., J. Opt. Soc. Am. 39, 978 (1949).

Born, Max, and Wolf, Emil, Chapter 14 in Principles of Optics, 5th ed.,
    (Pergamon, Oxford, New York, 1975).

Bousquet, Paul, Optica Acta 3, 1 (1956).

Bousquet, Paul, Ann. Phys. (Paris), 2, 5 (1957a).

Bousquet, Paul, PhD Dissertation (Masson et Cie., Paris, 1957b).

Bousquet, Paul, and Delcourt, Y., J. Phys. Radium 18, 447 (1957).

Bousquet, Paul, Flory, Francois, and Roche, P., J. Opt. Soc. Am. 71, 1115
    (1981).

Bousquet, Paul, and Rouard, P., J. Phys. Radium 21, 873 (1960).

Bradford, A. P., Hass, G., McFarland, M., and Ritter, E., Appl. Opt. 4, 971
    (1965).

Bragg, W. L., and Pippard, A. B., Acta Cryst. 6, 865 (1953).

Braun, Ferdinand, Ann. Physik 16, 1 (1905).

Browning, Stephen Douglas, PhD Dissertation, Optical Sciences Center, University of Arizona (1983).

Burgers, W. G., and Dippel, C. J., Physica $\underline{1}$, 549 (1934).

Burke, James J., Optical Sciences Center, University of Arizona, personal communication (1983).

Cau, Marcel, Comtes Rendues $\underline{186}$, 1293 (1928).

Coper, H. K., Frommer, L., and Zocher, H., Ztschr. Elektrochem. $\underline{37}$, 571 (1931).

Dirks, A. G., and Leamy, H. J., Thin Solid Films $\underline{47}$, 219 (1977).

Evans, John W., J. Opt. Soc. Am. $\underline{48}$, 142 (1958).

Faraday, M., Phil. Trans. $\underline{147}$, 145 (1857).

Flory, Francois, PhD Dissertation, Universite de Droit d'Economie et des Sciences d'Aix-Marseille (1978).

Goncharenko, A. M., and Fedorov, F. I., Optics and Spectroscopy $\underline{14}$, 48 (1963).

Guenter, K. H., and Pulker, H. K., Appl. Opt. $\underline{15}$, 2992 (1976).

Hacskaylo, Michael, J. Opt. Soc. Am. $\underline{54}$, 198 (1964).

Hass, Georg, in Applied Optics and Optical Engineering, Vol. 3, R. Kingslake, ed. (Academic, New York, 1965).

Heavens, O. S., Chapter 4 in Optical Properties of Thin Solid Films (Dover, New York, 1965), 2nd ed.

Hochheimer, B. F., and Kues, H. A., Appl. Opt. $\underline{21}$, 3811 (1982).

Hodgkinson, Ian, Horowitz, Flavio, Macleod, H. Angus, Sikkens, Marten, and Wharton, John, paper to be presented at the Optical Society of America Annual Meeting, San Diego, California (1983); to be published in J. Opt. Soc. Am.

Holland, L., J. Opt. Soc. Am. $\underline{43}$, 376 (1953).

Holmes, D. A., and Feucht, D. L., J. Opt. Soc. Am. $\underline{56}$, 1763 (1966).

Horowitz, Flavio, and Macleod, H. Angus, paper presented at the Los Alamos Conference on Optics, Santa Fe, New Mexico (1983); to be published in Proc. SPIE.

Jenkins, M. A., and Traub, J. F., Comm. ACM 15, 97 (1972).

Kelly, J. C., and Heavens, O. S., Optica Acta 6, 339 (1959).

King, R. J., and S. P. Talim, Optica Acta 28, 1107 (1981).

Konig, Von H., and Helwig, G., Optik 6, 111 (1950).

Koch, H., Phys. Stat. Sol. 12, 553 (1965).

Kundt, A., Ann. Physik 27, 59 (1886).

Laties, A. M., Liebman, P. A., and Campbell, C. E., Nature (London) 218, 172 (1968).

Leamy, H. J., Gilmer, G. H., and Dirks, A. G., Chapter 4 in Current Topics in Material Science, Vol. 6 E. Kaldis, ed. (North-Holland, Amsterdam, 1980).

Leurgans, P., and Turner, A. F., J. Opt. Soc. Am. 37, 983 (1947).

Lichtenstein, Terri L., MsC Thesis, Institute of Optics, University of Rochester (1980).

Macleod, H. Angus, Proc. SPIE 325, 21 (1982).

Malleman, R., and Suhner, F., Rev. Opt. 23, 20 (1944).

Martin, P. J., Macleod, H. A., Netterfield, R. P., Pacey, C. G., and Sainty, W. G., Appl. Opt. 22, 178 (1983).

Meaburn, J., Appl. Opt. 5, 1757 (1966).

Metzdorf, W., and Wiehl, H. E., Phys. Stat. Sol. 17, 285 (1966).

Minnaert, M., The Nature of Light and Colour in the Open Air (Dover, New York, 1954).

Movchan, B. A., and Demchishin, A. V., Fiz. Metal. Metalloved 28, 653 (1969).

Nieuwenhuizen, J. M., and Haanstra, H. B., Philips Tech. Rev. 27, 87 (1966).

Pearson, J. M., Thin Solid Films 6, 349 (1970).

Pocza, E. F., Acta Phys. (Acad. Sci. Hung.) 15, 1 (1962).

Reimer, Von L., Optik 14, 83 (1957).

Schesser, Joel, and Eichman, George, J. Opt. Soc. Am. 62, 786 (1972).

Schopper, Herwig, Z. Phys. 132, 146 (1952).

Shack, Roland, Optical Sciences Center, University of Arizona, personal communication (1983).

Slocum, R. E., Proc. SPIE 307, 25 (1981).

Smith, D. O., J. Appl. Phys. 30, 264S (1959).

Smith, D. O., Cohen, M. J., and Weiss, G. P., J. Appl. Phys. 31, pp. (1960).

Teitler, S., and Henvis, B. W., J. Opt. Soc. Am. 60, 830 (1970).

Thiessen, G., and Broglia, P., Z. Astrophys. 48, 81 (1959).

Thornton, John A., J. Vac. Sci. Technol. 11, 666 (1974).

Turner, A. F., and Ullrich, O. A., J. Opt. Soc. Am. 37, 521 (1947).

Weast, Robert C., ed., Section B in CRC Handbook of Chemistry and Physics (CRC Press, Florida, 1980).

Winterbottom, A. B., J. Opt. Soc. Am. 38, 1074 (1948).

Yeh, Pochi, J. Opt. Soc. Am. 69, 742 (1979).

Zeidler, J. R., Kohles, R. B., and Bashara, N. M., Appl. Opt. 13, 1115 (1974).